Cover Page

Universiteit Leiden

The handle https://hdl.handle.net/1887/3158736 holds various files of this Leiden University dissertation.

Author: Munting, L.
Title: Functional imaging of the brain vasculature in pre-clinical models of amyloidosis
Issue Date: 2021-04-01

FUNCTIONAL IMAGING OF THE BRAIN VASCULATURE IN PRE-CLINICAL MODELS OF AMYLOIDOSIS

Leon Munting

FUNCTIONAL IMAGING OF THE BRAIN VASCULATURE IN PRE-CLINICAL MODELS OF AMYLOIDOSIS

ter verkrijging van
de graad van doctor aan de Universiteit Leiden,
op gezag van rector magnificus prof. dr. ir. H. Bijl,
volgens besluit van het college voor promoties
te verdedigen op donderdag 1 april 2021
klokke 15.00 uur

door

Leon Munting
geboren te Voorburg in 1989

Promotor
Prof. dr. ir. M.J.P. van Osch
Prof. dr. M.A. van Buchem

Copromotores
Dr. ir. L. van der Weerd

Leden promotiecommissie
Prof. dr. A.M.J.M. van den Maagdenberg
Prof. dr. H.E. de Vries   Amsterdam University Medical Center
Prof. dr. E.L. Barbier   Grenoble Institut des Neurosciences

TABEL OF CONTENTS

1

Introduction

The human brain contains roughly 86 billion neurons (Azevedo *et al.*, 2009). They communicate with each other through electrical signaling, an energy-demanding process which involves an extensive amount of active pumping of ions over the cell membrane. Neuronal signaling therefore forms the largest expense on the brain's energy budget and largely explains why the brain's relative energy use is about ten times higher than its relative mass (Shulman *et al.*, 2004). Furthermore, unlike for example liver or muscle tissue, the brain does not maintain an energy reserve. This means that all energy must be supplied from the periphery via the blood to the brain without interruption (Berg *et al.*, 2002). Consequently, a dysfunctional brain vasculature can severely impair brain function. Indeed, abrupt cessation of blood supply, such as after stroke, leads to near instantaneous and irreversible brain damage. However, more subtle and chronic cerebrovascular dysfunction has also been linked to brain diseases, including Alzheimer's disease (AD)(Iturria-Medina *et al.*, 2016). Whether cerebrovascular dysfunction in this case also plays a causative role in disease pathogenesis requires further research. Measurements optimized to detect changes in cerebrovascular function could therefore help to further unravel the pathophysiology of brain diseases such as AD. Furthermore, they could be an important indicator of brain health in general.

One of the pathological hallmarks of AD is amyloid-β accumulation in the parenchymal brain tissue. Amyloid-β is also found in the vessel wall of patients with cerebral amyloid angiopathy (CAA). These pathological accumulations of the amyloid-β peptide are referred to as amyloidosis. The aim of this thesis is to improve our understanding of the relation between cerebrovascular function and amyloidosis. To that end, cerebrovascular function measurements will be designed and carried out in animal models of cerebral amyloidosis, as seen in AD and CAA.

STRUCTURAL PROPERTIES OF THE CEREBRAL VASCULATURE

The left and right carotids and the left and right vertebral arteries are the feeding arteries of the brain. They all combine into one circular vascular structure called the circle of Willis (CoW), which is located below the brain and allows for some redistribution of blood in case one of the four feeding arteries collapses. From the CoW, several arteries branch off that go on to perfuse the brain. Of those, the posterior, middle and anterior cerebral arteries curve around the brain and supply cortical brain tissue. While curving around the brain, they bifurcate into several smaller branches that spread over the surface of the brain. These superficial arteries are often referred to as leptomeningeal arteries. Eventually, these vessels penetrate the cortical brain tissue, after which they are referred to as penetrating arterioles. From the CoW, other vessels branch off that directly penetrate the brain from the bottom part, and supply the lower brain regions, i.e. subcortical brain regions. In

both cortical and subcortical brain tissue, the penetrating vessels further branch into a capillary network. At the level of the capillaries, exchange between blood and tissue occurs. Further downstream, capillaries gather into venules and thereafter veins, through which blood exits the brain again. On the surface of the brain, veins gather into sinuses, and eventually leave the head through the jugular veins (Cipolla MJ., 2009).

On the micro-anatomical level, all different vessel types – from arteries to veins – are lined on the luminal side with endothelium. Endothelium consists of a single-cell layer of endothelial cells (ECs), which can detect pressure or chemical changes and transmit that information to more abluminal cell layers (Wang *et al.*, 2016). In arteries and arterioles, a thin layer of elastic fibers, referred to as the internal elastic lamina, separates ECs from the next concentric cell layers. This elastic layer gives arteries the capacity to dampen the pulsatility of the heartbeat. The next layer in arteries and arterioles consists of vascular smooth muscle cells (VSMCs). The size of the vessel determines how many concentric cell layers of VSMCs are present. Penetrating arterioles have 1 layer of VSMCs, whereas leptomeningeal arteries contain several layers of VSMCs. VSMCs contain contractile properties that allow the vessel to change its diameter. This is helpful for blood flow regulation to the brain (see below). After the VSMC layer, arteries have another layer of tissue, which contains mostly fibers, fibroblasts, nerve terminals and/or astrocytic end feet. Capillaries have a much thinner vessel wall. After the endothelium, there is usually a single pericyte wrapping around the vessel. Different types of pericytes have been described, and some of them also contain contractile properties. Thus, capillaries have the capacity to contribute to blood flow regulation to the brain. A unique feature of brain capillary endothelium is its high restrictiveness to the passage of molecules between blood and brain tissue. This restriction is caused by a tight link between ECs, formed with tight junction proteins. This feature of the brain capillary endothelium is generally referred to as the blood-brain barrier (BBB), and is important for proper brain function. Lastly, venules and veins have somewhat thicker walls again, also with some degree of VSMCs present in the vessel wall. However, the amount of VSMCs is much lower than in arteries. Cerebral veins do not have valves, as in other parts of the body (Cipolla MJ., 2009).

This general micro- and macro-anatomical structure of the cerebral circulation is largely similar amongst humans and mice (Hagan, 2012).

REGULATION OF BLOOD SUPPLY TO THE BRAIN

Cerebral hemodynamics is a general term used to describe blood flow dynamics in the brain. A vital hemodynamic parameter is the amount of blood that passes through a certain amount of brain tissue per unit of time, usually referred to as cerebral blood flow (CBF)

or brain perfusion. CBF is commonly expressed in mL/100 g/min. Besides CBF, cerebral blood volume (CBV) and mean transit time (MTT) are important descriptors of the cerebral hemodynamics. The former describes the volume of blood present in brain tissue, the latter the time that it takes for blood to pass through the microvascular network. The central volume theorem states that CBF is equal the ratio of CBV over MTT, which can also be deduced from the respective units.

Cerebral perfusion pressure (CPP) can be considered the driving force of cerebral perfusion with CBF being equal to the ratio between CPP and the cerebrovascular resistance. CPP is the difference between the arterial and venous pressure, and is mostly dependent on the mean arterial pressure (MAP), as the venous pressure is normally negligible. The cerebral vasculature itself poses a certain resistance on the blood flow, which is dependent amongst others on the diameter of the vessels and especially the capillaries and arterioles. To maintain a constant CBF, the diameter of the vasculature is adapted when CPP changes (Powers, 1991), i.e. vasodilation and vasoconstriction. As an example, during exercise CPP will be high, which will result in a narrowing of the vessel diameters to induce increased vascular resistance to keep CBF constant. Or, while standing up, CPP will decrease, which will result in increased vessel diameter to decrease the vascular resistance. This process is referred to as cerebral autoregulation and is of vital importance for proper brain health (Van Beek *et al.*, 2008). However, under constant CPP, several factors can modulate CBF. Such changes are also mediated through changes in the diameter of the vasculature. One external factor with a particularly strong influence on CBF is the partial pressure of CO_2 (pCO_2) in the blood. Increases in pCO_2 are tightly coupled to vasodilation, thereby increasing CBF. The CBF is also responsive to the partial pressure of O_2 (pO_2), but to a lesser extent than to pCO_2, and only on the lower range of pO_2 values (Ellingsen *et al.*, 1987). The influence of the MAP, pCO_2 and pO_2 on the vascular diameter and the resulting CBF is further explained in figure 1. There are still other factors with an influence on CBF, such as temperature (Stretti *et al.*, 2014), or certain signaling molecules such as acetylcholine (Matsuda *et al.*, 1976) and bradykinin (Unterberg *et al.*, 1984). General anesthesia also has a major influence on cerebral hemodynamics, with different types of anesthetics differently influencing CBF (Matta *et al.*, 1999) and cerebral autoregulation (Smith *et al.*, 1970; Strebel *et al.*, 1995). This is particularly interesting for animal studies, as hemodynamic measurements are generally performed under general anesthesia. The influence of different anesthesia protocols on the murine hemodynamics will therefore be discussed in more detail later in this thesis.
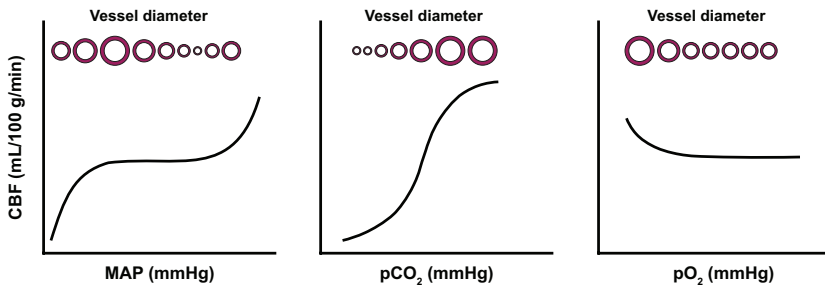
Figure 1: Influence of the mean arterial pressure (MAP), partial pressure of CO_2 (pCO_2) and O_2 (pO_2) on brain vessel diameter and cerebral blood flow (CBF). Note that in the MAP-CBF graph (left panel), the middle part is flat because constriction of the vessels negates the otherwise positive correlation between MAP and CBF, which is termed cerebral autoregulation. However, at the left and right sides of the MAP-CBF graph, the cerebral autoregulation is exhausted, and vessels either collapse (left), or forcefully dilate (right). An increase in pCO_2 (middle panel) leads to CBF increase through vessel diameter changes. A decrease in pO_2 (right panel) also leads to CBF increase, but only on the lower range of pO_2 values. Figure adapted from (Silvio Taccone et al., 2013) and (Budohoski et al., 2013).

An internal factor influencing CBF is neuronal activity. Local increases in neuronal activity are followed by local increases in CBF, which is referred to as neurovascular coupling (NVC). Interestingly, the increase in blood flow during NVC is much higher than what is required to compensate for the increased energy demand by neurons. This phenomenon is exploited during a type of imaging called blood oxygen level dependent (BOLD) functional MRI (fMRI), which is used to study brain activity (Logothetis & Pfeuffer, 2004). This will be addressed in more detail later in this chapter.

The brain's preferred energy substrate is glucose, which is normally the exclusive source of energy. However, in times of low glucose supply, the brain can switch to ketone bodies as a substitute. Oxidative phosphorylation is the major pathway for glucose metabolism in the brain. This is far more efficient in terms of energy yield than its alternative, glycolysis, but it requires oxygen. Neurons fully rely on oxidative phosphorylation, but astrocytes have been reported to also make use of glycolysis. The latter is counterintuitive given that oxygen is normally in excess in the brain and this topic is an area of continued scientific investigation. From the whole brain perspective, it is estimated that 90 % of the glucose is metabolized through oxidative phosphorylation (Magistretti & Allaman, 2015). Normally, the oxygenation saturation of arterial blood is close to 100 %, and on average, the oxygen extraction fraction (OEF) is around 37 % (Qin *et al.*, 2011). The product of the OEF and CBF gives the brain's oxygen consumption, the cerebral metabolic rate of oxygen ($CMRO_2$). When the lower limit of cerebral autoregulation has been reached, further CPP reductions will result in decreased CBF, putting the brain at risk of infarction. Up to a certain extent,

the $CMRO_2$ can be, however, compensated by increasing the OEF. A second limit will however be reached when further CPP reductions cannot be compensated anymore with OEF increases. At this point, brain ischemia will occur, with severe consequences for brain function (Powers, 1991).

NEUROVASCULAR DISEASE - GENERAL

An abrupt flow disruption of one of the larger brain arteries is referred to as stroke. Stroke prevalence in the Netherlands in 2018 was around 496,300, and 9,213 people died that year of stroke. With that, stroke was the third most common cause of death in 2018 in the Netherlands (RIVM, 2020). Stroke is usually divided into two types: ischemic and hemorrhagic stroke. The former is caused by artery obstruction and the latter by artery rupture. The ensuing lack of blood supply leads to metabolic failure and irreversible cell death in a few minutes in the core, i.e. tissue that is only supplied by the affected blood vessel. For hemorrhagic stroke, the extravasated blood forms an extra immediate risk, because within the confinement of the skull the blood may compress otherwise healthy brain tissue. Tissue that still partly receives blood from collateral vessels is not as sensitive as the core, but if not treated in time, might still become irreversibly damaged. This latter type of tissue is called the penumbra region. A fast response is thus key to rescue the penumbra region (Lo *et al.*, 2003). Early symptoms of stroke include face drooping (F), arm weakness (A) and speech difficulty (S) and can be easily remembered with the F.A.S.T. acronym to ensure a timely response (T).

Diseases that affect the smaller vessels in the brain are collectively referred to as cerebral small vessel disease (CSVD). CSVD is a major contributor to dementia and age-related disability, but can ultimately also lead to stroke. There are many different types of CSVD, of which arteriolosclerosis and cerebral amyloid angiopathy (CAA) are the most prevalent forms. Arteriolosclerosis is a systemic disease that also affects for example the vasculature in the kidneys. It is associated with hypertension, diabetes and ageing (Pantoni, 2010). CAA is also associated with ageing, but it is a brain disease that is characterized by accumulation of the amyloid-β peptide in the vessel wall of brain vessels only. Hemorrhagic lesions as a result of arteriosclerosis have a tendency to occur in deep brain regions and in the brainstem, whereas for CAA, these lesions are restricted to the cortex and subcortical white matter (lobar brain regions). This difference in affected brain region usually allows for distinction of the two diseases during life (Greenberg & Charidimou, 2018).

CAA & AD

CAA is a very prevalent disease. It has been estimated that a third of the people over 60 has CAA pathology (Love *et al.*, 2003; Vinters & Gilbert, 1983). However, CAA is still relatively unknown amongst the general public. As such, it has been fittingly termed "the biggest disease you never heard of" by the Dutch CAA foundation. For a definite CAA diagnosis, brain tissue is necessary, to allow for a histological staining proving the presence of accumulation of amyloid-β in the cerebral vessels. However, with the Boston criteria for CAA diagnosis, introduced by the group of Dr. Greenberg in Boston, imaging-based criteria were introduced to arrive at a more standardized diagnosis of "possible" or "probable" CAA. This further opened the means to do research in a clinical setting. For a possible or probable CAA diagnosis, respectively one or more indications of previous lobar vessel rupture have to be detected with imaging. These indications can include micro- or macrobleeds located in lobar regions, or cortical superficial siderosis. The latter is an MRI finding where a hypointense region overlays one or more gyri, which is thought to be the result of leptomeningeal bleeding. Importantly, the finding of bleeds in the deeper brain regions precludes the diagnosis probable or possible CAA, because, as stated above, such bleedings are likely caused by systemic arteriolar disease, not CAA (Greenberg & Charidimou, 2018).

In 2018, dementia was the most common cause of death in the Netherlands, as well as the most expensive disease on the Dutch health care budget (RIVM, 2020). Notwithstanding, an enormous growth in dementia incidence is expected, given the increasing life expectancy. This will be a huge burden on patients, family and society, whereas no treatment is available yet. AD is the most common cause of dementia ("2020 Alzheimer's disease facts and figures," 2020). Like CAA, Alzheimer's disease is also characterized by amyloid-β accumulation, but not necessarily in the vasculature. For AD diagnosis, *parenchymal* amyloid-β accumulation is required, and is one of the two pathological hallmarks of the disease. Nevertheless, almost every AD patient also has CAA pathology. The second pathological hallmark of AD is intraneuronal accumulation of tau, but tau will not be discussed in detail within this thesis. AD and CAA are thus tightly linked through amyloid-β accumulation. Novel research findings for one of the two diseases might therefore also apply to the other (Greenberg *et al.*, 2020). The connection of the two diseases is further underlined by the fact that different genetic mutations in the same gene, the *amyloid-β precursor protein (APP)*, can either lead to AD, CAA or both. One of these genetic variants leading to CAA is especially interesting in the context of the research as described in this thesis. This is the APP E693Q mutation, leading to Dutch-type CAA (D-CAA), also known as hereditary cerebral hemorrhages with amyloidosis Dutch-type (HCHWA-D). Patients with this disease mainly live in villages in the coastal area close to Leiden in the Netherlands. As such, the Leiden University Medical Center (LUMC) is the main referral center for D-CAA

patients. The disease is characterized by very early lobar hemorrhagic stroke, usually between the age of 40 and 65. The stroke is fatal 2 out of 3 times. Like sporadic CAA or AD, there is no treatment available yet for D-CAA. This lack of treatment is sustained by an incomplete understanding of the pathophysiology of the diseases. Further research in the disease mechanisms of AD and CAA is thus highly necessary. Unique for D-CAA is the possibility to genetically test individuals, and thereby come to a definite diagnosis of D-CAA during life without the need of brain biopsies. This as well as the fact that it allows for studying the pre-symptomatic phase of CAA, makes D-CAA an extremely helpful model for research into CAA (Kamp *et al.*, 2014).

The pathological burden of CAA is highest in the occipital lobe (Yamada *et al.*, 1987) and much more severe around arteries than veins (Weller *et al.*, 1998). VSMCs are particularly sensitive to amyloid-β, and become dysfunctional and eventually undergo cell death as a result of the amyloid-β accumulation in the vasculature (Christie *et al.*, 2001). This can also be seen in histological brain slices of (D-)CAA patients, stained for amyloid-β and VSMCs, where vessels with amyloid-β accumulation show reduced VSMCs, see figure 2. It is still unclear why CAA preferentially accumulates in the occipital cortex and on the arterial side of the circulation, but these findings could eventually be helpful in unraveling the disease pathophysiology. On the micro-anatomical scale, CAA can be divided into two subtypes, depending on whether or not there is capillary amyloid-β accumulation along the cerebrovascular tree. CAA with capillary involvement is referred to as type 1 CAA, or simply as capillary CAA. CAA without capillary involvement is referred to as type 2 CAA (Thal *et al.*, 2002). Patients with D-CAA only have capillary amyloid-β accumulation in a very advanced disease stage (Maat-Schieman *et al.*, 1996).
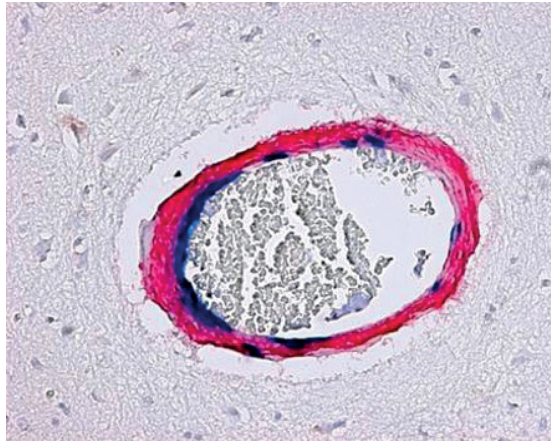
Figure 2: *Microscopic image of a D CAA brain slice. Shown is a cross-section of a vessel that has been stained for amyloid β in red and smooth muscle actin, a marker for vascular smooth muscle cells (VSMCs), in blue. Normally, VSMCs fully cover an arteriole. However, as can be seen in this image, with vascular amyloid β accumulation, VSMCs disappear. Image kindly provided by Dr. Laure Grand Moursel.*

Amyloid-β as deposited in parenchymal plaques or in the vessel wall are thought to originate from neurons (Calhoun *et al.*, 1999). Neurons express amyloid-β precursor protein (APP), a membrane protein involved in neuronal cell signaling processes. Amyloid-β is derived from APP through two enzymatic cleavages, yielding three fragments, i.e. the APP internal cellular domain (AICD), amyloid-β and soluble APP (sAPP). After cleavage, amyloid-β and sAPP end up in the extracellular space, while AICD is involved in an intracellular signaling cascade. APP cleavage does not always occur at the exact same amino acid, and as a result, amyloid-β species with different peptide lengths are created. Amyloid-β-40 and amyloid-β-42 are the most prevalent types of amyloid-β, where the numbers 40 and 42 indicate the length of the peptide. The ratio between the two has shown to play an important role in whether amyloid-β accumulates in the parenchyma or in the vasculature. Plaques contain higher amounts of amyloid-β-42, and CAA higher amounts of amyloid-β-40. The different amyloid-β species are continuously produced during life, but it is unclear whether they have a physiological function (Van Broeck *et al.*, 2007). It has been hypothesized that amyloid-β might function as an anti-microbial peptide (Welling *et al.*, 2015). However, more commonly, amyloid-β is thought to be a mere waste product that needs to be cleared from the brain.

AD is often considered the result of a disbalance in the production and clearance of amyloid-β, where neuronal loss, tau tangle formation and cognitive dysfunction are

downstream results of the disbalance. This is referred to as the amyloid hypothesis (Selkoe & Hardy, 2016). In some patients, a mutation in *APP* results in a higher production of amyloid-β, such as the KM670/671NL mutation found in two Swedish families. Mutations in the *presenilin1 (PS1)* and *presenilin2 (PS2)* genes, which encode APP cleaving proteins, can also increase amyloid-β production. This increase indeed leads to an unfavorable balance between the production and clearance of amyloid-β, with extensive amyloid-β accumulation and early cognitive decline as a result. However, in the vast majority of the patients, there is no increase in amyloid-β production. However, impaired amyloid-β clearance has been reported in these patients (Mawuenyega *et al.*, 2010). This indicates that impaired amyloid-β clearance may be an important factor in AD and CAA. There are several pathways through which amyloid-β is cleared. First is local degradation by catalytic enzymes in the extracellular space (Leissring *et al.*, 2003; Miners *et al.*, 2006). Amyloid-β is also taken up and degraded by phagocytic cells (Koenigsknecht-Talboo & Landreth, 2005). Lastly, amyloid-β is removed with the help of the vasculature, either by direct transportation over the BBB (Bell *et al.*, 2007), or by perivascular drainage (Aldea *et al.*, 2019; Iliff *et al.*, 2012). The E693Q Dutch mutation in the APP gene, leading to a charge change on the 22nd amino acid in the amyloid-β species, makes the amyloid-β more aggregation prone, more toxic to VSMCs and less efficiently cleared over the BBB. This is likely related to the early phenotype of D-CAA patients (Greenberg *et al.*, 2020).

MOUSE MODELS

Mouse models are useful models for mechanistic studies into disease and for testing safety and efficacy of novel treatments. When compared to other models for studying human disease, such as cell cultures or other animal models like the fruit fly, zebrafish, or rhesus macaque, the mouse is relatively similar to the human in terms of anatomy, physiology and genetics, while at the same time, the mouse has a short life span and requires little housing space. Furthermore, the availability of inbred strains allows for easy control of the genetic background. Lastly, the advanced genetic modification tools available for mice allow for the introduction of human disease-associated genes into the mouse genome (Gurumurthy & Kent Lloyd, 2019).

Towards creating a mouse model of AD and/or CAA, human variants of amongst others the *APP* and *PS1* genes have been introduced into the mouse genome with different familial mutations that have been linked to early-onset AD or CAA. Mostly, these genes are inserted with a neuron-specific promotor, to restrict expression to neurons. Many different types of AD/CAA-like mouse models have been created, by using different combinations of transgenes, familial mutations and promotors. In fact, over a hundred different types of models already exist, that all recapitulate one or several aspects of AD

and/or CAA (Joanna L. Jankowsky & Zheng, 2017). It is important to keep in mind that no single mouse model reflects all the aspects of human AD or CAA. On the other hand, the models can be used to study different aspects of AD or CAA in an isolated fashion. Thus, if the research question is matched with the proper model, a mouse model can be very instrumental. For example, using mouse models, it has been shown that CAA can arise when only neurons produce amyloid-β (Calhoun *et al.*, 1999), which was instrumental to arrive at the conclusion that vascular amyloid-β has a neuronal origin, not systemic. Another example is how mouse models were important for our understanding of the complicated relationship between the amyloid-β-40 to 42 ratio, different APOE isoforms and amyloid-β accumulation (Fryer *et al.*, 2005; Holtzman *et al.*, 2000).

Given that mouse models do not fully mimic AD or CAA, use of the term "model of AD" or "model of CAA" will be avoided in this thesis, as it can be misleading. Rather, they will be referred to as models of amyloidosis, as that is the aspect which the models mimic. Specifically, a model will be used with two genes - APP with the Swedish mutation (KM670/671NL), and PS1 with the ΔE9 mutation – co-inserted under a neuron-specific promotor into the mouse genome (J L Jankowsky *et al.*, 2001). This model is referred to as the APP^{Swe}/PS1^{ΔE9} (or just APP/PS1), and develops both parenchymal and leptomeningeal deposits of amyloid-β starting at the age of 6 months. At the age of 12 months, they have developed severe plaque pathology, and moderate leptomeningeal amyloid-β accumulation (Garcia-Alloza *et al.*, 2006). The capillaries and arterioles are spared in this model. This model is one of the most widely used models in AD research. In the research described in this thesis, we will also use a different mouse model that contains an APP insertion only, also under a neuron-specific promotor. However, the APP insert contains three mutations: the Swedish (KM670/671NL), the Dutch (E693Q) and the Iowa (D694N) mutation (Davis *et al.*, 2004). The model is referred to as the transgenic Swedish Dutch Iowa (Tg-SwDI) model. It develops microvascular amyloid-β accumulation and diffuse parenchymal plaques starting at the age of 6 months. By 12 months old, the model has developed severe microvascular amyloidosis throughout the brain, and extensive diffuse plaque pathology in the cortex only. Of note, another model exists which only contains the APP Dutch mutation (Herzig *et al.*, 2004). However, given its very late phenotype – it develops leptomeningeal and arteriolar CAA starting at 22-24 months of age, which is also approximately the life expectancy of a mouse – this model is considered unpractical.

TECHNIQUES FOR *IN VIVO* ASSESSMENT OF CEREBRAL HEMODYNAMICS

A wide variety of imaging techniques is available to measure cerebral hemodynamics, including autoradiography, X-ray computed tomography (CT), single-photon emission computed tomography (SPECT), positron emission tomography (PET), magnetic resonance imaging (MRI) and several optical and ultrasound-based techniques. These techniques vary widely in terms of invasiveness, the volume of tissue that can be imaged, the possibility for absolute quantification of hemodynamic parameters and the spatial and temporal resolution. Therefore, it depends on the research question what the preferred imaging modality is.

Autoradiography is one of the oldest techniques to measure tissue perfusion. It relies on intravenous (i.v.) injection of an inert, radioactive tracer into the blood stream, after which the animal model is euthanized and the brain tissue is isolated. The accumulation of the tracer within a slice of tissue, which is considered to be proportional to perfusion, is subsequently detected using a photographic film. With autoradiography, absolute perfusion values can be obtained by comparing the tissue signal to a radioactive blood scale (Reivich *et al.*, 1969; Schweitzer *et al.*, 1987). It is therefore considered the gold standard perfusion technique in animals. However, the high invasiveness makes it applicable only for terminal experiments and it cannot be used in humans. SPECT and PET are relatively closely related to autoradiography, because they also rely on i.v. injection of radioactive tracers into the blood stream. In contrast, the radiation is now detected in an intact body with detectors placed around the subject. As such, SPECT and PET can also be used in humans. The downside is, however, that detecting the tracer this way degrades the spatial resolution. While with autoradiography, SPECT and PET, the radiation comes from internal tracers, with CT, radio waves are introduced from outside. After passing through the body, the X-rays are detected. Different tissue X-ray absorption rates create contrast between tissue types, with the highest contrast between soft and hard tissue. For hemodynamic measurements, inhaled xenon or injected iodinated contrast agents are used to enhance the absorption rates of highly perfused tissue. In general, with SPECT, PET and CT, the continued circulation of the contrast agents prevents to repeatedly estimate perfusion values within a single imaging session. This makes it impossible to use them for measuring hemodynamic responses to vascular challenges. Furthermore, the different types of radiation associated these imaging techniques always pose a small risk of mutagenesis, thus the amount of imaging sessions that can be done is very limited (Wintermark *et al.*, 2005).

Hemodynamic measurements by means of MRI can be performed either with or without contrast agents. In general, MRI relies on the detection of the magnetization of protons,

also referred to as hydrogen atoms or spins, whereas differences in the magnetic properties of protons and their environment provides the contrast in MR images. MR contrast agents, which are usually gadolinium-based molecules, change the magnetic properties of protons that are in their direct vicinity. As such, when these agents are injected into the blood stream, they change the MR signal from the blood as well as from perfused tissue. With fast MRI read-out sequences, perfusion can be estimated in absolute numbers, although quantification is still considered to be error-prone (Paldino & Barboriak, 2009; Wintermark *et al.*, 2005). Like with SPECT, PET and CT, MR contrast agents continue to circulate after injection, preventing to repeatedly estimate perfusion values within a single imaging session. Traditionally, the gadolinium-based contrast agents are considered safe, and thus repeated imaging sessions seemed to be less of an issue. But recent evidence questions this assumption, as potentially toxic gadolinium deposition has been detected in the brain tissue of patients that have had repeated MRIs with contrast (Guo *et al.*, 2018). Therefore, also with MRI with contrast agents, the amount of imaging sessions should be limited.

Hemodynamics can also be assessed with MRI without the use of contrast agents. The two main types of non-invasive MRI for measuring cerebral hemodynamics are arterial spin labeling (ASL)-MRI and BOLD-fMRI, while new methods like VASO are still being introduced. With ASL-MRI, the magnetization of protons in the vessels upstream of the brain tissue is inverted with RF pulses. Thereby, the arterial blood becomes an endogenous tracer. During the so-called post-label delay (PLD), the labeled blood protons travel into the brain tissue, where they exchange with protons in brain tissue. An image is acquired both when inflowing protons are inverted, as well as during a control condition in which arterial blood spins are not inverted. Subtraction of these two images results in cancellation of the static tissue signal, and thus only perfusion signal remains. The resulting image is called a perfusion-weighted image (Alsop *et al.*, 2015). This principle is further illustrated in figure 3. Using Buxton's kinetic perfusion model (Buxton *et al.*, 1998), the ASL signal can be converted into absolute CBF values. As opposed to the previously discussed tracers, the endogenous tracer created with ASL decays in a matter of seconds. This is both an advantage and a disadvantage. At first, this decay allows for repeated CBF measurement during one imaging session. As such, perfusion responses to vascular challenges can be measured. However, the short decay-time of the label also gives ASL an inherent SNR and measurement problem. If the PLD is too long, the signal has decayed before it is measured; if the PLD is too short, the tracer has not yet arrived in the brain tissue. Usually, there is a small window of opportunity to measure the perfusion signal, and in that case, there is no problem. However, in patients with a delayed blood flow velocity, the signal may already have decayed before its arrival in the brain tissue. Advanced ASL sequences have been developed to allow for estimation of the arterial transit time (ATT). Such sequences can help to detect whether the used PLD is long enough, and can be a measure of vascular pathology by themselves (Alsop *et al.*, 2015). However, such

sequences are not yet available on pre-clinical MRI scanners. Such an MRI sequence will therefore be developed in this thesis.

BOLD-fMRI, like ASL-MRI, provides the possibility to perform repeated hemodynamic measurements within one imaging session. However, as the BOLD signal is dependent on a mixture of several parameters, i.e. blood oxygenation, CBF and CBV, the parameters cannot be determined absolutely. The BOLD signal thus always has to be normalized to a baseline condition (Logothetis & Pfeuffer, 2004).

The imaging techniques discussed for hemodynamic measurements so far all generally have an excellent tissue penetration depth (decimeters), but a relatively limited spatial resolution (millimeters). Completely different in this regard are optical imaging techniques, which generally have high spatial resolutions and low penetration depths (both in the micrometer range). The variety of optical imaging techniques that exists is endless, but most of them are not suited for *in vivo* hemodynamic measurements, because of their limited penetration depth. However, a specific type of optical imaging termed multi-photon microscopy (MPM) makes use of far-red or infrared wavelengths, which is one of the reasons why MPM has a slightly higher tissue penetration depth (up to a millimeter). As such, MPM allows for imaging of single vessels at the capillary level *in vivo* (Bacskai *et al.*, 2004). However, MPM is still limited for use in animal models only, as the 1 mm penetration depth requires removal of overlying skin and skull. The limited penetration is even an issue when imaging isolated brains post-mortem. Therefore, there has been a recent increase in interest in tissue clearing techniques for post-mortem imaging. With tissue clearing, fats and water are removed from tissue, and replaced with a medium that has the same refractive index as the remaining proteins and nucleotides, thereby making the tissue transparent. Transparency of the tissue vastly increases the penetration depth of the light. Thereby, the full mouse brain can be imaged at microscopic resolution (Richardson & Lichtman, 2015). The usefulness of tissue clearing for determining cerebral blood volume (CBV) will be further explored in this thesis.
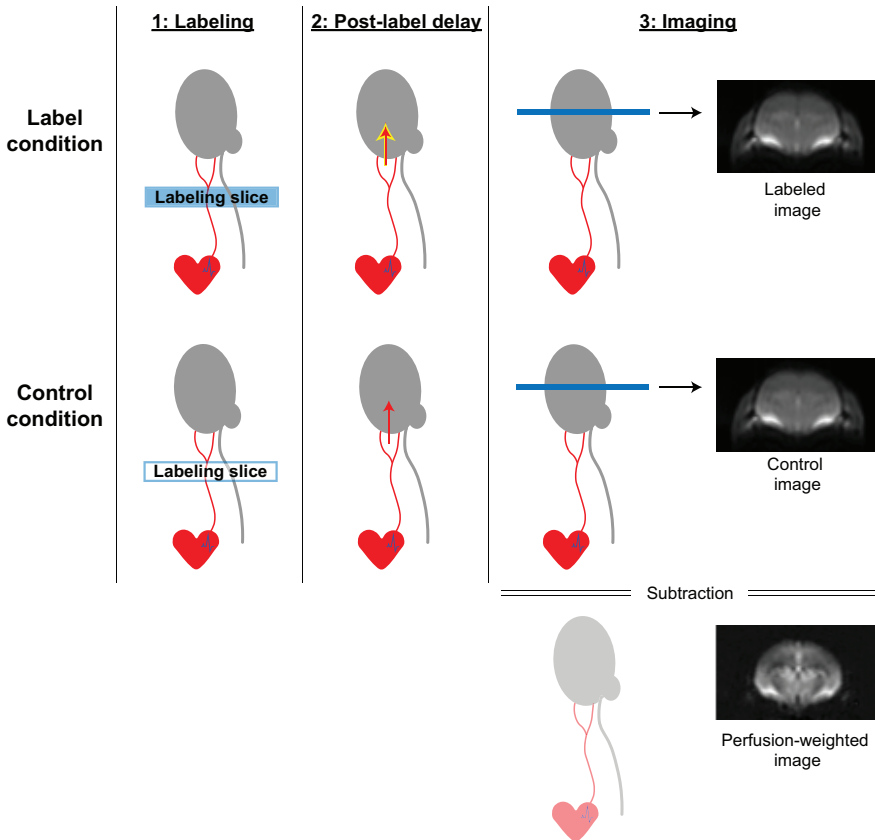
Figure 3: *Principle of Arterial Spin Labeling (ASL) MRI. During the label condition (upper row), the spins in the vessels upstream of the brain tissue are firstly inverted with RF pulses. Thereafter, during the so-called post-label delay (PLD), the labeled blood spins travel into the brain tissue, where they exchange with spins in the brain tissue. Subsequently, an image is acquired. The control condition (middle row) follows the same sequence of events, however, the spins are not inverted in this case. When the labeled image and control image are subtracted, the static tissue signal is cancelled out, and thus only perfusion signal remains. The resulting image is called a perfusion-weighted image.*

Another optical technique that allows for hemodynamic measurements is Laser Doppler Flowmetry (LDF). LDF also makes use of far-red wavelengths, but there is no imaging involved. Instead, the beam of light that is reflected by the tissue is spectrally analyzed. Flowing red blood cells cause a change in wavelength of the incoming light. The wavelength change of the reflected light is proportional to the quantity and speed of the red blood cells. This is used to calculate CBF. LDF allows for CBF measurements at very high temporal resolution, but it will only provide relative CBF values instead of absolute quantification (Rajan *et al.*, 2009).

SCOPE OF THIS THESIS

Here, the goal is to study the effect of amyloid-β accumulation on hemodynamics in the brain. Given the advantageous profile of ASL-MRI – its complete non-invasive nature allowing repeated measurements at a reasonable temporal resolution, the full brain imaging capacities, and its ability to quantify CBF absolutely– this will be the main workhorse for estimating cerebrovascular function in this thesis. However, occasionally, the ASL-MRI measurements will be supplemented with optical imaging techniques. At first, in chapter 2, the development of a novel pre-clinical ASL sequence to measure ATT will be described. Thereafter, in chapter 3, the effect of anesthesia on the hemodynamic parameters measured with ASL will be evaluated. These optimization steps will set the stage for the hemodynamic parameter estimation as described in both a more parenchymal model of amyloidosis in chapter 4, as well as a more vascular amyloidosis model in chapter 5. Lastly, the results will be discussed in chapter 6.

REFERENCES

1. 2020 Alzheimer's disease facts and figures. (2020). *Alzheimer's and Dementia*, *16*(3), 391–460. https://doi.org/10.1002/alz.12068

2. Aldea, R., Weller, R. O., Wilcock, D. M., Carare, R. O., & Richardson, G. (2019). Cerebrovascular smooth muscle cells as the drivers of intramural periarterial drainage of the brain. *Frontiers in Aging Neuroscience*, *11*(JAN). https://doi.org/10.3389/fnagi.2019.00001

3. Alsop, D. C., Detre, J. A., Golay, X., Günther, M., Hendrikse, J., Hernandez-Garcia, L., Lu, H., MacIntosh, B. J., Parkes, L. M., Smits, M., van Osch, M. J. P., Wang, D. J. J., Wong, E. C., & Zaharchuk, G. (2015). Recommended implementation of arterial spin-labeled perfusion MRI for clinical applications: A consensus of the ISMRM perfusion study group and the European consortium for ASL in dementia. *Magnetic Resonance in Medicine*, *73*(1), 102–116. https://doi.org/10.1002/mrm.25197

4. Azevedo, F. A. C., Carvalho, L. R. B., Grinberg, L. T., Farfel, J. M., Ferretti, R. E. L., Leite, R. E. P., Filho, W. J., Lent, R., & Herculano-Houzel, S. (2009). Equal numbers of neuronal and nonneuronal cells make the human brain an isometrically scaled-up primate brain. *Journal of Comparative Neurology*, *513*(5), 532–541. https://doi.org/10.1002/cne.21974

5. Bacskai, B. J., Klunk, W. E., Hickey, G. A., Skoch, J., Kajdasz, S. T., McLellan, M. E., Frosch, M. P., Debnath, M., Holt, D., Wang, Y., Huang, G., Mathis, C. A., & Hyman, B. T. (2004). *In Vivo Imaging of Alzheimer Pathology in Transgenic Mice using Multiphoton Microscopy* (pp. 33–45). Springer, Berlin, Heidelberg. https://doi.org/10.1007/978-3-642-59300-0_4

6. Bell, R. D., Sagare, A. P., Friedman, A. E., Bedi, G. S., Holtzman, D. M., Deane, R., & Zlokovic, B. V. (2007). Transport pathways for clearance of human Alzheimer's amyloid-β-peptide and apolipoproteins E and J in the mouse central nervous system. *Journal of Cerebral Blood Flow and Metabolism*, *27*(5), 909–918. https://doi.org/10.1038/sj.jcbfm.9600419

7. Berg, J. M., Tymoczko, J. L., & Stryer, L. (2002). *Each Organ Has a Unique Metabolic Profile*.

8. Budohoski, K. P., Czosnyka, M., Kirkpatrick, P. J., Smielewski, P., Steiner, L. A., & Pickard, J. D. (2013). Clinical relevance of cerebral autoregulation following subarachnoid haemorrhage. In *Nature Reviews Neurology* (Vol. 9, Issue 3, pp. 152–163). Nat Rev Neurol. https://doi.org/10.1038/nrneurol.2013.11

9. Buxton, R. B., Frank, L. R., Wong, E. C., Siewert, B., Warach, S., & Edelman, R. R. (1998). A general kinetic model for quantitative perfusion imaging with arterial spin labeling. *Magnetic Resonance in Medicine*, *40*(3), 383–396. http://www.ncbi.nlm.nih.gov/pubmed/9727941

10. Calhoun, M. E., Burgermeister, P., Phinney, A. L., Stalder, M., Tolnay, M., Wiederhold, K. H., Abramowski, D., Sturchler-Pierrat, C., Sommer, B., Staufenbiel, M., & Jucker, M. (1999). Neuronal overexpression of mutant amyloid precursor protein results in prominent deposition of cerebrovascular amyloid. *Proceedings of the National Academy of Sciences of the United States of America*, *96*(24), 14088–14093. https://doi.org/10.1073/pnas.96.24.14088

11. Christie, R., Yamada, M., Moskowitz, M., & Hyman, B. (2001). Structural and functional disruption of vascular smooth muscle cells in a transgenic mouse model of amyloid angiopathy. *American Journal of Pathology*, *158*(3), 1065–1071. https://doi.org/10.1016/S0002-9440(10)64053-9

12. Cipolla MJ. (2009). The Cerebral Circulation. In *Colloquium Series on Integrated Systems Physiology: From Molecule to Function to Disease*. Morgan & Claypool Life Sciences.

13. Davis, J., Xu, F., Deane, R., Romanov, G., Previti, M. Lou, Zeigler, K., Zlokovic, B. V, & Van Nostrand, W. E. (2004). Early-onset and robust cerebral microvascular accumulation of amyloid beta-protein in transgenic mice expressing low levels of a vasculotropic Dutch/Iowa mutant form of amyloid beta-protein precursor. *The Journal of Biological Chemistry*, *279*(19), 20296–20306. https://doi.org/10.1074/jbc.M312946200

14. Ellingsen, I., Hauge, A., Nicolaysen, G., Thoresen, M., & Walløe, L. (1987). Changes in human cerebral blood flow due to step changes in P(AO2) and P(ACO2). *Acta Physiologica Scandinavica*, *129*(2), 157–163. https://doi.org/10.1111/j.1748-1716.1987.tb08054.x

15. Fryer, J. D., Simmons, K., Parsadanian, M., Bales, K. R., Paul, S. M., Sullivan, P. M., & Holtzman, D. M. (2005). Human apolipoprotein E4 alters the amyloid-β 40:42 ratio and promotes the formation of cerebral amyloid angiopathy in an amyloid precursor protein transgenic model. *Journal of Neuroscience*, *25*(11), 2803–2810. https://doi.org/10.1523/JNEUROSCI.5170-04.2005

16. Garcia-Alloza, M., Robbins, E. M., Zhang-Nunes, S. X., Purcell, S. M., Betensky, R. A., Raju, S., Prada, C., Greenberg, S. M., Bacskai, B. J., & Frosch, M. P. (2006). Characterization of amyloid deposition in the APPswe/PS1dE9 mouse model of Alzheimer disease. *Neurobiology of Disease*, *24*(3), 516–524. https://doi.org/10.1016/j.nbd.2006.08.017

17. Greenberg, S. M., Bacskai, B. J., Hernandez-Guillamon, M., Pruzin, J., Sperling, R., & van Veluw, S. J. (2020). Cerebral amyloid angiopathy and Alzheimer disease — one peptide, two pathways. In *Nature Reviews Neurology* (Vol. 16, Issue 1, pp. 30–42). Nature Research. https://doi.org/10.1038/s41582-019-0281-2

18. Greenberg, S. M., & Charidimou, A. (2018). Diagnosis of cerebral amyloid angiopathy evolution of the Boston criteria. In *Stroke* (Vol. 49, Issue 2, pp. 491–497). Lippincott Williams and Wilkins. https://doi.org/10.1161/STROKEAHA.117.016990

19. Guo, B. J., Yang, Z. L., & Zhang, L. J. (2018). Gadolinium Deposition in Brain: Current Scientific Evidence and Future Perspectives. In *Frontiers in Molecular Neuroscience* (Vol. 11). Frontiers Media S.A. https://doi.org/10.3389/fnmol.2018.00335

20. Gurumurthy, C. B., & Kent Lloyd, K. C. (2019). Generating mouse models for biomedical research: Technological advances. *DMM Disease Models and Mechanisms*, *12*(1). https://doi.org/10.1242/dmm.029462

21. Hagan, C. E. . B. B. K. D. . (2012). Nervous System. In *Comparative Anatomy and Histology: A Mouse and Human Atlas* (pp. 339–394).

22. Herzig, M. C., Winkler, D. T., Burgermeister, P., Pfeifer, M., Kohler, E., Schmidt, S. D., Danner, S., Abramowski, D., Stürchler-Pierrat, C., Bürki, K., van Duinen, S. G., Maat-Schieman, M. L. C., Staufenbiel, M., Mathews, P. M., & Jucker, M. (2004). Abeta is targeted to the vasculature in a mouse model of hereditary cerebral hemorrhage with amyloidosis. *Nature Neuroscience*, *7*(9), 954–960. https://doi.org/10.1038/nn1302

23. Holtzman, D. M., Bales, K. R., Tenkova, T., Fagan, A. M., Parsadanian, M., Sartorius, L. J., Mackey, B., Olney, J., McKeel, D., Wozniak, D., & Paul, S. M. (2000). Apolipoprotein E isoform-dependent amyloid deposition and neuritic degeneration in a mouse model of Alzheimer's disease.

Proceedings of the National Academy of Sciences of the United States of America, *97*(6), 2892–2897. https://doi.org/10.1073/pnas.050004797

24. Iliff, J. J., Wang, M., Liao, Y., Plogg, B. A., Peng, W., Gundersen, G. A., Benveniste, H., Vates, G. E., Deane, R., Goldman, S. A., Nagelhus, E. A., & Nedergaard, M. (2012). A paravascular pathway facilitates CSF flow through the brain parenchyma and the clearance of interstitial solutes, including amyloid-β. *Science Translational Medicine*, *4*(147), 147ra111. https://doi.org/10.1126/scitranslmed.3003748

25. Iturria-Medina, Y., Sotero, R. C., Toussaint, P. J., Mateos-Pérez, J. M., Evans, A. C., Weiner, M. W., Aisen, P., Petersen, R., Jack, C. R., Jagust, W., Trojanowki, J. Q., Toga, A. W., Beckett, L., Green, R. C., Saykin, A. J., Morris, J., Shaw, L. M., Khachaturian, Z., Sorensen, G., … Furst, A. J. (2016). Early role of vascular dysregulation on late-onset Alzheimer's disease based on multifactorial data-driven analysis. *Nature Communications*, *7*, 11934. https://doi.org/10.1038/ncomms11934

26. Jankowsky, J L, Slunt, H. H., Ratovitski, T., Jenkins, N. A., Copeland, N. G., & Borchelt, D. R. (2001). Co-expression of multiple transgenes in mouse CNS: a comparison of strategies. *Biomolecular Engineering*, *17*(6), 157–165. http://www.ncbi.nlm.nih.gov/pubmed/11337275

27. Jankowsky, Joanna L., & Zheng, H. (2017). Practical considerations for choosing a mouse model of Alzheimer's disease. In *Molecular Neurodegeneration* (Vol. 12, Issue 1). BioMed Central Ltd. https://doi.org/10.1186/s13024-017-0231-7

28. Kamp, J. A., Moursel, L. G., Haan, J., Terwindt, G. M., Lesnik Oberstein, S. A. M. J., Van Duinen, S. G., & Van Roon-Mom, W. M. C. (2014). Amyloid-β in hereditary cerebral hemorrhage with amyloidosis-Dutch type. *Reviews in the Neurosciences*, *25*(5), 641–651. https://doi.org/10.1515/revneuro-2014-0008

29. Koenigsknecht-Talboo, J., & Landreth, G. E. (2005). Microglial phagocytosis induced by fibrillar β-amyloid and IgGs are differentially regulated by proinflammatory cytokines. *Journal of Neuroscience*, *25*(36), 8240–8249. https://doi.org/10.1523/JNEUROSCI.1808-05.2005

30. Leissring, M. A., Farris, W., Chang, A. Y., Walsh, D. M., Wu, X., Sun, X., Frosch, M. P., & Selkoe, D. J. (2003). Enhanced proteolysis of β-amyloid in APP transgenic mice prevents plaque formation, secondary pathology, and premature death. *Neuron*, *40*(6), 1087–1093. https://doi.org/10.1016/S0896-6273(03)00787-6

31. Lo, E. H., Dalkara, T., & Moskowitz, M. A. (2003). Neurological diseases: Mechanisms, challenges and opportunities in stroke. *Nature Reviews Neuroscience*, *4*(5), 399–414. https://doi.org/10.1038/nrn1106

32. Logothetis, N. K., & Pfeuffer, J. (2004). On the nature of the BOLD fMRI contrast mechanism. *Magnetic Resonance Imaging*, *22*(10 SPEC. ISS.), 1517–1531. https://doi.org/10.1016/j.mri.2004.10.018

33. Love, S., Nicoll, J. A. R., Hughes, A., & Wilcock, G. K. (2003). APOE and cerebral amyloid angiopathy in the elderly. *NeuroReport*, *14*(11), 1535–1536. https://doi.org/10.1097/00001756-200308060-00027

34. Maat-Schieman, M. L., van Duinen, S. G., Bornebroek, M., Haan, J., & Roos, R. a. (1996). Hereditary cerebral hemorrhage with amyloidosis-Dutch type (HCHWA-D): II--A review of histopathological aspects. *Brain Pathology (Zurich, Switzerland)*, *6*(2), 115–120. http://www.ncbi.nlm.nih.gov/

pubmed/8737927

35. Magistretti, P. J., & Allaman, I. (2015). A Cellular Perspective on Brain Energy Metabolism and Functional Imaging. In *Neuron* (Vol. 86, Issue 4, pp. 883–901). Cell Press. https://doi.org/10.1016/j.neuron.2015.03.035

36. Matsuda, M., Meyer, J. S., Deshmukh, V. D., & Tagashira, Y. (1976). Effect of acetylcholine on cerebral circulation. *Journal of Neurosurgery*, *45*(4), 423–431. https://doi.org/10.3171/jns.1976.45.4.0423

37. Matta, B. F., Heath, K. J., Tipping, K., & Summors, A. C. (1999). Direct cerebral vasodilatory effects of sevoflurane and isoflurane. *Anesthesiology*, *91*(3), 677–680. http://www.ncbi.nlm.nih.gov/pubmed/10485778

38. Mawuenyega, K. G., Sigurdson, W., Ovod, V., Munsell, L., Kasten, T., Morris, J. C., Yarasheski, K. E., & Bateman, R. J. (2010). Decreased clearance of CNS β-amyloid in Alzheimer's disease. *Science*, *330*(6012), 1774. https://doi.org/10.1126/science.1197623

39. Miners, J. S., Van Helmond, Z., Chalmers, K., Wilcock, G., Love, S., & Kehoe, P. G. (2006). Decreased expression and activity of neprilysin in Alzheimer disease are associated with cerebral amyloid angiopathy. *Journal of Neuropathology and Experimental Neurology*, *65*(10), 1012–1021. https://doi.org/10.1097/01.jnen.0000240463.87886.9a

40. Paldino, M. J., & Barboriak, D. P. (2009). Fundamentals of Quantitative Dynamic Contrast-Enhanced MR Imaging. In *Magnetic Resonance Imaging Clinics of North America* (Vol. 17, Issue 2, pp. 277–289). Magn Reson Imaging Clin N Am. https://doi.org/10.1016/j.mric.2009.01.007

41. Pantoni, L. (2010). Cerebral small vessel disease: from pathogenesis and clinical characteristics to therapeutic challenges. *The Lancet. Neurology*, *9*(7), 689–701. https://doi.org/10.1016/S1474-4422(10)70104-6

42. Powers, W. J. (1991). Cerebral hemodynamics in ischemic cerebrovascular disease. *Annals of Neurology*, *29*(3), 231–240. https://doi.org/10.1002/ana.410290302

43. Qin, Q., Grgac, K., & Van Zijl, P. C. M. (2011). Determination of whole-brain oxygen extraction fractions by fast measurement of blood T2 in the jugular vein. *Magnetic Resonance in Medicine*, *65*(2), 471–479. https://doi.org/10.1002/mrm.22556

44. Rajan, V., Varghese, B., Van Leeuwen, T. G., & Steenbergen, W. (2009). Review of methodological developments in laser Doppler flowmetry. In *Lasers in Medical Science* (Vol. 24, Issue 2, pp. 269–283). Springer. https://doi.org/10.1007/s10103-007-0524-0

45. Reivich, M., Jehle, J., Sokoloff, L., & Kety, S. S. (1969). Measurement of regional cerebral blood flow with antipyrine-14C in awake cats. *Journal of Applied Physiology*, *27*(2), 296–300. https://doi.org/10.1152/jappl.1969.27.2.296

46. Richardson, D. S., & Lichtman, J. W. (2015). Clarifying Tissue Clearing. In *Cell* (Vol. 162, Issue 2, pp. 246–257). Cell Press. https://doi.org/10.1016/j.cell.2015.06.067

47. RIVM. (2020). *Volksgezondheidenzorg.info*. https://www.volksgezondheidenzorg.info/

48. Schweitzer, A., Fahr, A., & Niederberger, W. (1987). A simple method for the quantitation of 14C-whole-body autoradiograms. *International Journal of Radiation Applications and Instrumentation. Part*, *38*(5), 329–333. https://doi.org/10.1016/0883-2889(87)90019-0

49. Selkoe, D. J., & Hardy, J. (2016). The amyloid hypothesis of Alzheimer's disease at 25 years. *EMBO Molecular Medicine*, *8*(6), 595–608. https://doi.org/10.15252/emmm.201606210

50. Shulman, R. G., Rothman, D. L., Behar, K. L., & Hyder, F. (2004). Energetic basis of brain activity: Implications for neuroimaging. In *Trends in Neurosciences* (Vol. 27, Issue 8, pp. 489–495). https://doi.org/10.1016/j.tins.2004.06.005

51. Silvio Taccone, F., Scolletta, S., Franchi, F., Donadello, K., & Oddo, M. (2013). Brain Perfusion In Sepsis. *Current Vascular Pharmacology*, *11*(2), 170–186. https://doi.org/10.2174/1570161111311020007

52. Smith, A. L., Neigh, J. L., Hoffman, J. C., & Wollman, H. (1970). Effects of general anesthesia on autoregulation of cerebral blood flow in man. *Journal of Applied Physiology*, *29*(5), 665–669. https://doi.org/10.1152/jappl.1970.29.5.665

53. Strebel, S., Lam, A. M., Matta, B., Mayberg, T. S., Aaslid, R., & Newell, D. W. (1995). Dynamic and static cerebral autoregulation during isoflurane, desflurane, and propofol anesthesia. *Anesthesiology*, *83*(1), 66–76. https://doi.org/10.1097/00000542-199507000-00008

54. Stretti, F., Gotti, M., Pifferi, S., Brandi, G., Annoni, F., & Stocchetti, N. (2014). Body temperature affects cerebral hemodynamics in acutely brain injured patients: An observational transcranial color-coded duplex sonography study. *Critical Care*, *18*(5). https://doi.org/10.1186/s13054-014-0552-7

55. Thal, D. R., Ghebremedhin, E., Rüb, U., Yamaguchi, H., Del Tredici, K., & Braak, H. (2002). Two types of sporadic cerebral amyloid angiopathy. *Journal of Neuropathology and Experimental Neurology*, *61*(3), 282–293. http://www.ncbi.nlm.nih.gov/pubmed/11895043

56. Unterberg, A., Wahl, M., & Baethmann, A. (1984). Effects of bradykinin on permeability and diameter of pial vessels in vivo. *Journal of Cerebral Blood Flow and Metabolism*, *4*(4), 574–585. https://doi.org/10.1038/jcbfm.1984.82

57. Van Beek, A. H. E. A., Claassen, J. A. H. R., Rikkert, M. G. M. O., & Jansen, R. W. M. M. (2008). Cerebral autoregulation: An overview of current concepts and methodology with special focus on the elderly. In *Journal of Cerebral Blood Flow and Metabolism* (Vol. 28, Issue 6, pp. 1071–1085). https://doi.org/10.1038/jcbfm.2008.13

58. Van Broeck, B., Van Broeckhoven, C., & Kumar-Singh, S. (2007). Current insights into molecular mechanisms of Alzheimer disease and their implications for therapeutic approaches. *Neuro-Degenerative Diseases*, *4*(5), 349–365. https://doi.org/10.1159/000105156

59. Vinters, H. V, & Gilbert, J. J. (1983). Cerebral Amyloid Angiopathy: Incidence and Complications in the Aging Brain II. The Distribution of Amyloid Vascular Changes. In *Stroke* (Vol. 14, Issue 6). http://ahajournals.org

60. Wang, S. P., Chennupati, R., Kaur, H., Iring, A., Wettschureck, N., & Offermanns, S. (2016). Endothelial cation channel PIEZO1 controls blood pressure by mediating flow-induced ATP release. *Journal of Clinical Investigation*, *126*(12), 4527–4536. https://doi.org/10.1172/JCI87343

61. Weller, R. O., Massey, A., Newman, T. A., Hutchings, M., Kuo, Y. M., & Roher, A. E. (1998). Cerebral amyloid angiopathy: Amyloid-β accumulates in putative interstitial fluid drainage pathways in Alzheimer's disease. *American Journal of Pathology*, *153*(3), 725–733. https://doi.org/10.1016/S0002-9440(10)65616-7

62. Welling, M. M., Nabuurs, R. J. A., & Van Der Weerd, L. (2015). Potential role of antimicrobial peptides in the early onset of Alzheimer's disease. *Alzheimer's and Dementia*, *11*(1), 51–57. https://doi.org/10.1016/j.jalz.2013.12.020

63. Wintermark, M., Sesay, M., Barbier, E., Borbély, K., Dillon, W. P., Eastwood, J. D., Glenn, T. C., Grandin, C. B., Pedraza, S., Soustiel, J.-F., Nariai, T., Zaharchuk, G., Caillé, J.-M., Dousset, V., & Yonas, H. (2005). Comparative Overview of Brain Perfusion Imaging Techniques. *Stroke*, *36*(9). https://doi.org/10.1161/01.str.0000177884.72657.8b

64. Yamada, M., Tsukagoshi, H., Otomo, E., & Hayakawa, M. (1987). Cerebral amyloid angiopathy in the aged. *Journal of Neurology*, *234*(6), 371–376. https://doi.org/10.1007/BF00314080

2

Transit time mapping in the mouse brain using time-encoded pseudo-continuous arterial spin labeling

Lydiane Hirschler*[1,2,3,4], Leon P. Munting*[4,5], Artem Khmelinskii[6,7], Wouter M. Teeuwisse[4], Ernst Suidgeest[4], Jan M. Warnking[1,2], Louise van der Weerd[4,5], Emmanuel L. Barbier**[1,2] and Matthias J. P. van Osch[4].

[1]Université Grenoble Alpes, Grenoble Institut des Neurosciences, GIN, F-38000 Grenoble, France
[2]Inserm, U1216, F-38000 Grenoble, France
[3]Bruker Biospin, Ettlingen, Germany
[4]Leiden University Medical Center, Department of Radiology, C.J. Gorter Center for High Field MRI, Leiden, Netherlands
[5]Leiden University Medical Center, Department of Human Genetics, Leiden, Netherlands
[6]Leiden University Medical Center, Department of Radiology, Division of Image Processing, Leiden, Netherlands
[7]Netherlands Cancer Institute, Department of Radiation Oncology, Amsterdam, Netherlands

*both authors contributed equally

**Corresponding author:
Emmanuel L. Barbier
Mailing address: Grenoble Institut Des Neurosciences, Chemin Fortuné Ferrini, 38700 La Tronche, France.
E-mail address: emmanuel.barbier@univ-grenoble-alpes.fr
Tel.: +33-4-56-52-05-88. Fax: +33-4-56-52-05-98.

ABSTRACT

Cerebral Blood Flow (CBF) is a potential biomarker for neurological disease. However, the Arterial Transit Time (ATT) of the labeled blood is known to potentially affect CBF quantification. Furthermore, ATT could be an interesting biomarker in itself, as it may reflect underlying macro- and microvascular pathologies. Currently, no optimized MRI sequence exists to measure ATT in mice. Recently, time-encoded labeling schemes have been implemented in rats and men, enabling ATT mapping with higher SNR and shorter scan time than multi-delay ASL. In this study, we show that time-encoded pseudo-Continuous Arterial Spin Labeling (te-pCASL) also enables transit-time measurements in mice. As an optimal design that takes the fast blood flow in mice into account, time encoding with 11 sub-boli of 50 ms is proposed to accurately probe the inflow of labeled blood. For perfusion imaging, a separate, traditional pCASL scan was employed. From the six studied brain regions, the hippocampus showed the shortest ATT (169 ± 11 ms) and the auditory/visual cortex the longest (284 ± 16 ms). Furthermore, ATT was found to be preserved in old wild type mice. In a mouse with an induced carotid artery occlusion, prolongation of ATT was shown. In conclusion, this study shows the successful implementation of te-pCASL in mice, making it possible for the first time to measure ATT in mice in a time-efficient manner.

2

INTRODUCTION

Currently, there is a lack of functional disease biomarkers for the diagnosis of neurovascular dysfunction in patients and animal models. This hampers the prediction of clinical events such as a vessel rupture or cognitive impairment. Cerebral Blood Flow (CBF) as measured by Arterial Spin Labeling (ASL) MRI has shown the potential to develop into such a biomarker.[1–3] However, CBF quantification is influenced by the arterial transit time (ATT), the time it takes for the blood to travel from the labeling slice to the brain slice of interest. Taking the ATT into account therefore reduces potential bias when comparing CBF between groups.[4] Furthermore, ATT is interesting in itself, as it may reflect underlying pathologies such as increased vessel tortuosity or occlusion.[5] No optimized MRI sequence exists at the moment to measure ATT in mice.

ATT maps can be obtained using multi-delay ASL.[6] However, these scans are time consuming, as each acquisition provides information at a single post-label delay (PLD) only. Recently, time-encoded labeling schemes have been implemented in rats and men, enabling ATT mapping with higher signal-to-noise ratio (SNR) and lower scan time.[7–10] The basis of this technique is the sub-division of the labeling period into "blocks" or "sub-boli" and the alternation between labeling and control states during the label period in each acquisition. The order of the label and control blocks differs over different acquisitions and is altogether played out as a Hadamard matrix (figure 1). Decoding of the Hadamard matrix enables to calculate perfusion images from the individual blocks of the Hadamard matrix. Thereby, time-encoded ASL provides the possibility to monitor the evolution of the signal over the separate PLDs from which the ATT can be estimated as well as the shape of the label inflow curve. Each individual perfusion image from a sub-bolus provides similar information and SNR as a traditional ASL scan with the same labeling duration, total scan time, TR, and PLD. Since time-encoded ASL allows the measurement of multiple ASL images within the same scan time without SNR penalty, it provides a more effective manner to obtain similar information as in a multi-PLD ASL scan.

In this study, we show that ATT estimation by time-encoded ASL is also feasible in mice. Furthermore, we demonstrate that the sequence is sensitive to mechanically induced ATT changes and that wild type mice have preserved CBF and ATT up to 25 months of age.
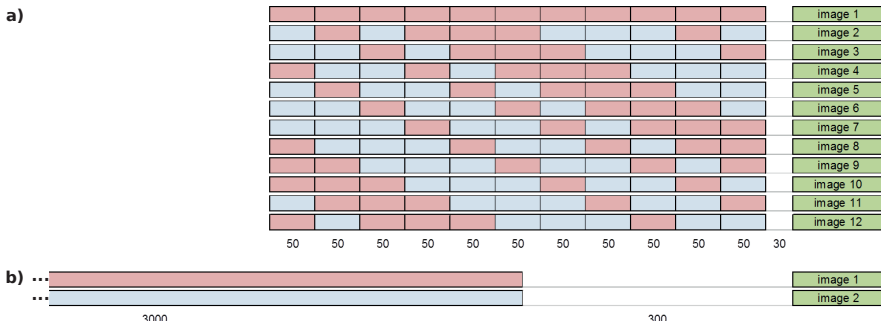
Figure 1: (a) Time-encoded pseudo-continuous arterial spin labeling (te-pCASL) and (b) standard pCASL labeling schemes. Label (resp. control) sub-boli are represented in red (resp. blue), and the imaging readout in green. The duration of every sub-bolus for te-pCASL was 50 ms and a final PLD of 30 ms was added between the end of the last sub-bolus and the EPI-acquisition. The labeling duration for standard pCASL was 3 s followed by a 300 ms PLD.

EXPERIMENTAL

Animals

All experiments were approved by the local ethics committee and were performed in full compliance with the guidelines of the European community (EUVD 86/609/ EEC) for the care and use of the laboratory animals. Experiments were performed under DEC permit 12065 of the Leiden University Medical Center.

Two groups of wild type (WT) mice were studied: one group of young mice (n = 8; 50 % female; mean ± SD age of 5.8 ± 0.40 months) and one group of old mice (n = 8; 50 % female; mean age of 25.5 ± 1.2 months). From the group of old mice, two mice (both male) needed to be excluded due to insufficient data quality due to severe movements during the scan. All mice were on a mixed C57BL/6J and C3H/HeJ background, further referred to as B6 C3 mice. Founder mice were ordered from the Jackson Laboratory and the breeding was maintained in-house. Animals were housed together in an ML-2 facility with a 12 h light/dark cycle and had unlimited access to chow food and water.

All procedures were performed under isoflurane (3.5 % for induction, 1.5-2 % for maintenance in air:O_2 1:1). During scans, respiration rate and rectal temperature were monitored and maintained at around 100 bpm and 37°C, respectively.

One additional B6 C3 young mouse (6.0 months old; male) was used for a carotid occlusion experiment to evaluate the sensitivity of the implemented method to measure ATT

variations. After anesthesia induction with isoflurane, a medial cut was made along the chest and the left carotid was disjoined from the surrounding mesenchyme. Subsequently, a stitch was used to fully occlude the artery. Then the wound was closed and the animal was scanned immediately; the time from wound closure to the first ASL scan was approximately 30 minutes. The animals were not allowed to recover after the experiments and the brains were collected for future experiments.

MR sequences and experiments

Experiments were performed on a horizontal 7-T preclinical MRI scanner (PharmaScan, Bruker, Ettlingen, Germany) with a mouse transmit-receive 23-mm volume coil. Anatomical T_2-weighted (T_2w) images were obtained through a spin-echo sequence (TR/TE = 2500/35 ms, in-plane resolution 84×84 μm², 0.7-mm slice thickness, RARE-factor = 8, acquisition time T_{acq} = 80 s). Two ASL labeling schemes were implemented: a standard pseudo-continuous ASL (pCASL) labeling scheme[11] to measure CBF and a time-encoded pCASL (te-pCASL) labeling scheme optimized for ATT measurements (figure 1). Both were followed by identical axial single-shot spin-echo EPI acquisitions of the brain (TE = 17 ms, in-plane resolution = 224 × 224 μm², slice thickness = 1.5 mm, slice gap = 1 mm, three slices with the center of the most posterior slice at approximately -3 mm from the bregma and the middle slice located at the isocenter of the bore). Since pCASL is known to be sensitive to off-resonance effects,[12,13] the entire study was performed with a global first order shim and the pCASL interpulse phase-increase was optimized during a pre-scan as described before.[14] Labeling pulses were applied in the neck, at 10 mm from the isocenter with the following sequence-specific parameters:

- For pCASL, a label duration of 3 seconds was followed by 300 ms PLD (figure 1b). 60 pairs of label/control images were acquired within 7 minutes (TR = 3498 ms).

- For te-pCASL, a Hadamard-12 matrix was used as labeling scheme (figure 1a). The duration of every sub-bolus was 50 ms and a final PLD of 30 ms was added at the end of the scheme. This resulted in 11 effective PLDs (30, 80, 130 … 530 ms). The scheme was repeated 45 times (TR = 778 ms, T_{acq} = 7 minutes).

For CBF quantification, maps of the tissue T_1 (T_{1t}) were acquired with an non-selective inversion recovery (IR) spin-echo EPI sequence (TR/TE = 10000/19 ms, 18 inversion times (TI) between 30 ms and 10000 ms, T_{acq} = 4 min) and labeling efficiency was measured 3 mm downstream of the labeling plane with a flow-compensated, pCASL-encoded FLASH sequence (TR/TE = 225/5.6 ms, 84 μm isotropic in-plane resolution, 1-mm slice thickness, NA = 2, T_{acq} = 3 min 30 s) for each animal.

Post-processing

Inversion efficiency

The inversion efficiency (α) was derived from a complex reconstruction of the pCASL-FLASH sequence as follows:

$$\alpha = \left| \frac{M_C - M_L}{2M_C} \right|, \text{ (1)}$$

where M_C and M_L are respectively the complex signals from the control and the label experiments. A region of interest (ROI) was manually drawn on each common carotid. The inversion efficiency α was obtained as the mean of the inversion efficiencies measured independently in each of the two carotids.

Scan registration and brain region delineation

To compensate for possible motion during standard pCASL and te-pCASL acquisitions, all repetitions were registered to the first EPI acquisition. ROIs for the auditory/visual cortex, hippocampus, motor cortex, sensory cortex, striatum and thalamus were delineated manually on an anatomical T_2w image of a randomly selected animal (reference T_2w image) based on the Franklin & Paxinos mouse brain atlas[15] (figure 7a). The T_2w images of the remaining animals were registered to the above-mentioned reference T_2w image and all ROIs were propagated to each animal's correspondent T_2w image. For each animal, all sequences (te-pCASL, T_{1t} map, T_2w image) were registered to the standard pCASL space. The registration of the T_2w images to the standard pCASL space allowed propagating the anatomical ROIs to all the remaining MRI sequences. Two independent observers verified the quality of the registration by visual inspection. The registration was performed using the open source image registration toolbox Elastix[16] and was performed in a coarse-to-fine manner.

T_{1t} map

The T_{1t} map was obtained by fitting the following equation to the signal from each pixel using a Levenberg-Marquardt algorithm:

$$M_z(TI) = M_0 \cdot \left(1 - 2\kappa \, e^{-TI/T_{1t}}\right), \text{ (2)}$$

where M_z is the MR signal collected at each TI, M_0 is the magnetization at thermal equilibrium, T_{1t} is the longitudinal relaxation time constant of tissue and κ is the inversion efficiency. M_0, T_{1t} and κ are the fitted parameters.

ASL maps - te-pCASL post-processing

The 45 repetitions of the Hadamard12 matrix were first averaged, after which the matrix was decoded. The same matrix was employed to determine whether a raw image was

added or subtracted. A more elaborate description of the decoding can be found in Teeuwisse *et al.*, 2014.[10] After decoding, eleven perfusion-weighted images were obtained at eleven different PLDs. Buxton's general kinetic perfusion model[17] was fitted voxel-by-voxel to ΔM over time in the perfusion-weighted images using a Levenberg-Marquardt algorithm, where ATT, CBF and T_{1app} were the estimated paraeters:

$$\Delta M(t) = \begin{cases} 0 & 0 < t < ATT \\ 2\,M_0\,CBF\,T_{1app}\,\alpha\,e^{-ATT/T_{1b}}\left(1 - e^{-\frac{(t-ATT)}{T_{1app}}}\right) & \Delta t < t < \tau + ATT \\ 2\,M_0\,CBF\,T_{1app}\,\alpha\,e^{-ATT/T_{1b}}\,e^{-\frac{(t-\tau-ATT)}{T_{1app}}}\left(1 - e^{-\frac{\tau}{T_{1app}}}\right) & \tau + ATT < t. \end{cases}$$

(3)

τ is the labeling duration of a sub-bolus; T_{1b} is the longitudinal relaxation time of blood (2230 ms at 7 T[18]) and T_{1app} is the apparent longitudinal relaxation time of tissue. t represents the time from the beginning of labeling and therefore consists of PLD + τ . This perfusion mo,del consists of three parts (Figures 3 and 4): in the first part, the labeled blood has not arrived yet, therefore the ASL signal intensity is zero. The second part is the rising part of the curve, which represents the inflow of label, while accounting of longitudinal relaxation of the label. During the third and last part, the signal declines, reflecting only relaxation of the label (outflow is neglected in this model). To quantify CBF from te-pCASL, the fit's peak height was retrieved and the CBF was calculated as described below. Voxels that showed very low transit times (< 30 ms) and/or very low longitudinal relaxation times (T_{1app} < 100 ms), which are expected to mainly reflect voxels largely composed of arterial blood, were excluded when calculating the average values over the ROIs.

ASL maps - CBF quantification

Assuming that M_{0b}, the magnetization of arterial blood at thermal equilibrium, may be approximated by M_{0t}/λ, where M_{0t} is the magnetization of tissue at thermal equilibrium and λ is the blood-brain partition coefficient of wa:ter (0.9 mL/g[19]), the following equation was used to quantify CBF (mL/100 g/min)[17,20]

$$\text{CBF} = \frac{\lambda \cdot \Delta M \cdot \exp(ATT/T_{1b})}{2 \cdot \alpha\,T_{1t} \cdot M_{0t} \cdot \exp(-(PLD-ATT)/T_{1t}) \cdot (1 - \exp(-\tau/T_{1t}))} \quad (4)$$

where ΔM is either the peak-height for te-pCASL or the averaged signal difference between control and label acquisitions for standard pCASL; T_{1t} is the tissue T_1 taken from the T_{1t} map; M_{0t} is the magnetization of tissue obtained from the IR experiment. For standard pCASL, we assumed that the ATT was shorter than the PLD.

Statistical analysis

To validate normality of the data, Kolmogorov-Smirnov tests were performed. Distributions from all parameters (ATT, CBF measured with te-pCASL and CBF measured with standard pCASL), all brain regions and both young and old mice were tested separately and did not significantly deviate from normality. Therefore, a mixed ANOVA was performed to analyze the effect of age, brain region and the interaction of age and brain region on the measured parameters ATT, CBF measured with te-pCASL and CBF measured with standard pCASL. Since Mauchly's test of sphericity was significant for all of the three parameters, the degrees of freedom for the F-distribution were corrected. The Greenhouse-Geisser-estimate of ε was 0.478 for ATT measurements, 0.413 for CBF measurements with te-pCASL, and 0.354 for CBF measurements with standard pCASL. A post-hoc Bonferroni-corrected pairwise comparison was performed when the ANOVA showed that there was a significant difference. All statistical analyses were conducted with the IBM SPSS statistics 23 software.

RESULTS

te-pCASL signal time-course

By decoding the Hadamard-encoded ASL signal,[7,10] individual sub-bolus images were obtained from the te-pCASL measurements for each slice (figure 2). At the early time points after labeling, single bright voxels can be seen, indicating the arrival of signal in the larger arteries. Quickly thereafter, the ASL signal arrives in larger groups of voxels, representing the spread of the labeled blood through smaller vessels. Lastly, the signal enters the capillaries and exchanges with the tissue magnetization. On top of these tracer kinetics, the signal continuously decays due to longitudinal relaxation.
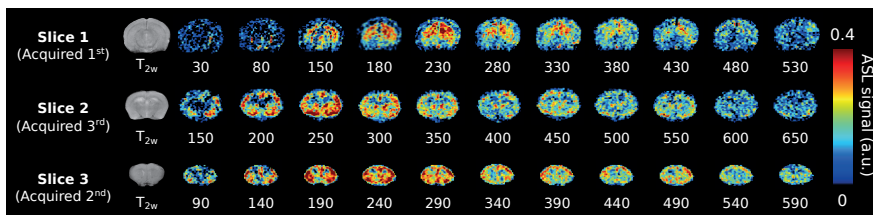

Figure 2: Example of perfusion-weighted images (arbitrary units, a.u.) obtained after Hadamard-decoding, and the corresponding anatomical images (T_2w). The number below each map indicates the effective post-labeling delay (PLD) in milliseconds. Note that the slices were acquired in interleaved order (i.e. slice 1 - slice 3 - slice 2).

Fit to the te-pCASL data

Figure 3 shows examples of the Buxton model fitted to the te-pCASL signal time-course from two individual voxels. The estimated parameters for the first voxel were: ATT 121 ms, CBF

284 mL/100 g/min and T_{1app} 296 ms and visual inspection confirms that the model fits the data. For the second voxel, the estimated parameters were ATT 92 ms, CBF 472 mL/100 g/min and T_{1app} 319 ms, but visual inspection reveals that the model fits the data poorly, as the measured ASL signal seems to show a second wave of arrival of labeled blood.

Figure 4 shows the time-courses averaged over all young mice in the auditory/visual cortex and in the hippocampus, which represent the ROIs with highest (284 ± 16 ms) and lowest ATT (169 ± 11 ms) respectively. A fit of the Buxton model to the experimental data, where ATT, CBF and T_{1app} were allowed to be adjusted to fit the data best, is displayed in the same figure (full lines). These fits are compared to theoretical Buxton curves (dashed lines), derived from the CBF value from standard pCASL, T_{1t} from the inversion recovery experiment and the ATT from te-pCASL (from now on referred to as theoretical Buxton curves). In the hippocampus, the ΔM values from te-pCASL reach markedly higher values than the ΔM from the theoretical Buxton curves. In contrast, in the auditory/visual cortex, the ΔM values from both curves reach about the same height. In both brain regions, the decay after the peak is faster in the te-pCASL data than in the theoretical Buxton curves: mean decay values retrieved from the fit to the te-pCASL data are between 300 ms and 500 ms instead of the 1600-1700 ms measured with the IR sequence.

ATT and CBF maps

Figure 5 shows the CBF and ATT maps of a representative mouse. Next to the CBF maps determined with te-pCASL (second row), maps acquired with standard pCASL are also shown (first row). In both CBF maps, a clear contrast is observed between grey and white matter (corpus callosum), with grey matter showing higher values. However, it can also be noticed that CBF values are higher in the te-pCASL measurement as compared to those measured with standard pCASL.

Effect of left carotid occlusion

Both the ATT and the CBF maps measured in the mouse with a left carotid occlusion are affected by the occlusion (figure 6). When comparing the ROIs drawn in the hemisphere ipsilateral to the occlusion with their respective contralateral ROIs, ATT was found to be slightly increased (11 % on average), whereas CBF was markedly lower (47 % for standard pCASL CBF and 33 % for te-pCASL CBF on average).
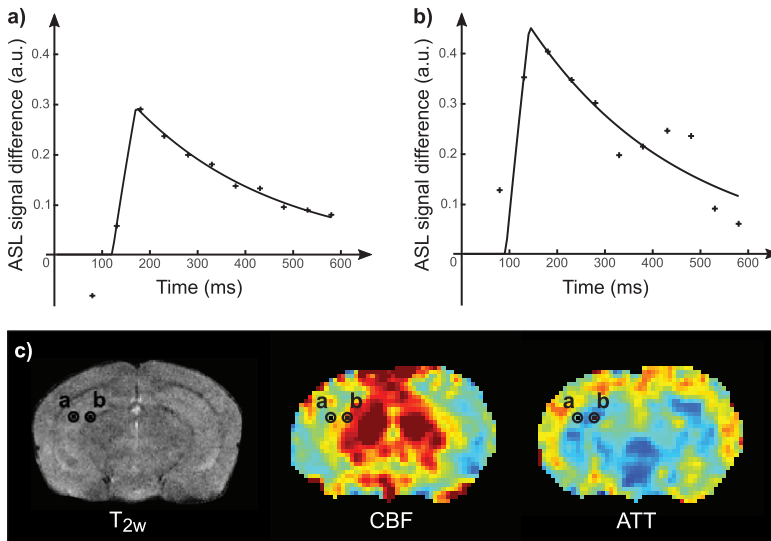
Figure 3: *Two examples of the signal intensity (i.e. decoded Hadamard-encoded ASL-signal) time courses (crosses) with their corresponding model fits (full lines). The two voxels are taken from the same mouse and the same brain region (hippocampus). The estimated parameters for the first voxel are (a) arterial transit time (ATT) 121 ms, cerebral blood flow (CBF) 284 mL/100 g/min and T_{1app} 296 ms and the model seems to fit the data. For the second voxel (b), the estimated parameters are ATT 92 ms, CBF 472 mL/100 g/min and T_{1app} 319 ms, but the model does not fit the data well.*
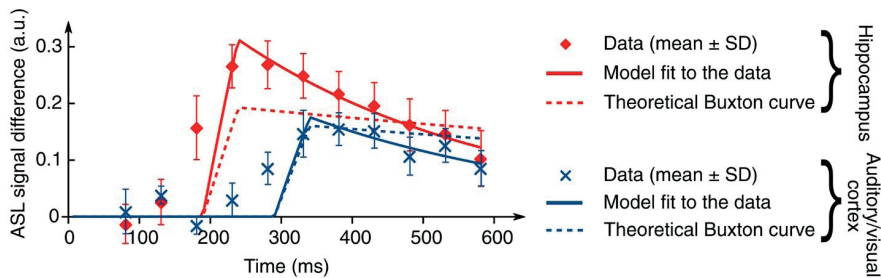

Figure 4: *Signal time-courses of the time-encoded pseudo-continuous arterial spin labeling (te-pCASL) signal (mean ± standard deviation, SD). te-pCASL ΔM values in the sub-boli are averaged over all young mice for two brain regions (crosses) and displayed together with the fit to the data (full lines). Dashed lines represent theoretical Buxton curves with cerebral blood flow (CBF) values from standard pCASL, Tissue T_1 values from the inversion recovery experiment and arterial transit times (ATTs) from te-pCASL. The auditory/visual cortex are depicted in blue and the hippocampus in red.*
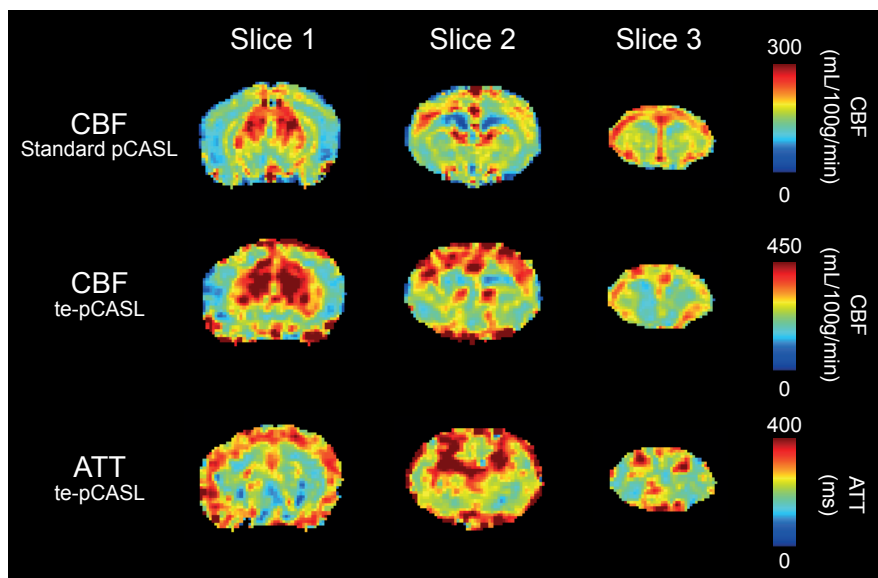
Figure 5: Cerebral blood flow (CBF) maps obtained in one mouse (3 slices) with a standard pseudo-continuous arterial spin labeling (pCASL) acquisition (first row) and a voxel-by-voxel fit to the time-encoded pCASL data (te-pCASL, second row). The color scales are different in order to have a good contrast in both maps. The third row shows the arterial transit time (ATT) as obtained from te-pCASL.

Effects of age and brain region on ATT and CBF

No significant effects of age were observed for the ATT (F [1,12] = 0.056), the CBF measured with te-pCASL (F [1,12] = 0.220) nor for the CBF measured with standard pCASL (F [1,12] = 0.484) (figure 7).

A significant effect of the brain region on ATT, p<0.001 (F [2.388,28.658] = 92.335) was found, with 22 out of the 30 post-hoc brain region comparisons showing statistically significant differences.

No additional effects of interaction between age and brain region were observed on the ATT (F [2.388,28.658] = 0.264), te-pCASL CBF (F [2.064,24.768] = 0.399) or standard pCASL CBF (F [1.770,21.237] = 0.454).
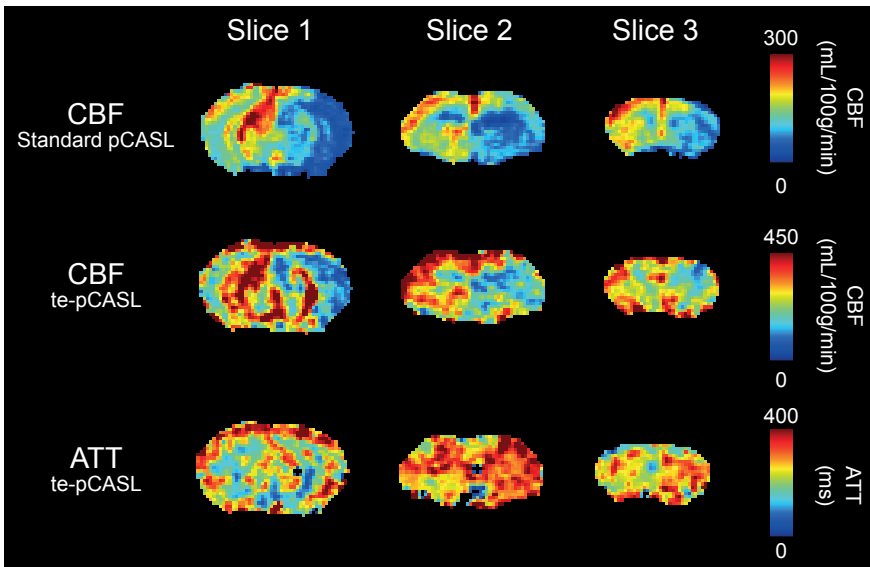
Figure 6: *Cerebral blood flow (CBF) maps from standard pseudo-continuous arterial spin labeling (pCASL, (first row) and from time-encoded pCASL (te-pCASL, second row) and arterial transit time (ATT) maps (bottom row) obtained on a mouse with a left carotid occlusion (3 slices). Note that the images are represented in radiological convention.*

te-pCASL CBF versus standard pCASL CBF

CBF estimations as measured with the te-pCASL and the standard pCASL sequences in all the 14 animals and all the brain regions were compared in a Bland-Altman plot. The te-pCASL sequence shows a consistently higher estimated CBF than the standard pCASL sequence (figure 8). Furthermore, the difference between the two measurements increases with the mean CBF value.
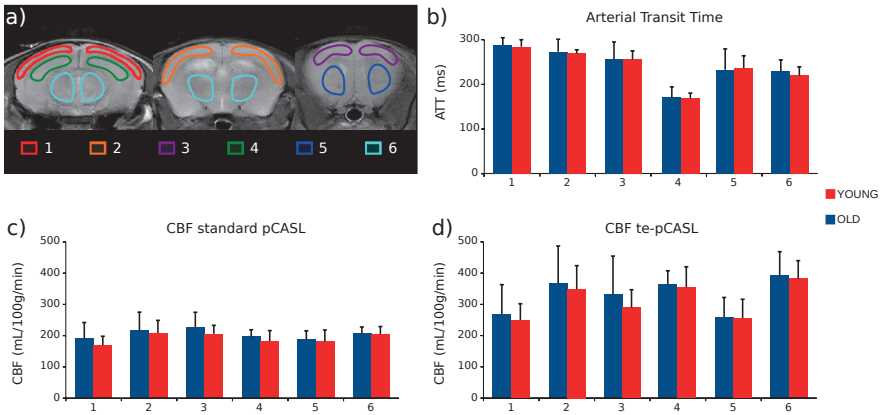
Figure 7: (a) Example of anatomical T_2-weighted images with regions of interest: 1- Auditory/visual cortex, 2- Sensory cortex, 3- Motor cortex, 4- Hippocampus, 5- Striatum, 6- Thalamus. (b) Comparison between young (red) and old (blue) mice in different brain regions for arterial transit time (ATT), (c) cerebral blood flow (CBF) from standard pseudo-continuous arterial spin labeling (pCASL) and (d) CBF from time encoded-pCASL (te-pCASL). Bars show mean values ± standard deviation.
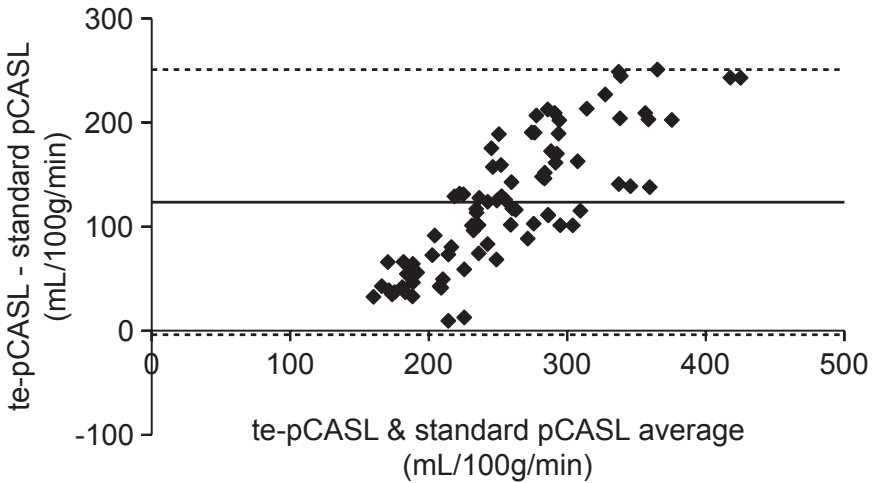

Figure 8: Bland-Altman plot comparing cerebral blood flow (CBF) values from time-encoded pseudo-continuous arterial spin labeling (te-pCASL) and standard pCASL. All 14 animals and all the brain regions are represented. The central line represents the mean of all values and the two dashed lines are offset by 2 ± standard deviation from that mean.

DISCUSSION

This study demonstrated that the implementation of a time-encoded ASL approach enables ATT measurements in mice. Since inflow times in the mouse brain are short and the brain regions are small compared to human anatomy, high spatial and temporal resolutions are required, which severely limits the perfusion SNR. The above described te-pCASL sequence was optimized to keep a balance between spatial resolution, temporal resolution and perfusion SNR. The high amount of averaging was a prerequisite for this trade-off (note that one Hadamard scheme is already equivalent to six averages of standard multi-PLD pCASL performed with a label duration equal to the sub-bolus duration[7]). This also made it preferable to split the perfusion imaging and the ATT measurement into two separate sequences. A "Free-lunch-approach" in which ATT-measurement blocks are played out during the PLD of a traditional pCASL scan would either lead to too low SNR for the ATT measurement to allow accurate ATT measurements or to too long scan times.

The measured ATT values were different across brain regions. Average ATT values in young mice varied from 169 ms (hippocampus) to 284 ms (auditory-visual cortex). To the best of our knowledge, only one other study acquired Hadamard-encoded ASL-MRI data in animals, which were obtained with CASL in rats.[9] In that study, ATT was measured in cortical regions of three rats to be between 190 and 310 ms. The values from the time-encoded sequence and those from the multi-PLD CASL sequence acquired in the same animals were well in accordance with each other. In an earlier study, ATT estimates for the whole rat brain measured with multi-PLD ASL in a group of 12 rats ranged from 100 to 500 ms.[6] Using a dynamic ASL scheme (DASL), another study reported ATT values in rats of around 200 ms.[21] Also, a pCASL optimization study in mice, which may not have been intended to estimate ATT, does provide a rough estimation of ATT in mice:[22] the authors optimized a pCASL sequence by varying several parameters settings, including the PLD, and analyzed the resulting SNR in the perfusion images. Regarding the PLD, they concluded that it ideally should be between 200 and 400 ms, since the perfusion signal is highest between these points. Hence, the values found in this study are in agreement with previously reported ATT values.

Furthermore, the animal with a unilateral carotid occlusion showed increased ATTs in the ipsilateral hemisphere. However, the ATT difference between the ipsilateral and contralateral hemispheres was not very large (11%), especially compared to the major difference in CBF measured in the same scans. It can thus be questioned whether ATT measurements in mice would be suitable to detect milder pathology, such as partial occlusion, or increased vessel tortuosity with the setup used in this study.

In all mice, cortical regions showed longer transit times than subcortical regions. This is

consistent with the anatomy of the murine cerebral circulation.[23] The major blood supply of the murine cerebrum comes from the internal carotid arteries, which end in the circle of Willis, located ventrally to the brain. From there, several arteries sprout, which supply blood to the different brain regions. Subcortical tissue is supplied with blood through arteries such as the posterior cerebral artery (PCA) and the anterior choroidal artery (AchA), which directly penetrate the brain tissue from the circle of Willis. The mouse cerebral cortex on the other hand, is mostly supplied by the anterior and middle cerebral arteries (ACA and MCA respectively), which first curve around the cerebrum before they penetrate the brain tissue. In the posterior part of the cerebrum, this cortical-subcortical difference is the most profound. The posterior part of the cortex is fed by the most distal parts of the ACA and MCA, which wrap around the frontal and medial cortex. On the other hand, the PCA and AchA penetrate directly into the subcortical regions in the posterior part of the cerebrum, with a much smaller distance to the internal carotids. This could explain the large difference in ATT between the cortical and subcortical regions on the most posterior slice in figure 5. Furthermore, it could explain the fact that the hippocampus, located posteriorly and subcortically, showed the lowest transit times from the regions analyzed in this study (figure 7b).

In all six brain regions analyzed, the mean ATT was smaller than 300 ms. This indicates that the PLD-choice of the standard pCASL, 300 ms, was appropriate to reduce contamination of the ASL signal from the major arteries and to limit the sensitivity of pCASL to ATT heterogeneity.[4] However, on the microscale (arterioles, capillaries, parenchyma and venules), it remains elusive in which compartment the label resides at the moment of detection, both for the CBF measured with standard pCASL, as well as for CBF measured with te-pCASL. At the chosen PLD of 300 ms, smaller vessels may still contain labeled blood that ultimately moves on to perfuse tissue in a different voxel. Previously, distinctions have been made between vascular and tissue transit time.[4,24] The te-pCASL sequence used here was optimized to see the inflow-phase of the label, and thus corresponds to the aforementioned vascular transit time. Due to the fact that ATT is mainly influenced by the macro-vasculature, measurement of the *tissue* transit time may provide additional useful information on the microvascular status. The exact definition of tissue transit time, whether it indicates arrival of labeled spins in the extravascular space, in the capillaries or in the microvasculature that only feeds tissue located within a distance smaller than the size of an imaging voxel, varies among studies. In order to measure transit times to the microvasculature, vascular crushers can be used to crush the signal coming from flowing spins in the arteries just before the imaging read-out,[25] with the strength of the crushers determining how far down the vascular tree the ASL signal is suppressed. However, this approach further lowers SNR, as part of the perfusion signal is also attenuated due to the diffusion-weighting of the crushers. Another method exploits the measurement of the T_2 of the ASL signal, since the T_2 of the label depends on whether it is intra- or extravascular.[26–29]

This approach has the potential to distinguish between labeled spins in vascular and extravascular spaces, but has to deal with the difficulties inherent in separating the components in biexponential transverse relaxation signals. In rats, the measured transit time of labeled spins to the extravascular space was about 370 ± 40 ms longer than the ATT,[28] providing a ballpark estimate of what could be expected in mice. The transit time to the moment labeled spins arrive in vessels that are small enough to only feed local tissue, which would be the time of interest to choose the PLD, is likely situated between the ATT measured here and this tissue transit time.

The te-pCASL sequence may be improved in several ways. Tissue transit times may be longer than the longest effective PLD used in the te-pCASL labeling scheme of this study. It might therefore be useful to adapt the temporal encoding scheme to cover later time points. Furthermore, given the low SNR of the te-pCASL measurements in mice, the te-pCASL sequence should probably be adapted in combination with higher field strengths and/or more sensitive receive coils in order to measure tissue transit times. A second technical limitation of the current sequence was the limited number of slices (three). This was caused by the long readout time per slice: extending the number of imaging slices to four (or more), would result in poor determination of the ATT in the additional slices, since the label would already have arrived. This limitation can be overcome by using a 3D readout, a multiband readout, or stronger and faster gradients.

The ASL signal of the te-pCASL data decreased faster than the T_{1t} measured with the IR sequence. This is also the reason why CBF values from the te-pCASL experiment were quantified from the fit's peak height (ΔM), instead of directly using the CBF value provided by the fit. There may be explanations at both sides of the signal profile from the te-pCASL data for the observed fast decay. Since the te-pCASL sequence is optimized to see the inflow-phase of the label, it will be contaminated by vascular signal. This may lead to higher values at the early part of the signal profile. This explanation is supported by figure 3b and figure 4. In figure 3b, the first peak most probably represents the passage of a bolus through arteries feeding more distal brain regions, whereas the second peak would represent true perfusion of the voxel, identical to what has been described by Chappell *et al.*[30] Nevertheless, after averaging signals across voxels in the cortical ROI and across animals this pattern was not visible anymore (figure 4), and thus further research is necessary to document these effects. Moreover, a higher signal was measured in the hippocampal ROI for the earlier time-points after labeling for the te-pCASL data (figure 4). Labeled spins detected in these time-points may be located in the larger vessels that surround and penetrate the hippocampus,[23] but may go on to perfuse a different voxel in the later time-points. The signal in the auditory/visual cortex, containing less of these large vessels, show comparable peak signal in the te-pCASL data curve and the theoretical Buxton curve, which was obtained from the standard pCASL perfusion scan. At the late

part of the time profile of the te-pCASL signal, there may be influence by venous outflow, which was not taken into account in this study. Underestimation due to venous outflow becomes of particular importance with high blood flow[31] and high blood T_1.[18] In humans, this may be less of a problem than in rodents, which have higher CBF and are imaged at higher magnetic fields with therefore prolonged blood T_1. In rats, using a multi-TI FAIR approach, significant outflow of labeled blood from the imaging slice leading to accelerated ASL signal decrease was shown for CBF values higher than 100 mL/100 g/min.[32] In a previous DASL study in rats, the authors also measured higher CBF and faster signal decay in voxels containing mostly arterial signal.[21]

The different designs of the standard pCASL and the te-pCASL sequence ultimately resulted in differences between the measured CBF values, which can probably be explained by the above described vascular artefacts and venous outflow. In addition, it should be noted that the standard pCASL sequence, with its long labeling duration (3 s), may be particularly sensitive to the outflow effect, especially in regions with high flow rates. This may lead to underestimation of the CBF and can be an additional explanation for the different CBF values between standard pCASL and te-pCASL.

Because of the different objectives of the te-pCASL scan (measurement of ATT) and the standard pCASL sequence (measurement of CBF), the labeling durations of the two sequences differed to a great extent; 50 ms was chosen for each block of the te-pCASL sequence to provide sufficient temporal resolution, whereas 3000 ms was used in the standard pCASL sequence to quantify perfusion as suggested in the literature.[22] This resulted in a large raw ASL signal difference between the te-pCASL data and the standard pCASL data (around 24 times higher for standard pCASL, data not shown). Noisy MRI data can be biased by the Rician distribution of the noise, but when the SNR is higher than 2, the noise distribution is nearly Gaussian.[33] Therefore, to ensure that the te-pCASL signal is not subjected to a noise dependent bias, we quantified the noise in the decoded Hadamard images. The whole-brain average ASL SNR was higher than 2 for all time-points after arrival of the label (data not shown), which allows to confirm the normal distribution of decoded te-pCASL data. This implies that the ATT as obtained by fitting the Buxton-model can be trusted, even though the SNR of decoded te-pCASL data (<5) was much lower than that of standard pCASL data (~38).

Another improvement that could be made is to fit a Buxton model extended with dispersion of the blood arrival times.[34] In figure 4, it can be seen that the second part of the model, representing arrival of label, does not accurately fit the data. In particular, in the cortex the model is inaccurate. The model assumes that labeled blood arrives non-dispersed, and as such it contains a boxcar input function. However, it may be reasonable to assume that blood in the center of the vessel travels faster than blood at the vessel wall, resulting

in a dispersed arrival. Especially in the cortex, since it has later arrival times, and thus the labeled blood has longer time to disperse. Inclusion of dispersed arrival in the model would probably lead to a better fit of the model to the data.

With aging, CBF in the human brain has been shown to decrease, also with imaging modalities different from MRI.[35–37] In case of neurological disease, such as Alzheimer's disease, CBF is even further reduced.[1] Even though the evidence is less strong, both vascular and tissue transit times have been shown to increase with age.[37] It has been reported that CBF in WT mice is maintained, as opposed to several mouse models of neurological disease, which show decreased CBF with age.[38] Our experiments also did not show an effect of aging on the CBF in WT mice. Additionally, our results indicated that ATT is also preserved with aging in WT mice. Therefore, in future studies it may be of interest to investigate whether there is an age-dependent change in ATT in mouse models of neurological disease.

In conclusion, this study shows the successful implementation of te-pCASL in mice. For the first time, ATT was measured in mice and changes in ATT as a function of age were assessed. No differences were found in CBF or in ATT between old (25 months) and young (6 months) mice. te-pCASL and standard pCASL CBF values were different, probably due to a vascular contribution and the venous outflow of labeled spins.

ACKNOWLEDGEMENTS

REFERENCES

1. Wolk DA, Detre JA. Arterial spin labeling MRI: an emerging biomarker for Alzheimer's disease and other neurodegenerative conditions. *Curr Opin Neurol* 2012; 25: 421–8.
2. Iturria-Medina Y, Sotero RC, Toussaint PJ, *et al.* Early role of vascular dysregulation on late-onset Alzheimer's disease based on multifactorial data-driven analysis. *Nat Commun* 2016; 7: 11934.
3. Xekardaki A, Rodriguez C, Montandon M-L, *et al.* Arterial spin labeling may contribute to the prediction of cognitive deterioration in healthy elderly individuals. *Radiology* 2015; 274: 490–9.
4. Alsop DC, Detre JA. Reduced transit-time sensitivity in noninvasive magnetic resonance imaging of human cerebral blood flow. *J Cereb Blood Flow Metab* 1996; 16: 1236–1249.
5. Hendrikse J, van Osch MJP, Rutgers DR, *et al.* Internal carotid artery occlusion assessed at pulsed arterial spin-labeling perfusion MR imaging at multiple delay times. *Radiology* 2004; 233: 899–904.
6. Thomas DL, Lythgoe MF, van der Weerd L, *et al.* Regional Variation of Cerebral Blood Flow and Arterial Transit Time in the Normal and Hypoperfused Rat Brain Measured Using Continuous Arterial Spin Labeling MRI. *J Cereb Blood Flow Metab* 2006; 26: 274–282.
7. Günther M. Highly efficient accelerated acquisition of perfusion inflow series by Cycled Arterial Spin Labeling. In: *Proceedings of the 16th Annual Meeting of ISMRM*. Berlin, 2007.
8. Dai W, Shankaranarayanan A, Alsop DC. Volumetric measurement of perfusion and arterial transit delay using hadamard encoded continuous arterial spin labeling. *Magn Reson Med* 2013; 69: 1014–1022.
9. Wells J a., Lythgoe MF, Gadian DG, *et al.* In vivo Hadamard encoded Continuous arterial spin labeling (H-CASL). *Magn Reson Med* 2010; 63: 1111–1118.
10. Teeuwisse WM, Schmid S, Ghariq E, *et al.* Time-encoded pseudocontinuous arterial spin labeling: Basic properties and timing strategies for human applications. *Magn Reson Med* 2014; 00: 1–11.
11. Dai W, Garcia D, De Bazelaire C, *et al.* Continuous flow-driven inversion for arterial spin labeling using pulsed radio frequency and gradient fields. *Magn Reson Med* 2008; 60: 1488–1497.
12. Jahanian H, Noll DC, Hernandez-Garcia L. B_0 field inhomogeneity considerations in pseudo-continuous arterial spin labeling (pCASL): effects on tagging efficiency and correction strategy. *NMR Biomed* 2011; 24: 1202–1209.
13. Luh WM, Talagala SL, Li TQ, *et al.* Pseudo-continuous arterial spin labeling at 7 T for human brain: Estimation and correction for off-resonance effects using a Prescan. *Magn Reson Med* 2013; 69: 402–410.
14. Hirschler L, Debacker C, Voiron J, *et al.* Inter-Pulse Phase Corrections for Unbalanced Pseudo-Continuous Arterial Spin Labeling at High Magnetic Field. *Magn Reson Med*; In press. Epub ahead of print 2017. DOI: https://doi.org/10.1002/mrm.26767.
15. Franklin K, Paxinos G. *The Mouse Brain in Stereotaxic Coordinates*. third. 2007.
16. Klein S, Staring M, Murphy K, *et al.* elastix: A Toolbox for Intensity-Based Medical Image Registration. *IEEE Trans Med Imaging* 2010; 29: 196–205.
17. Buxton RB, Frank LR, Wong EC, *et al.* A general kinetic model for quantitative perfusion imaging with arterial spin labeling. *Magn Reson Med* 1998; 40: 383–96.
18. Dobre MC, Ugurbil K, Marjanska M. Determination of blood longitudinal relaxation time (T1) at high magnetic field strengths. *Magn Reson Imaging* 2007; 25: 733–735.
19. Herscovitch P, Raichle ME. What is the correct value for the brain--blood partition coefficient for water? *J Cereb Blood Flow Metab* 1985; 5: 65–69.

2

20. Alsop DC, Detre JA, Golay X, *et al.* Recommended implementation of arterial spin-labeled perfusion MRI for clinical applications: A consensus of the ISMRM perfusion study group and the European consortium for ASL in dementia. *Magn Reson Med*. Epub ahead of print 8 April 2014. DOI: 10.1002/mrm.25197.

21. Barbier EL, Silva AC, Kim SG, *et al.* Perfusion imaging using dynamic arterial spin labeling (DASL). *Magn Reson Med* 2001; 45: 1021–1029.

22. Duhamel G, Callot V, Tachrount M, *et al.* Pseudo-continuous arterial spin labeling at very high magnetic field (11.75 T) for high-resolution mouse brain perfusion imaging. *Magn Reson Med* 2012; 67: 1225–36.

23. Dorr A, Sled JG, Kabani N. Three-dimensional cerebral vasculature of the CBA mouse brain: a magnetic resonance imaging and micro computed tomography study. *Neuroimage* 2007; 35: 1409–23.

24. Wang J, Alsop DC, Song HK, *et al.* Arterial transit time imaging with flow encoding arterial spin tagging (FEAST). *Magn Reson Med* 2003; 50: 599–607.

25. Ye FQ, Mattay VS, Jezzard P, *et al.* Correction for vascular artifacts in cerebral blood flow values measured by using arterial spin tagging techniques. *Magn Reson Med* 1997; 37: 226–35.

26. Wells JA, Lythgoe MF, Choy M, *et al.* Characterizing the origin of the arterial spin labelling signal in MRI using a multiecho acquisition approach. *J Cereb Blood Flow Metab* 2009; 29: 1836–1845.

27. Liu P, Uh J, Lu H. Determination of spin compartment in arterial spin labeling MRI. *Magn Reson Med* 2011; 65: 120–127.

28. Wells JA, Siow B, Lythgoe MF, *et al.* Measuring biexponential transverse relaxation of the ASL signal at 9.4T to estimate arterial oxygen saturation and the time of exchange of labeled blood water into cortical brain tissue. *J Cereb Blood Flow Metab* 2013; 33: 215–24.

29. Schmid S, Teeuwisse WM, Lu H, *et al.* Time-efficient determination of spin compartments by time-encoded pCASL T2-relaxation-under-spin-tagging and its application in hemodynamic characterization of the cerebral border zones. *Neuroimage* 2015; 123: 72–79.

30. Chappell MA, MacIntosh BJ, Donahue MJ, *et al.* Separation of macrovascular signal in multi-inversion time arterial spin labelling MRI. *Magn Reson Med* 2010; 63: 1357–65.

31. Parkes LM, Tofts PS. Improved accuracy of human cerebral blood perfusion measurements using arterial spin labeling: Accounting for capillary water permeability. *Magn Reson Med* 2002; 48: 27–41.

32. Wegener S, Wu W-C, Perthen JE, *et al.* Quantification of rodent cerebral blood flow (CBF) in normal and high flow states using pulsed arterial spin labeling magnetic resonance imaging. *J Magn Reson Imaging* 2007; 26: 855–62.

33. Gudbjartsson H, Patz S. The Rician distribution of noisy MRI data. *Magn Reson Med* 1995; 34: 910–4.

34. Hrabe J, Lewis DP. Two analytical solutions for a model of pulsed arterial spin labeling with randomized blood arrival times. *J Magn Reson* 2004; 167: 49–55.

35. Leenders KL, Perani D, Lammertsma AA, *et al.* Cerebral blood flow, blood volume and oxygen utilization. Normal values and effect of age. *Brain* 1990; 27–47.

36. Pagani M, Salmaso D, Jonsson C, *et al.* Regional cerebral blood flow as assessed by principal component analysis and (99m)Tc-HMPAO SPET in healthy subjects at rest: normal distribution and effect of age and gender. *Eur J Nucl Med Mol Imaging* 2002; 29: 67–75.

37. Liu Y, Zhu X, Feinberg D, *et al.* Arterial spin labeling MRI study of age and gender effects on brain perfusion hemodynamics. *Magn Reson Med* 2012; 68: 912–22.

38. Maier FC, Wehrl HF, Schmid AM, *et al.* Longitudinal PET-MRI reveals β-amyloid deposition and rCBF dynamics and connects vascular amyloidosis to quantitative loss of perfusion. *Nat Med* 2014; 20: 1485–1492.

3

Influence of different isoflurane anesthesia protocols on murine cerebral hemodynamics measured with pseudo-continuous arterial spin labeling

Leon P. Munting[1,2*], Marc P.P. Derieppe[1,3*], Ernst Suidgeest[1], Baudouin Denis de Senneville[4,5], Jack A. Wells[6], Louise van der Weerd[1,2**]

[1]Department of Radiology, Leiden University Medical Center, Leiden, the Netherlands
[2]Department of Human Genetics, Leiden University Medical Center, Leiden, the Netherlands
[3]Prinses Máxima Center for Pediatric Oncology, University Medical Center Utrecht, Utrecht, the Netherlands
[4]Department of Radiotherapy, University Medical Center Utrecht, Utrecht, Netherlands
[5]Institut de Mathématiques de Bordeaux, Université Bordeaux/CNRS UMR 5251/INRIA Bordeaux-Sud-Ouest, France
[6]Division of Medicine, UCL Centre for Advanced Biomedical Imaging, University College London, London, United Kingdom

*Both authors contributed equally

**Corresponding author:
Dr. Louise van der Weerd
Leiden University Medical Center, Albinusdreef 2, 2333 ZA Leiden, the Netherlands
Email: L.van_der_Weerd@lumc.nl

ABSTRACT

Arterial Spin Labeling (ASL)-MRI can non-invasively map cerebral blood flow (CBF) and cerebrovascular reactivity (CVR), potential biomarkers of cognitive impairment and dementia. Mouse models of disease are frequently used in translational MRI studies, which are commonly performed under anesthesia. Understanding the influence of the specific anesthesia protocol used on the measured parameters is important for accurate interpretation of hemodynamic studies with mice. Isoflurane is a frequently used anesthetic with vasodilative properties. Here, the influence of three distinct isoflurane protocols was studied with pseudo-continuous ASL in two different mouse strains. The first protocol was a free-breathing set-up with medium concentrations, the second a free-breathing set-up with low induction and maintenance concentrations and the third a set-up with medium concentrations and mechanical ventilation. A protocol with the vasoconstrictive anesthetic medetomidine was used as a comparison. As expected, medium isoflurane anesthesia resulted in significantly higher CBF and lower CVR values than medetomidine (median whole-brain CBF of 157.7 *vs* 84.4 mL/100 g/min and CVR of 0.54 *vs* 51.7 % in C57BL/6J mice). The other two isoflurane protocols lowered the CBF and increased the CVR values compared to medium isoflurane anesthesia, without obvious differences between them (median whole-brain CBF of 138.9 *vs* 131.7 mL/100 g/min and CVR of 10.0 *vs* 9.6 %, in C57BL/6J mice). Furthermore, CVR was shown to be dependent on baseline CBF, regardless of the anesthesia protocol used.

INTRODUCTION

Cerebral blood flow (CBF) and cerebrovascular reactivity (CVR) are emerging as potential biomarkers for cognitive impairment and dementia.[1,2] They can be measured in the clinic[3] and in pre-clinical research[4,5] by means of MRI-based perfusion imaging. The arterial spin labeling (ASL) MRI technique is particularly attractive as it is completely non-invasive, using blood water as an endogenous tracer. This enables repeated measures for dynamic recordings of responses to stimuli such as a "CO_2 challenge" for assessment of cerebrovascular reactivity (CVR).

Mouse models are important tools for translational neuroscience and neurology. Although MRI studies with awake mice have been performed,[6,7] this approach is often tied to ethical and technical restrictions that heavily restrict practical application. Therefore, mouse MRI is commonly performed under anesthesia. However, anesthesia protocols are known to influence cerebral hemodynamics. In order to more clearly relate MRI measures of brain hemodynamics obtained from mouse models to clinical data and for meaningful comparison with other pre-clinical studies, it is important to understand the hemodynamic influence of the different anesthesia protocols used. Furthermore, different mouse strains may vary in their response to the anesthesia protocol used.[8,9] It is therefore important to devise standardized protocols in order to provide comparable and reproducible CBF and CVR estimates. Isoflurane is the most widely used anesthetic in imaging studies with mice, likely due to its very straightforward method of administration, fast reversibility and the minimal long-term side-effects, even upon repeated use in the same animal.[10] However, isoflurane also has a dose-dependent vasodilatory effect,[11] as well as a dose-dependent respiratory depressive effect.[12,13] Thus it has been posited to reduce the dynamic range in ASL-based CVR studies, both directly via its vasodilatory effect and – if not ventilated - indirectly via an increase in the partial pressure of arterial pCO_2 as a consequence of respiratory depression.

BOLD-fMRI studies also appear to be impaired by isoflurane in a dose dependent manner, as stimulus-evoked BOLD-responses and resting state network organization have been shown to be reduced when higher levels of isoflurane were used.[14,15] In order to benefit from its otherwise favorable characteristics, refinements have been proposed to minimize the needed dose of isoflurane. For example, combining it with a low-dose of medetomidine permits stable anesthesia at 0.5 % of isoflurane.[16] Also, isoflurane has been combined with the paralysis agent pancuronium-bromide to support mechanical ventilation, with maintenance levels of 1.0 %.[17] However, combination with paralyzing agents or medetomidine may not always be wanted, due to ethical reasons or unresponsiveness of the mouse strain used respectively.[9] Alternatively, Wells *et al.* showed that by simply administering a relatively low concentration of isoflurane both during induction (2.0 %)

and maintenance (1.5 %) - without any other anesthetic - workable CVR values can be obtained in an ASL-based CVR study.[18]

In this work we provide the first comprehensive assessment of CBF and CVR in the mouse brain under different anesthetic regimes using pseudo-continuous ASL-MRI in C57BL/6J mice. In particular, given the prevalence and unique perks of isoflurane anesthesia, we compare three distinct isoflurane-based protocols: i) a free breathing isoflurane protocol with doses that reflect commonly used isoflurane concentrations in mouse brain MRI studies[9,19], defined henceforth as the "medium-dose" protocol; ii) the protocol described by Wells *et al.,*[18] where a relatively low dose of isoflurane was used for both induction and maintenance, defined henceforth as the "low-dose" protocol; iii) a medium-dose isoflurane protocol with mechanical ventilation to counteract the respiratory depressive effect. Additionally, we compare the three isoflurane protocols to a medetomidine anesthesia protocol, which is known to be vasoconstrictive. Furthermore, we evaluate the low-dose and ventilated isoflurane protocols in a second mouse strain, partly on a C3H/HeJ background, a strain with known respiratory anomalies.[20]

EXPERIMENTAL

This study was performed in compliance with the guidelines of the European community for the care and use of laboratory animals (EUVD 86/609/EEC) and reported conform the ARRIVE guidelines.[21]

Animal procedures. All experiments were approved by the local ethics committee "Instantie voor Dierenwelzijn" of the Leiden University Medical Center and were performed under DEC permits 11165 and 14073.

33 wild type C57BL/6J mice (31 males, 2 females) were used at 10.7 months (standard deviation [SD] 6.5 months), with a mean weight of 35 grams (SD 6 grams). The second wild type strain used in this study was the F2 generation of a cross of C57BL/6J and C3H/HeJ mice, further referred to as B6C3. 11 B6C3 mice (7 males, 4 females) were used at 13.5 months (SD 0.5 months), with a mean weight of 46 grams (SD 7 grams). The mice were derived from an in-house breeding. Founder mice were obtained from the Jackson Laboratory (Bar Harbor, ME, USA). The mice were co-housed in individually ventilated cages (2-4 per cage) in a 12 h dark/ light cycle-ML2-facility. They had unlimited chow food and water at their disposal and were supplied with bedding material and cage enrichment.

Anesthesia and monitoring of the physiological signals. The following four anesthesia protocols were used (dose, route of administration, animal number and age per group are summarized in supplementary table 1):

1) An isoflurane protocol with commonly used doses in mouse brain MRI studies:[9,19] 3.5 % induction for 4 minutes and 1.5-2.0 % maintenance; during maintenance the breathing rate was kept between 80 and 100 bpm by adjusting the isoflurane accordingly between 1.5-2.0 %. The isoflurane was administered in medical air enriched with oxygen (air:oxygen 3:1). This protocol is referred to as the medium-dose isoflurane protocol.

2) An isoflurane protocol with 2.0 % induction for 5 minutes and 1.25 % maintenance, based on the protocol described in Wells *et al.*[18] However, to restrict the accumulation of isoflurane even more, the maintenance concentration was lowered to 1.25 % (instead of 1.50 % in Wells *et al.*), which was the minimum in our hands. Some B6C3 animals required slightly longer induction times to be sufficiently anesthetized. For both strains, a quick transfer from the induction box to the animal bed of the MRI setup was necessary to prevent awakening. The isoflurane was administered in pure medical air, in accordance with Wells *et al.*[18] This protocol is referred to as the low-dose isoflurane protocol.

3) An isoflurane protocol with 3.5 % induction for 4 minutes, 1.75 % maintenance and intubation and mechanical ventilation. After induction, the mouse was taken out of the induction box and transferred to a supine position and supplied with a nose cone with continued 3.5 % isoflurane administration. The trachea was subsequently endotracheally intubated, after which the mouse was transferred to the scanner bed and the isoflurane was then decreased to 1.75 %. There, the mechanical ventilation was started with a CWE MRI-1 ventilator (Ardmore, USA) with settings as recommended during the *functional MRI in mice* workshop in November 2016 at the animal imaging center of the ETH Zürich, Switzerland: a rate of 80 bpm, a tidal volume of 1.7 mL and inspiration of 25 %. The animal was not paralyzed during the scan. Both the gas used during induction and the air used during ventilation consisted of oxygen-enriched medical air (air:oxygen 3:1). This protocol is referred to as the medium-dose isoflurane + ventilation protocol.

4) A medetomidine protocol. Here, anaesthesia was also induced with 3.5 % isoflurane in oxygen-enriched medical air (air:oxygen 3:1) for 4 minutes. After transfer to the animal bed, the isoflurane was decreased to 2.0 %, and after finalizing the setup, a subcutaneous catheter was inserted in the flank of the animal. Then a 0.15 mg/kg bolus of dexmedetomidine-hydrochloride was given (Dexdomitor®, Vetoquinol SA, Lure, France [a solution without levomedetomidine]), followed 10 minutes later by 0.30 mg/kg/hr infusion with a syringe pump (Univentor© 802, Univentor© High Precision Instruments, Zejtun, Malta). Note that this is equivalent to a 0.30 mg/kg bolus and 0.60 mg/kg/hr

3

infusion protocol when a mixture of both active (dexmedetomidine) and inactive (levomedetomidine) enantiomers is used. During the 10 minutes between bolus and infusion, the isoflurane was decreased to 0 %, but the administration of oxygen-enriched air was continued. The protocol is based on the optimal findings in the medetomidine optimization study by Adamczak *et al.*[22] This protocol is referred to as the medetomidine protocol.

For physiological monitoring, heart and respiration rates were captured respectively with a pressure sensitive pad below the animal and a pulse oxygenation probe around the hind paw (SA instruments, New York, USA). Temperature was maintained around 36.5 C with a water bed plugged on a feedback control system (Medres, Cologne, Germany). Furthermore, a transcutaneous probe (Radiometer®, Zoetermeer, The Netherlands) was applied on the shaved flank of the mouse for non-invasive collection of the transcutaneous partial pressure in carbon dioxide (tc-pCO_2). As absolute arterial pCO_2 values are not reflected by the tc-pCO_2 values, whereas changes in arterial pCO_2 are reflected by changes in tc-pCO_2,[23] the tc-pCO_2 plots are shown as absolute change of tc-pCO_2 in mmHg during challenge relative to baseline. Due to a technical error during the medetomidine scans, 7 out of the 11 tc-pCO_2 profiles were not captured in this group. For each anesthesia protocol, representative CBF, heart rate, respiration rate and tc-pCO_2 time-profiles are shown in supplementary figure 1. In a few animals, parts of the heart or respiration rate time-profiles were not captured properly, as illustrated in supplementary figure 1. Such incorrectly sampled data was excluded from the median and interquartile range (iqr) calculation of the heart and respiration rates, which is shown in supplementary table 2.

MRI measurements. A 7 Tesla Pharmascan (Bruker Biospin GmbH, Ettlingen, Germany) was used with a 23 mm volume resonator.

Anatomical scans. For planning of the pCASL sequence, anatomical T_2-weighted magnitude images were acquired with a RARE sequence in the axial, sagittal and coronal orientation, using the following parameters: TE/TR/FA = 35.0 ms/2,500 ms/90 degrees, matrix 256x256, field of view of 21.55 x 21.55 mm, 0.7 mm slice thickness, no slice gap, 1 average, RARE factor of 8, and a bandwidth of 36.7 kHz. Additionally, a set of anatomical images with the same geometry as the pCASL read-out was acquired for registration purposes.

Cerebral blood flow measurements. A pCASL sequence allowed measuring the cerebral blood flow. The pCASL-interpulse phases were optimized to correct for off-resonance effects with pre-scans.[24] Labeling pulses were applied with 3.5 µT B1, 400/800 µs pulse duration/interval and a total labeling duration (τ) of 3000 ms. A post-label delay (PLD) of 300 ms was included before a single-shot spin echo – echo planar imaging (EPI) read-out. The following read-out parameters were used: TE/FA = 16.8 ms/90 degrees, 4 dummy

scans, matrix size 96 x 96, FOV 21.55 x 21.55 x 1.5 mm, 3 slices with the middle slice position at -0.75 mm Bregma and at the isocenter of the bore and a maximum/average labeling gradient of 45.0 / 5.0 mT/m. The labeling slice was always positioned exactly 1.0 cm from the middle imaging slice, which is around 4 mm upstream of the split of the common carotid artery. The TR was 3,520 ms, meaning that each control/labelled pair of images took of 7.04 seconds to acquire. An example of the planning and the resulting ASL images is shown in supplementary figure 2.

To support CBF-quantification, tissue T_1 (T_1t) maps were acquired with an inversion recovery EPI sequence with 18 inversion times and labeling efficiency (α) was measured in the carotids 3 mm downstream of the labeling plane with a flow-compensated, ASL-encoded FLASH sequence.

Timeline of the CBF measurements. CBF time-profiles were acquired for 21 minutes separated in 3 fragments of 7 minutes: 7 minutes baseline, 7 minutes 7.5 % CO_2 challenge, 7 minutes back to baseline. This duration was chosen to collect 60 repetitions for each fragment of the sequence, thus with a total of 180 repetitions. During the challenge, the oxygen concentration stayed the same, *i.e.* 7.5 % CO_2 replaced N_2 in the air mixture.

Image processing

Alignment of the pCASL and inversion recovery EPIs. A MATLAB® monomodal rigid-body registration (300 iterations) was applied on the label and control magnitude images collected by the pCASL sequence to align them to the first label magnitude image of the sequence. In the same way, the 18 inversion recovery EPIs were aligned to the first label magnitude image of the pCASL sequence. The CBF and T_1t maps could then be computed voxel wise.

Cerebral blood flow quantification. The CBF was quantified in mL/100 g/min using Buxton's general kinetic perfusion model.[25] Assuming that M_{0b}, the magnetization of arterial blood at thermal equilibrium, may be approximated by M_{0t}/λ, where M_{0t} is the magnetization of tissue and λ is the blood–brain partition coefficient of water, i.e. 0.9 mL/g,[26] the following equation was used:

$$\text{CBF} = \frac{\lambda \cdot \Delta M \cdot \exp(\text{PLD}/T_{1b})}{2 \cdot \alpha \cdot T_{1t} \cdot M_{0t} \cdot \left(1 - \exp(-\tau/T_{1t})\right)} \quad (1)$$

Where ΔM is the measured difference between label and control acquisition and T_1b is 2230 ms, the longitudinal relaxation time of blood at 7 T.[27]

Delineation of the brain regions. The anatomical T_2-weighted magnitude images in one dataset of the study served as the basis for the delineation of the full brain and the cortex.

These brain regions were then automatically propagated to the anatomical T_2-weighted magnitude images of the other datasets by applying a monomodal optical-flow registration algorithm. The field of transport $\vec{V}$ was thus estimated on a pixel-by-pixel basis by means of the following minimization process:

$$arg\min_{\vec{v}} \int_{\Omega} \left| I_t + \vec{V} \cdot \vec{\nabla} I \right| + \alpha \left(\left\| \vec{\nabla} u \right\|_2^2 + \left\| \vec{\nabla} v \right\|_2^2 \right) d\vec{r} \quad (2)$$

where $\Omega \subseteq \mathbb{R}^2$ is the image coordinate domain, I_t the temporal partial derivative of the image intensity I calculated between the timepoints t and $t+\delta t$, (u,v) the estimated

components of transport vectors, and $\vec{r} \in \Omega$ the spatial location. The minimized functional accounts for the two following additive contributions: 1) a data fidelity term (left part of the integral in Eq. (2)) that measures, through a L^1 norm, the similarity between the images, 2) a regularization term (right part of the integral in Eq.(2)) designed to provide a sufficient conditioning to the numerical scheme. The regularization term is given by

$\left\| \vec{\nabla} u \right\|_2^2 = u_x^2 + u_y^2$ and $\left\| \vec{\nabla} v \right\|_2^2 = v_x^2 + v_y^2$, $u_x u_x$, $u u_{y'}$, $v_x v_x$ and $v v_{x'}$ being the spatial partial derivatives of u and v, respectively. The regularization term alpha was set to 0.5. The results of this propagation step was then verified dataset-by-dataset by an operator (LPM). In each dataset, the in-plane spatial transformation between the anatomical T_2-weighted magnitude image and the first frame of the pCASL magnitude image (*i.e.*, the reference image chosen previously) was then automatically estimated as follows: an edge-based variational method for non-rigid multimodal registration[28] was employed to circumvent potential geometrical distortions induced by the EPI readout. For this purpose, the data fidelity term in Eq. (2) (left part of the integral) was replaced by a multi-modal similarity metric which favors the alignment of edges/gradients that are present in both images, as described in Chen *et al.*[29] The obtained motion-vector field was subsequently employed to adjust the position of the masks of each brain region. Here again the results of this propagation step was verified dataset-by-dataset by an operator (LPM).

CVR quantification. The spatial mean of the CBF in each brain region was collected frame-by-frame, and allowed quantifying the CVR by computing the following estimates: 1) baseline CBF from the mean CBF of the 20 repetitions, *i.e.*, 2 min 20 sec, before the onset of the CO_2 challenge, and 2) CBF during CO_2 challenge based on the 20 repetitions before the end of the CO_2 challenge. The percentage of CVR was calculated by applying the following equation:

$$CVR\ (\%) = 100 * \left(\frac{\text{mean CBF during challenge}}{\text{mean baseline CBF}} - 1 \right) \quad (3)$$

Statistical analysis. Estimates are expressed as median (iqr), except for the time-profiles in the figures, which are given in mean (standard deviation [SD]) to better visualize the group response. The statistical tests were performed using the IBM SPSS statistics 23 software package (Armonk, New York, USA). For multiple comparisons, first a Kruskal-Wallis test was used to evaluate whether the non-parametric unpaired groups belonged to the same distribution. If a significant difference was found, post-hoc testing was performed with Dunn-Bonferroni tests to assess which groups differed. Mann-Whitney tests were used when only comparing two groups.

RESULTS

Comparison of the anesthesia protocols in C57BL/6J mice. The CBF time-profiles for the different anesthesia protocols are displayed in figure 1a and 1b for full brain ROIs and cortical ROIs respectively. CBF and CVR maps of individual mice representative for their groups and their respective anatomical T_2-weighted images are shown in figure 1c. The lowest baseline CBF estimates were found using the medetomidine protocol, and the highest when administering medium isoflurane. The other two isoflurane protocols are in between, without an obvious difference between the two. Figure 2a and 2b show CBF time-profiles normalized to the baseline CBF values for the full brain and cortex respectively. The resulting CVR values are compared in figure 2c and 2d with boxplots for respectively full brain and cortex. Here, an opposite trend is observed for the anesthesia protocols, with medium isoflurane resulting in the lowest CVR and medetomidine in the highest CVR. Again, the other two isoflurane protocols result in an intermediary CVR response, with similar results recorded.

The distribution of CBF and CVR values in both full brain and cortex for the four anesthesia protocols were significantly different from each other ($H(3) = 19.02$ & $p < 0.001$; $H(3) = 24.24$ & $p < 0.001$; $H(3) = 12.36$ & $p = 0.006$; $H(3) = 14.75$ & $p = 0.002$ respectively for full brain CBF, full brain CVR, cortical CBF and cortical CVR). Post-hoc analysis indicated that the CBF values in the full brain obtained under medetomidine (84.4 mL/100 g/min [31.4 mL/100 g/min]) were significantly lower than those obtained with medium isoflurane (157.7 mL/100 g/min [41.72 mL/100 g/min]) and significantly lower than those obtained under low isoflurane (138.9 mL/100 g/min [26.5 mL/100 g/min]), adj. $p = 0.001$ and adj. $p = 0.006$ respectively. Regarding the CVR values in the full brain, the same groups differed: medium isoflurane (0.5 % [3.1 %]) *vs.* medetomidine (51.7 % [25.7 %]), adj. $p < 0.001$; low isoflurane (10% [7.1%]) *vs.* medetomidine, adj. $p = 0.036$. Most of the other comparisons lost their statistical significance after Dunn-Bonferoni correction. For the low isoflurane and medium isoflurane + ventilation CBF and CVR comparisons however, even uncorrected p-values were not significant ($p = 0.688$ and $p = 0.974$ respectively), reflecting their similar

CBF time-profiles. In the cortical ROIs, statistical testing gave comparable results as in the full brain ROIs (data not shown). Median and interquartile ranges of the CBF and CVR values per anesthesia protocol are given in supplementary table 3.
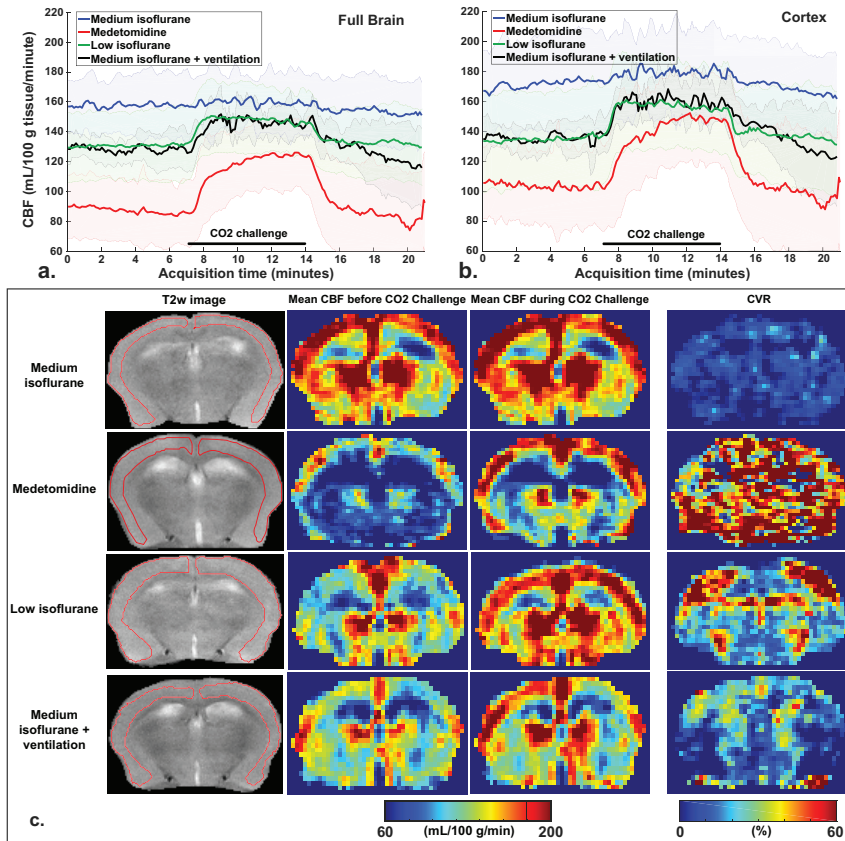

Figure 1: Absolute CBF values and CBF maps for the four different anesthesia protocols in C57BL/6J mice. a,b) Mean and standard deviation of the absolute CBF profiles in the full brain (a) and the cortex (b). c) Representative examples of images acquired at -0.75mm from Bregma. In the columns from left to right: anatomical images with cortical ROIs; mean CBF maps collected in the last 2 minutes before the onset of the CO_2 challenge; mean CBF maps collected in the last 2 minutes during CO_2 challenge; CVR maps. All the images on a row are from the same mouse.
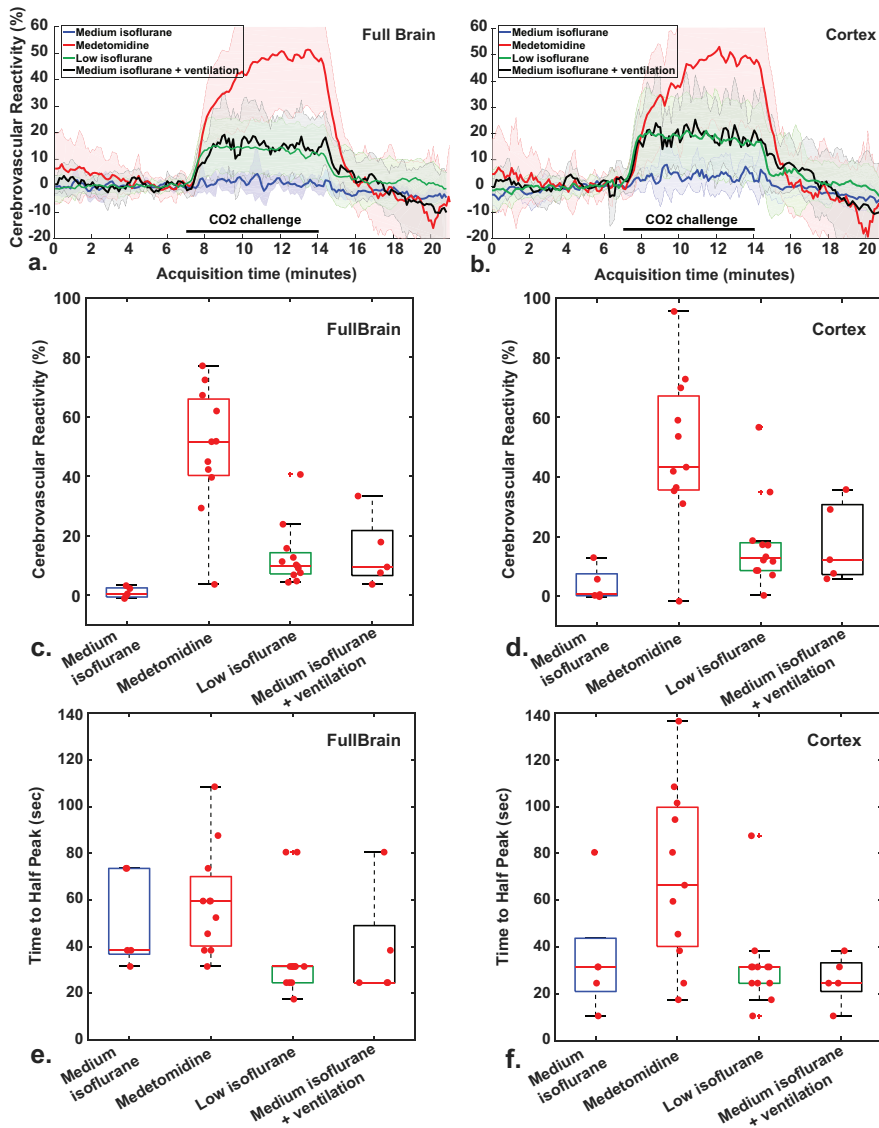
Figure 2: CVR relative to the baseline CBF for the four different anesthesia protocols in C57BL/6J mice. CVR estimates are computed in the full brain (a, c, e) and in the cortex (b, d, f).

It should be pointed out that in the medetomidine group, not all of the individual baseline CBF profiles were stable yet, even though the medetomidine infusion started 20 minutes before the pCASL scan (see supplementary figure 4). It is also to be noted that, unlike the isoflurane anesthesia protocols where the CVR is most pronounced in the cortex, the CVR obtained using the medetomidine protocol was strongly present throughout the full brain. Also observed in the CBF time-profile of medetomidine only, is a continuing CBF increase during hypercapnia, suggesting a competition between processes (vasoconstrictive medetomidine and vasodilative CO_2) influencing the CBF. This is reflected in the time to half peak (TTHP) distributions, which were also different between the anesthesia protocols, H(3) = 9.701 and p = 0.021 in the full brain and H(3) = 9.105; p = 0.028 in the cortex. Only the medetomidine *vs.* low isoflurane full brain TTHP post-hoc test survived the Dunn-Bonferoni correction, with an adj. p = 0.03.

There were no significant differences in the tc-pCO_2 rise upon CO_2 challenge between the different anesthesia protocols (supplementary figure 3, H(3) = 6.167; p = 0.104). The median heart rates were lower and respiration rates higher in the medetomidine group (supplementary table 2), which was to be expected given the known respiratory depressive action of isoflurane[12,13] and the known bradycardic action of medetomidine.[30]

Comparison of the anesthesia protocols in B6C3 *vs.* C57BL/6J mice. The B6C3 mice could not be sedated sufficiently with medetomidine, thus compromising the use of this anesthetic for this strain. The application of the low isoflurane protocol in free-breathing B6C3 mice showed a higher but non-significant mean baseline CBF in B6C3 mice compared to C57BL/6J mice (figure 3; full brain: U = 21.0; Z = -1.405; p = 0.180; cortex: U = 24.0; Z = -1.124; p = 0.291). Using the low isoflurane protocol, a significantly lower CVR in B6C3 mice was found *vs.* C57BL/6J mice: 3.1 % (4.6 %) *vs.* 10.0 % (7.1 %) in the full brain (U = 4.0; Z = -2.997; p = 0.001); and 4.5 % (1.1 %) *vs.* 12.7 % (9.3 %) in the cortex (U = 7.0; Z = -2.716 p = 0.005) (figure 3a-d). Interestingly, the change in tc-pCO_2 was also significantly lower in B6C3: mean rise of 18.6 mmHg in C57BL/6J mice vs 11.5 mmHg in B6C3 mice (Mann-Whitney, p = 0.014) (figure 3e). It is to be noted that B6C3 mice displayed a higher group variability in tc-pCO_2 rise, with a standard deviation of 6.1 mmHg (normalized standard deviation of 53 %) *vs.* 4.7 mmHg only in C57BL/6 mice (normalized standard deviation of 25 %) (figure 3e). When using medium isoflurane + mechanical ventilation, the difference in CVR in B6C3 mice *vs.* C57BL/6J mice was abolished: 6.8 % (12.1 %) *vs.* 9.6 % (15.1 %) in the full brain (U = 8.0; Z = -0.940; p = 0.421), and 4.4 % (17.5 %) *vs.* 12.2 % (23.5 %) in the cortex (U = 8.0; Z = -0.940; p = 0.421) (figure 4a-d). With mechanical ventilation, both strains displayed a similar tc-pCO_2 rise, with a mean rise of 13.2 mmHg (7.3) *vs.* 10.8 mmHg (6.8) in B6C3 mice (t-test, p = 0.595) (figure 4e).
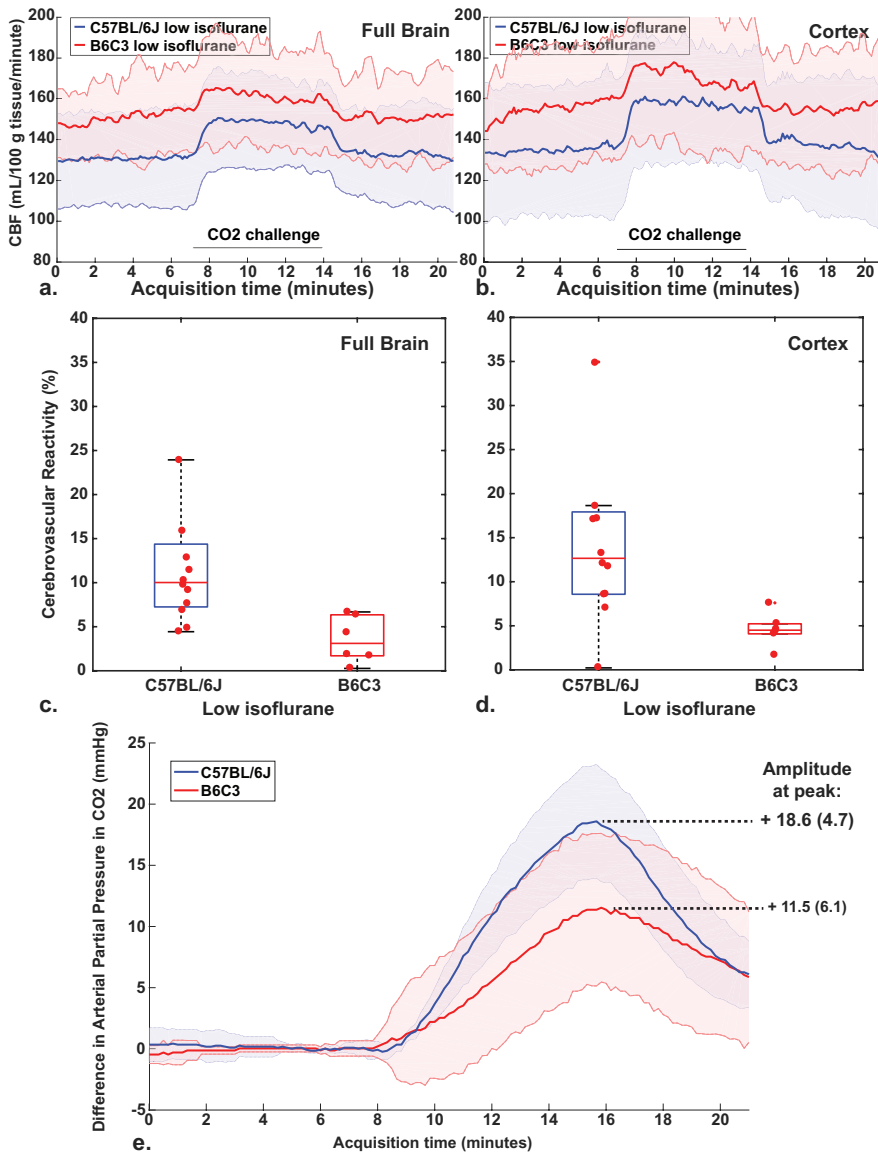
Figure 3: CBF and CVR values for the "low isoflurane" protocol in C57BL/6J mice (blue) vs B6C3 mice (red). Time profiles of the CBF acquired in the full brain (a) and in the cortex (b). The CVR is significantly different between both strains (c,d). The transcutaneous pCO_2 rise was significantly different at the time of maximum pCO_2 rise (e).
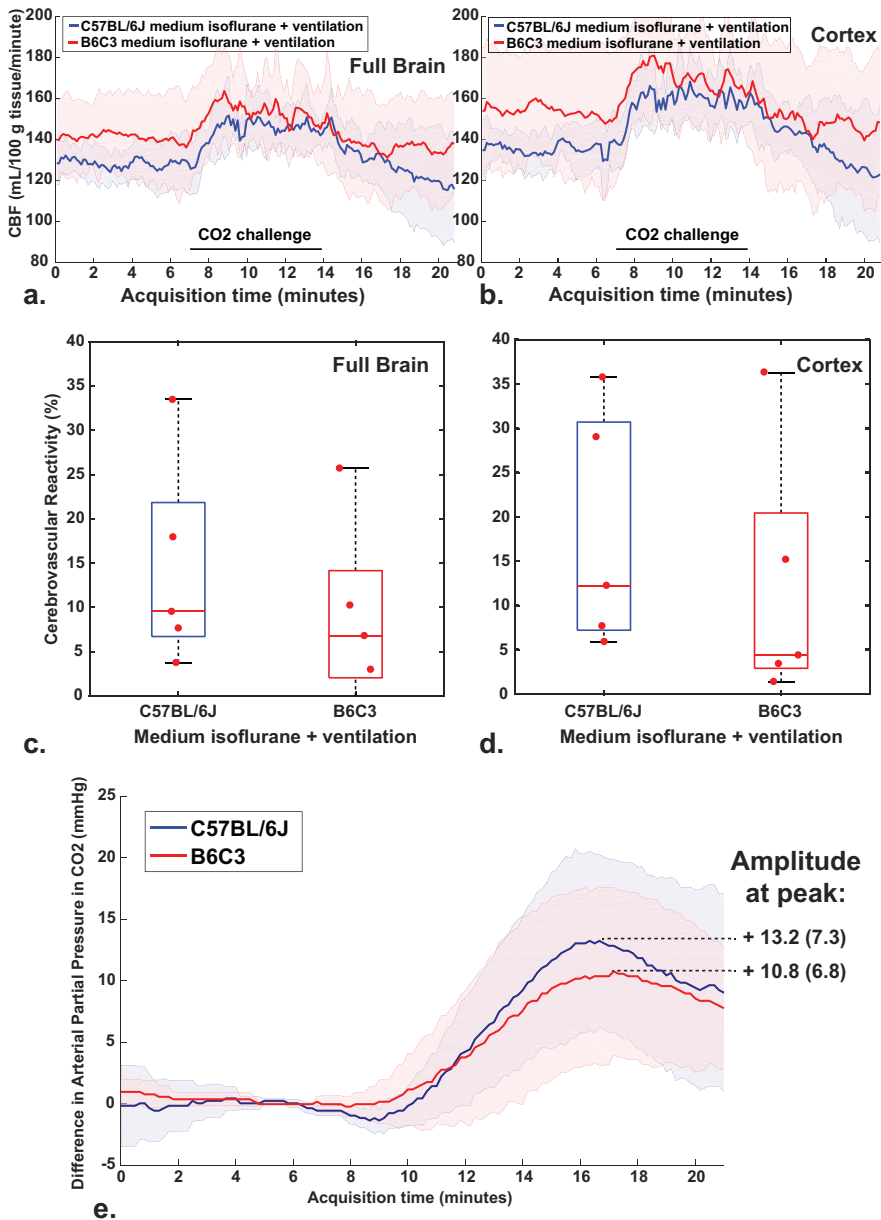
Figure 4: CBF and CVR for the "standard isoflurane + mechanical ventilation" protocol - C57BL/6J mice (blue) vs B6C3 mice (red). a-b) Time profiles of the CBF acquired in the full brain (a) and in the cortex (b). c-d) CVR in the full brain (c) and in the cortex (d), which are not significantly different in B6C3 vs. C57BL/6J mice. e) tc-pCO$_2$ rise in B6C3 vs. C57BL/6J mice was not significantly different.

End of the hemodynamic capacity reserve with high baseline CBF values

To visualize the dependency of CVR on baseline CBF, a correlation plot between the two is shown in figure 5. There is a strong negative correlation between baseline CBF and CVR, with high baseline CBF values resulting in a blunted or absent CVR response regardless of the protocol used, indicating the maximum of the hemodynamic capacity is reached. Only measurements in C57BL/6J mice were used for this plot.
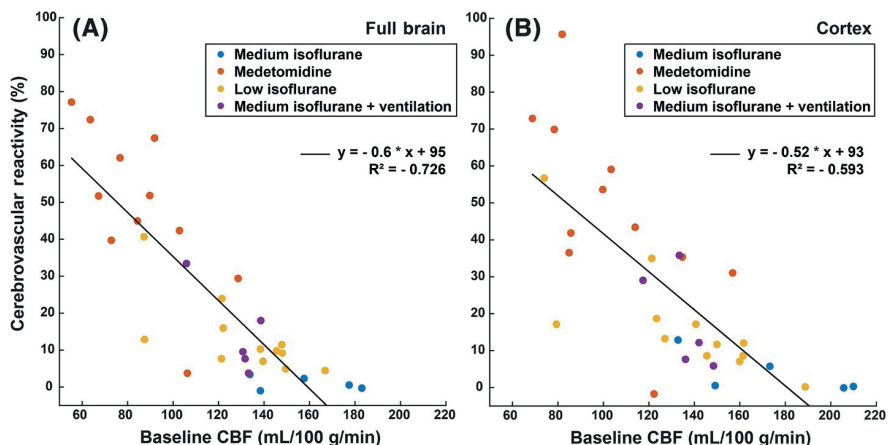

Figure 5: CVR expressed as a function of the baseline CBF in C57BL/6J mice. Every dot represents one mouse, where the colour indicates the anesthesia protocol used. Relation is given for the full brain (a) and for the cortex (b).

DISCUSSION

The current increase of studies investigating hemodynamics in the mouse brain requires a better understanding of the physiological influence of the anesthesia protocols used. Our results demonstrate exquisite sensitivity of CBF and CVR to the anesthesia protocol employed, findings that reinforce the need for care in the experimental design and interpretation of studies of murine cerebrovascular function, where anesthesia is often required. Isoflurane is the most widely used anesthestic due to its many advantages, but it has the disadvantage of being a dose-dependent vasodilator and a respiratory depressant. In this study, we focused on the influence of different isoflurane protocols on the hemodynamic measures CBF and CVR to a CO_2 stimulus. A medium-dose isoflurane protocol was compared with two alternative isoflurane protocols that have been adapted to minimize its vasodilatory and/or respiratory depressive properties: a low-dose isoflurane protocol and a medium-dose isoflurane protocol with mechanical ventilation. To put the results in context, the isoflurane protocols were also compared to the vasoconstrictive

medetomidine protocol. All four protocols were tested in the commonly used C57BL/6J mouse strain. Lastly, the performance of the adapted isoflurane protocols was also assessed in a second mouse strain, namely the mixed background B6C3 strain.

As reported before[9], the medium isoflurane protocol resulted in a high baseline CBF, thus blunting the CVR. Conversely, the medetomidine protocol yielded the lowest CBF and highest CVR, with median CVR estimates over 50 % in C57BL/6J mice. As intended, the adapted isoflurane protocols lowered basal CBF compared to the medium isoflurane protocol. Consequently, workable CVR values were obtained. There was no observable difference between the two adapted isoflurane protocols. This is interesting, because with the low isoflurane protocol, both the vasodilatory and the respiratory depressive effects are reduced compared to the medium isoflurane protocol, whereas with the medium isoflurane + ventilation protocol, only the respiratory depressive effects are reduced. Thus it implies that the respiratory depression plays a major role in the outcome of the high baseline CBF with the medium isoflurane protocol. Because of its much easier implementation, we recommend researchers unexperienced with intubation to use the low isoflurane protocol over the medium isoflurane + ventilation protocol for CVR studies with perfusion imaging. It should be stressed here, that in our experience, not only the low maintenance, but also the low induction is of high importance for maintaining some hemodynamic reserve capacity. Compared to the other protocols, the low induction keeps the respiration rate higher especially in the beginning of the anesthesia period, and fully avoids any spasmodic breathing. Also to be noted is that studies have been reported with lower maintenance concentrations than our low isoflurane protocol.[6,14] In our hands, we could not lower the isoflurane concentration, as animals would then have woken up. Perhaps local differences in isoflurane delivery systems can explain differences in lower boundaries of isoflurane maintenance. In supplementary table 4, a list of pros and cons of the different anesthesia protocols in this study are summarized.

A wider range of anesthetics has been used for rodent MRI studies than used here. Most of these anesthetics have been reported to affect hemodynamic regulation. For example, propofol reduces blood pressure and is respiratory depressive.[31,32] Other fluorinated gases than isoflurane such as halothane and sevoflurane have a similar hemodynamic influence as isoflurane.[33] Of particular interest are urethane and etomidate. These anesthetics are known to have very little effect on hemodynamics.[9,34,35] However, urethane is not applicable to longitudinal studies, due to the toxicity of the compound. Etomidate sedation has been suggested as a widely applicable anaesthesia regime in multiple strains.[9,35] It is even preferred for anesthesia induction of cardiac patients, due to its lack of hemodynamic influence.[36] However, the current availability of formulations of etomidate is very limited and, to the best of our knowledge, etomidate is only available in a concentration of 2 mg/mL. This means that injection volumes needed for at least one hour of sedation

exceed the animal welfare guidelines.[37] A very recent paper showed that it was possible to measure unilateral BOLD responses upon a somatosensory stimulus repeatedly in the same mouse anesthetized with a novel ketamine/xylazine formulation.[38] It would therefore be of interest to characterize the absolute CBF and CVR profiles with this new ketamine/xylazine formulation.

Unfortunately, B6C3 mice exhibited an insufficient anesthetic depth with medetomidine, thus compromising the use of this anesthetic for this strain. This insensitivity likely comes from the C3H strain. Medetomidine has been reported to show limited efficacy of anaesthesia not only in C3H mice but also in BTRB T+tf/J mice and CD1 strains[9]. Therefore, if medetomidine use is uncharacterized in a mouse strain, we recommend careful bench studies with frequent monitoring of anesthetic depth and physiological measures such as heart and respiration rate before starting an MRI experiment with medetomidine. Another limitation of medetomidine was the unstable baseline CBF that was sometimes observed in the C57Bl/6J mice. This is probably a result of the switch from isoflurane induction to medetomidine. The dynamics of CBF stabilization under medetomidine is not well-known and this might be interesting for future research. However, since the sedation time of medetomidine is limited (around 1 hour starting from the time of bolus injection[22]), it would be risky to delay the start of the pCASL scan, as the animal may wake up before the end of the scan.

A different complication with the CVR measurements was encountered when using the low isoflurane protocol in free-breathing B6C3 mice. Here, a CBF response to CO_2 was nearly absent (3.1 % CVR). Interestingly, when comparing the mean tc-pCO_2 increase with the same hypercapnia protocol in free-breathing mice, B6C3 mice also had a significantly lower tc-pCO_2 increase compared to C57BL/6J mice (11.5 mmHg *vs.* 18.6 mmHg). When the B6C3 mice were mechanically ventilated, both the difference in CVR and tc-pCO_2 between B6C3 and C57BL/6J mice were abolished. It has been reported before that C3H mice have a low respiratory sensitivity to hypercapnic stimulation.[20] However, it seems paradoxical that a lower tc-pCO_2 increase is measured in free-breathing mice with a lower respiratory response to CO_2, as a lower respiratory response is expected to less efficiently remove CO_2 from the body. Further research is therefore necessary to clarify if and how the reduced CVR, reduced tc-pCO_2 rise and low respiratory sensitivity to hypercapnia in the B6C3 mice anesthetized with low isoflurane are related. Whole-body plethysmography to measure minute ventilation as well as more reliable pCO_2 measurements such as end-tidal CO_2 or blood sampling could give more insight in this matter. Also to be taken into account is that factors such as skin perfusion influence the diffusion of CO_2 through the skin,[23] which might in their turn be influenced by the anesthesia protocol used. This may bias the tc-pCO_2 measurements, which is why we chose not to express CVR per mmHg rise of transcutaneous CO_2.

A few limitations specific to this study have to be taken into account. The large age range of the animals and the different oxygen content in the low isoflurane protocol (20 % versus around 40 % O2 in the other protocols) might have biased the results. However, this bias is probably small, as several studies have shown that brain hemodynamic parameters are preserved with age in wild type mice,[5,39,40] and because the effect of 100 % O2 inhalation on the baseline CBF has been shown to be an order of magnitude lower than that of hypercapnia.[41] Another limit is that due to technical constraints the labeling efficiency was only measured in the carotids, and not in the vertebral arteries. This might have introduced noise in the CBF values of the flow territory of the vertebral arteries (the posterior part of the brain), but this is not expected to be different between groups. Lastly, the absence of paralysis in the mechanically ventilated animals sometimes resulted in counter-breathing, especially during the CO_2-administration, probably explaining the more fluctuating CBF time-profile in this group.

In conclusion, this study stresses the importance of careful selection of the specific anesthesia protocol for CBF and/or CVR studies in the mouse brain. From the four protocols tested, the medetomidine protocol showed the lowest CBF and highest CVR values, as expected given medetomidine's vasoconstrictive properties. However, an important limitation is that medetomidine induces insufficient depth of anaesthesia in several mouse strains. Despite the known vasodilative properties of isoflurane, CVR studies were possible with the two adapted isoflurane protocols, with comparable CVR values in C57BL/6J mice. Of these two, the free-breathing low isoflurane protocol may experimentally provide the most straight-forward protocol. With this protocol, it is important that the isoflurane dose is kept low during both induction and maintenance. Furthermore, CVR was shown to be highly dependent on the baseline CBF, with high baseline CBF resulting in blunted CVR.

ACKNOWLEDGEMENTS

REFERENCES

1. Beishon L, Haunton VJ, Panerai RB, *et al.* Cerebral Hemodynamics in Mild Cognitive Impairment: A Systematic Review. J Alzheimers Dis. 2017 Jul 3;59(1):369–85.

2. Hays CC, Zlatar ZZ, Wierenga CE. The Utility of Cerebral Blood Flow as a Biomarker of Preclinical Alzheimer's Disease. Cell Mol Neurobiol. 2016 Mar 22;36(2):167–79.

3. Alsop DC, Detre JA, Golay X, *et al.* Recommended implementation of arterial spin-labeled perfusion MRI for clinical applications: A consensus of the ISMRM perfusion study group and the European consortium for ASL in dementia. Magn Reson Med. 2015 Jan;73(1):102–16.

4. Williams DS, Detre JA, Leigh JS, *et al.* Magnetic resonance imaging of perfusion using spin inversion of arterial water. Proc Natl Acad Sci U S A. 1992 Jan 1;89(1):212–6.

5. Maier FC, Wehrl HF, Schmid AM, *et al.* Longitudinal PET-MRI reveals β-amyloid deposition and rCBF dynamics and connects vascular amyloidosis to quantitative loss of perfusion. Nat Med. 2014 Nov 10;20(12):1485–92.

6. Jonckers E, Delgado y Palacios R, Shah D, *et al.* Different anesthesia regimes modulate the functional connectivity outcome in mice. Magn Reson Med. 2014 Oct;72(4):1103–12.

7. Yoshida K, Mimura Y, Ishihara R, *et al.* Physiological effects of a habituation procedure for functional MRI in awake mice using a cryogenic radiofrequency probe. J Neurosci Methods. 2016 Dec 1;274:38–48.

8. Zuurbier CJ, Emons VM, Ince C. Hemodynamics of anesthetized ventilated mouse models: aspects of anesthetics, fluid support, and strain. Am J Physiol Heart Circ Physiol. 2002 Jun;282(6):H2099-105.

9. Petrinovic MM, Hankov G, Schroeter A, *et al.* A novel anesthesia regime enables neurofunctional studies and imaging genetics across mouse strains. Sci Rep. 2016 Apr 15;6(1):24523.

10. Hohlbaum K, Bert B, Dietze S, *et al.* Severity classification of repeated isoflurane anesthesia in C57BL/6JRj mice-Assessing the degree of distress. Xie Z, editor. PLoS One. 2017 Jun 15;12(6):e0179588.

11. Matta BF, Heath KJ, Tipping K, *et al.* Direct cerebral vasodilatory effects of sevoflurane and isoflurane. Anesthesiology. 1999 Sep;91(3):677–80.

12. Eger EI. Isoflurane: a review. Anesthesiology. 1981 Nov;55(5):559–76.

13. Cesarovic N, Nicholls F, Rettich A, *et al.* Isoflurane and sevoflurane provide equally effective anaesthesia in laboratory mice. Lab Anim. 2010 Oct;44(4):329–36.

14. Nair G, Duong TQ. Echo-planar BOLD fMRI of mice on a narrow-bore 9.4 T magnet. Magn Reson Med. 2004 Aug;52(2):430–4.

15. Bukhari Q, Schroeter A, Rudin M. Increasing isoflurane dose reduces homotopic correlation and functional segregation of brain networks in mice as revealed by resting-state fMRI. Sci Rep. 2018 Jul 12;8(1):10591.

16. Grandjean J, Schroeter A, Batata I, *et al.* Optimization of anesthesia protocol for resting-state fMRI in mice based on differential effects of anesthetics on functional connectivity patterns. Neuroimage. 2014 Nov 15;102 Pt 2:838–47.

17. Schroeter A, Schlegel F, Seuwen A, *et al.* Specificity of stimulus-evoked fMRI responses in the mouse: the influence of systemic physiological changes associated with innocuous stimulation under four different anesthetics. Neuroimage. 2014 Jul 1;94:372–84.

18. Wells JA, Holmes HE, O'Callaghan JM, *et al.* Increased cerebral vascular reactivity in the tau expressing rTg4510 mouse: evidence against the role of tau pathology to impair vascular health in Alzheimer's disease. J Cereb Blood Flow Metab. 2015 Mar;35(3):359–62.

19. Kober F, Duhamel G, Callot V. Cerebral Perfusion MRI in Mice. In: Methods in molecular biology (Clifton, NJ). 2011. p. 117–38.

20. Tankersley CG, Fitzgerald RS, Kleeberger SR. Differential control of ventilation among inbred strains of mice. Am J Physiol. 1994 Nov;267(5 Pt 2):R1371-7.

21. Kilkenny C, Browne WJ, Cuthill IC, *et al.* Improving Bioscience Research Reporting: The ARRIVE Guidelines for Reporting Animal Research. PLoS Biol. 2010 Jun 29;8(6):e1000412.

22. Adamczak JM, Farr TD, Seehafer JU, *et al.* High field BOLD response to forepaw stimulation in the mouse. Neuroimage. 2010 Jun;51(2):704–12.

23. Stout RW, Cho DY, Gaunt SD, *et al.* Transcutaneous blood gas monitoring in the rat. Comp Med. 2001 Dec;51(6):524–33.

24. Hirschler L, Debacker CS, Voiron J, *et al.* Interpulse phase corrections for unbalanced pseudo-continuous arterial spin labeling at high magnetic field. Magn Reson Med. 2018 Mar;79(3):1314–24.

25. Buxton RB, Frank LR, Wong EC, *et al.* A general kinetic model for quantitative perfusion imaging with arterial spin labeling. Magn Reson Med. 1998 Sep;40(3):383–96.

26. Herscovitch P, Raichle ME. What is the correct value for the brain--blood partition coefficient for water? J Cereb Blood Flow Metab. 1985;5(1):65–9.

27. Dobre MC, Uğurbil K, Marjanska M. Determination of blood longitudinal relaxation time (T1) at high magnetic field strengths. Magn Reson Imaging. 2007;25:733–5.

28. Denis de Senneville B, Zachiu C, Ries M, *et al.* EVolution: an edge-based variational method for non-rigid multi-modal image registration. Phys Med Biol. 2016 Oct 21;61(20):7377–96.

29. Chen X, Gilkeson RC, Fei B. Automatic 3D-to-2D registration for CT and dual-energy digital radiography for calcification detection. Med Phys. 2007 Nov 28;34(12):4934–43.

30. Pan W, Hua X, Wang Y, *et al.* Dose response of dexmedetomidine-induced resistance to hypoxia in mice. Mol Med Rep. 2016 Oct;14(4):3237–42.

31. Zuurbier CJ, Koeman A, Houten SM, *et al.* Optimizing anesthetic regimen for surgery in mice through minimization of hemodynamic, metabolic, and inflammatory perturbations. Exp Biol Med (Maywood). 2014 Jun 25;239(6):737–46.

32. Zeller A, Arras M, Lazaris A, *et al.* Distinct molecular targets for the central respiratory and cardiac actions of the general anesthetics etomidate and propofol. FASEB J. 2005 Oct;19(12):1677–9.

33. Crawford MW, Lerman J, Saldivia V, *et al.* Hemodynamic and organ blood flow responses to halothane and sevoflurane anesthesia during spontaneous ventilation. Anesth Analg. 1992 Dec;75(6):1000–6.

34. Maggi CA, Meli A. Suitability of urethane anesthesia for physiopharmacological investigations in various systems. Part 2: Cardiovascular system. Experientia. 1986 Mar 15;42(3):292–7.

35. Wang Z, Schuler B, Vogel O, *et al.* What is the optimal anesthetic protocol for measurements of cerebral autoregulation in spontaneously breathing mice? Exp brain Res. 2010 Dec;207(3–4):249–58.

36. Gooding JM, Weng JT, Smith RA, *et al.* Cardiovascular and pulmonary responses following etomidate induction of anesthesia in patients with demonstrated cardiac disease. Anesth Analg. 58(1):40–1.

37. Morton DB, Jennings M, Buckwell A, *et al.* Refining procedures for the administration of substances. Lab Anim. 2001 Jan 24;35(1):1–41.

38. Shim H-J, Jung WB, Schlegel F, *et al.* Mouse fMRI under ketamine and xylazine anesthesia: Robust contralateral somatosensory cortex activation in response to forepaw stimulation. Neuroimage. 2018 Aug 15;177:30–44.

39. Hirschler L, Munting LP, Khmelinskii A, *et al.* Transit time mapping in the mouse brain using

time-encoded pCASL. NMR Biomed. 2018 Feb;31(2):e3855.

40. Tong X-K, Lecrux C, Hamel E, *et al.* Age-Dependent Rescue by Simvastatin of Alzheimer's Disease Cerebrovascular and Memory Deficits. J Neurosci. 2012 Apr 4;32(14):4705–15.

41. Matsuura T, Fujita H, Kashikura K, *et al.* Modulation of evoked cerebral blood flow under excessive blood supply and hyperoxic conditions. Jpn J Physiol. 2000 Feb;50(1):115–23.

3

SUPPLEMENTARY TABLES

Supplementary table 1. Anesthesia protocols used in this study. Animal numbers and age apply to C57BL/6J only.

Anesthesia	Isoflurane induction	Maintenance	Mixture air:oxygen	Number of animals	Age in months - mean (stdev)
Standard isoflurane	3.5 %	1.5 – 2.0 %	3:1	3	8.6 (3.7)
Low-dose isoflurane	2.0 %	1.25 %	Pure air	12	6.5 (4.0)
Standard isoflurane + ventilation	3.5 %	1.75 %	3:1	5	9.2 (3.3)
Medetomidine s.c.	3.5 %	0.15 mg/kg bolus; 0.30 mg/kg/h infusion	3:1	8	20.9 (0.5)

Supplementary table 2. Summary of absolute CBF values before and during CO_2 challenge.

Anesthesia protocol		Baseline CBF (mL/100 g/min)		CBF during CO_2 challenge (mL/100 g/min)		CVR (%)		Time to half peak (sec)	
		Median	IQR	Median	IQR	Median	IQR	Median	IQR
Standard isoflurane	Cortex	173.1	57.8	183.0	45.3	5.7	9.5	31.5	5.3
	Full Brain	157.7	32.9	161.3	30.2	2.3	2.1	38.5	5.3
Medetomidine	Cortex	113.9	41.3	160.1	25.4	36.5	30.6	45.5	59.5
	Full Brain	91.7	29.3	136.4	28.8	42.3	31.4	45.5	22.8
Low isoflurane	Cortex	143.0	38.3	164.1	28.1	12.7	9.3	31.5	7.0
	Full Brain	138.9	26.5	151.5	24.5	10.0	7.1	31.5	7.0
Standard isoflurane + ventilation	Cortex	136.1	14.2	157.1	14.5	12.2	23.5	24.5	12.3
	Full Brain	131.7	10.0	141.8	7.8	9.6	15.1	24.5	24.5

Supplementary table 3. Pros and cons of the anesthesia protocols tested.

	Pros	Cons
Standard isoflurane	- Easiest protocol - Short imaging session	- No CVR experiment possible - Respiratory depression
Medetomidine	- High CVR measurable	- Not suitable for every mouse strain - Longer preparation time (injection line, injection minipump) - Narrow time window for CVR measurements; measuring too early results in an unstable baseline; too late and the mouse is awake - Cardiac depression
Low isoflurane	- Accessible protocol for any user - CVR measurable	- Slightly longer induction time of anesthesia - Quick transfer to MRI animal bed after induction needed
Standard isoflurane + mechanical ventilation	- Stable physiology - CVR measurable	- Technical skills required for the intubation procedure - Dedicated equipment needed (ventilation pump) - Longer preparation time (intubation procedure)

3

SUPPLEMENTARY FIGURES
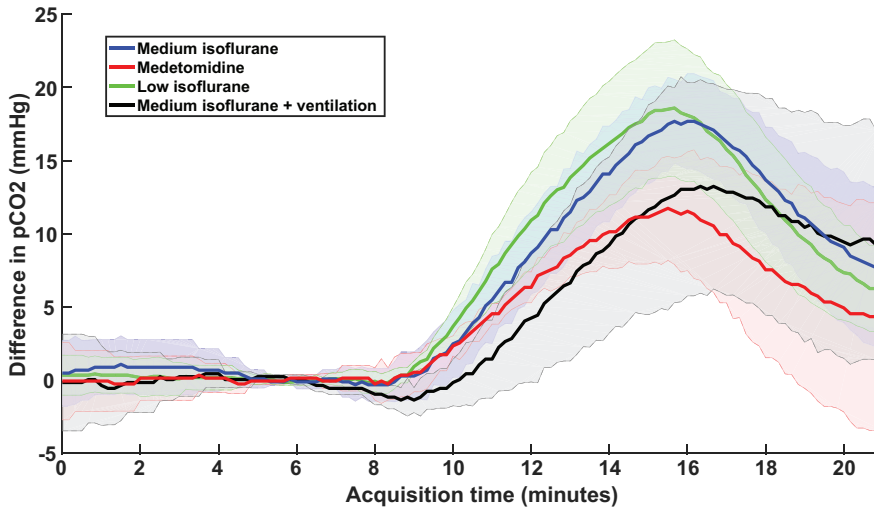
Supplementary figure 1. *The transcutaneous pCO_2 profiles measured during the pCASL scans in the C57BL/6J mice. The profiles are grouped per anesthesia protocol (mean ± SD). No significant differences were found between the groups. Note that the it takes around 2 minutes before the arterial CO_2 has diffused to the skin (CO_2 was administered from minute 7-14). Also note that 7 out of the 8 medetomidine profiles have not been captured due to a technical error, explaining the absence of the SD line in that group.*
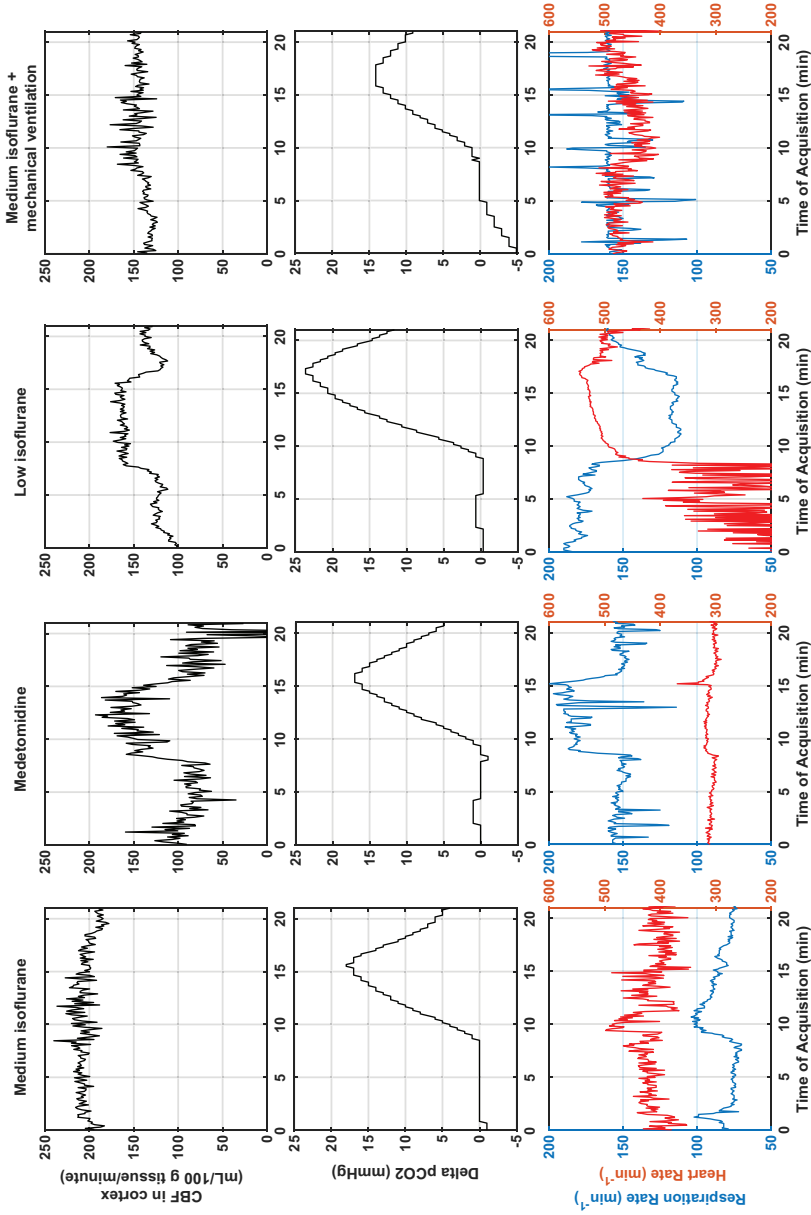
Supplementary figure 2. *Examples of physiological time-profiles. Note the lower heart rate in the medetomidine protocol compared to the others, and the incorrect sampling of the heart rate in the first half of the time-profile of the low isoflurane protocol. Also note the lower respiration rates in the high isoflurane protocol and the doubling of the measured respiration rate (ventilated at 80bpm) in the ventilation protocol, due to extra breaths/movements that the mouse exhibited in sync with the ventilation protocol (present in around half of the ventilated animals).*

4

Multi-scale assessment of brain blood volume and perfusion in the APP/PS1 mouse model of amyloidosis

Leon P Munting[1,2], Marc PP Derieppe[3], Lenard M Voortman[4], Artem Khmelinskii[5], Ernst Suidgeest[1], Lydiane Hirschler[1,6], Emmanuel L Barbier[6], Baudouin Denis de Senneville[7,8], Louise van der Weerd[1,2,*]

[1]Department of Radiology, Leiden University Medical Center, Leiden, the Netherlands.
[2]Department of Human Genetics, Leiden University Medical Center, Leiden, the Netherlands.
[3]Prinses Máxima Center for Pediatric Oncology, University Medical Center Utrecht, Utrecht, the Netherlands.
[4]Department of Cell and Chemical Biology, Leiden University Medical Center, Leiden, the Netherlands.
[5]Department of Radiation Oncology, Netherlands Cancer Institute, Amsterdam, the Netherlands.
[6]Univ. Grenoble Alpes, Inserm, U1216, Grenoble Institut des Neurosciences, Grenoble, France
[7]Department of Radiotherapy, University Medical Center Utrecht, Utrecht, the Netherlands.
[8]Institut de Mathématiques de Bordeaux, Université Bordeaux/CNRS UMR 5251/INRIA, Bordeaux-Sud-Ouest, France.

*Corresponding author. E-mail address: L.van_der_Weerd@lumc.nl;

(Submitted)

ABSTRACT

<u>Significance:</u> **Cerebrovascular dysfunction is increasingly recognized to play a role in the development of Alzheimer's disease (AD). However, the exact relation between cerebrovascular dysfunction and the for-AD characteristic neuropathological amyloid-β accumulation is still unclear and further studied in this work.**

<u>Aim:</u> **The effect of parenchymal amyloid-β plaques on the structure and function of the vasculature is investigated in the APP/PS1 mouse model of amyloidosis using 3D microscopy and perfusion MRI.**

<u>Approach:</u> **For structural imaging, blood vessels and amyloid-β plaques were fluorescently labeled** *in vivo* **with lectin-DyLight594 and methoxy-XO4, respectively, in 17 months old APP/PS1 and control mice. The brain tissue was cleared post-mortem with the CUBIC tissue clearing protocol, which allowed microscopic imaging of the vessels and plaques in a large 3D volume. Segmentation of the brain vasculature enabled quantification of the microvascular Cerebral Blood Volume (mCBV). For functional imaging,** *in vivo* **pseudo-Continuous Arterial Spin Labeling (pCASL)-MRI was used to measure Cerebral Blood Flow (CBF) and Arterial Transit Time (ATT) in 2 years old APP/PS1 and control mice.**

<u>Results:</u> **mCBV ranged from 2 % to 5 % in the white matter and the thalamus, respectively. No mCBV differences were observed between APP/PS1 mice and control mice. Neither were any differences observed in the MRI measures CBF or ATT.**

<u>Conclusions:</u> **Our results indicate that structure and function of brain vasculature are not profoundly affected by the presence of amyloid-β plaques, at least not in mice.**

INTRODUCTION

Familial mutations in genes related to the production of the amyloid-β peptide are associated with early cognitive decline and extensive accumulation of amyloid-β pathology in the brain. These mutations lead to Alzheimer's disease (AD) with full penetrance.[1] This is a clear indication that amyloid-β plays an important role in the development of AD, at least in familial cases with early onset. The importance of its role in the development of sporadic AD, however, is continuously debated. Researchers who are sceptic about the amyloid hypothesis, point out that amyloid-β plaque load correlates poorly with cognitive decline and that plaques are also found in the healthy elderly.[2] Alternative, or synergistic, pathogenic mechanisms for AD are receiving more and more attention in the recent years, among which is the cerebral circulation. Various imaging studies have demonstrated that changes in brain perfusion,[3] blood volume[4,5] and cerebrovascular reactivity[6] are associated with AD. In a predictive model based on human imaging data, cerebrovascular dysfunction has been estimated to be present early on in the AD onset.[7] AD and cardiovascular disease share genetic risk factors[8] and histological studies have shown that cerebrovascular pathology such as microinfarcts and atherosclerotic arteries is commonly found in AD, more often than in other neurodegenerative diseases.[9] Given the lack of evidence to hold either amyloid-β or the vasculature fully responsible for the development of sporadic AD, it seems likely that it is a multi-factorial disease in which amyloid-β, cerebrovascular dysfunction and possibly other factors all play a part. Insight into the extent of their roles as well as how amyloid-β and cerebrovascular dysfunction influence each other is important to better understand the mechanisms of the disease and for the development of therapeutic strategies. However, studying this relation in patients is complicated due to a number of reasons. Firstly, although PET and MRI imaging techniques exist to directly visualize amyloid-β burden and perfusion *in vivo* in patients,[1,3] these imaging techniques are not offering sufficient spatial resolution to directly link amyloid-β distribution and the microvasculature. Thus, these cellular relations can only be characterized end-stage after autopsy. Secondly, the intricate 3D structure of the microvasculature complicates its characterization even *ex vivo*, as conventional histology does not allow volumetric imaging. Lastly, amyloid-β can be present in different forms, including parenchymal amyloid-β plaques, cerebrovascular amyloid-β and amyloid-β oligomers. The latter are soluble, neurotoxic forms of amyloid-β aggregates which in the recent years have been shown to correlate better with cognitive decline than parenchymal amyloid-β plaques.[10] Cerebrovascular amyloid-β is commonly referred to as cerebral amyloid angiopathy (CAA), which has been estimated to co-occur in around 78 % to 98 % of the AD cases.[11] A deeper understanding of the pathophysiology implies that the interplay of each structure, *i.e.*, amyloid-β oligomers, cerebrovascular and parenchymal amyloid-β, with the brain vasculature is better understood.

Mouse models can be a useful tool to study the relation between cerebrovascular dysfunction and amyloid-β, as tissue can be collected for histology at any age and disease stage following *in vivo* imaging in order to relate imaging outcomes with molecular or microstructural phenotypes. Furthermore, the possibility to specifically engineer the genome of a mouse has enabled the creation of models that reflect separate disease components. By introducing different types of familial AD mutations, models have been created that develop either mainly parenchymal plaques,[12,13] arteriolar CAA,[14] capillary CAA[15] or oligomers.[16] Here, we exploited this benefit of mouse models and studied whether the presence of parenchymal amyloid-β plaques influences the morphology or function of the brain vasculature. Specifically, we studied the microvascular cerebral blood volume (mCBV), the cerebral blood flow (CBF) and the arterial transit time (ATT) in the APP^{swe}/ $PS1^{dE9}$ amyloidosis model[12] at old age and thus with high parenchymal plaque burden. To measure the mCBV, the vasculature was imaged post-mortem in 3D with laser scanning microscopy after the brain tissue was made transparent with CUBIC (clear, unobstructed brain imaging cocktails and computational analysis).[17] CBF and ATT were measured *in vivo* with pseudo-Continuous Arterial Spin Labeling (pCASL)-MRI. Our findings indicate that the structure and function of the mouse cerebral circulation are not substantially disturbed by the presence of parenchymal amyloid-β plaques.

MATERIALS AND METHODS

Animals

This study was carried out in compliance with the European Directive 2010/63/EU on the protection of animals used for scientific purposes and reported in compliance with the ARRIVE guidelines.[18] The experiments were approved by the institution for animal welfare of the Leiden University Medical Center in the Netherlands and performed under DEC12065. The background strain of all mice in the study was the F2 generation of a cross between C57Bl/6J and C3H/HeJ mice. An optical imaging study and an MRI study were performed with two separate groups of mice bred in-house. The founder mice were acquired at the Jackson Laboratory (Bar Harbor, ME, USA). For optical imaging, 5 APP^{swe}/ $PS1^{dE9}$ (APP/PS1)[12] transgenic (TG) mice (17 ± 2 months old; 2 female) and 5 wild type (WT) controls (18 ± 2 months old; 3 female) were used. In the MRI study, 6 APP/PS1 mice (24 ± 1 month old; 6 females) and 6 WT controls (26 ± 1 month old; 4 females) were used. The mice were housed together (2–4 per cage) and had access to chow food and water *ad libitum*. The cages were individually ventilated and were provided with bedding material and cage enrichment, with a 12 h day/night cycle.

Microscopy

Brain isolation and tissue processing—Twenty-four hours ante-mortem, the 5 APP/PS1 and 5 WT mice were i.p. injected with 10 mg/kg methoxy-XO4 (in-house synthesized, 0.05 M dissolved in 1:1 DMSO:Cremophor and diluted in PBS to a total volume of 150 µL), a small fluorescent molecule that binds to beta-sheets and thereby enables visualization of Aβ deposits. The next day, 5 minutes ante-mortem, the mice were i.v. injected with 200 µL of 1 mg/mL DyLight 594-labeled tomato lectin (Vector Labs, CA, USA), which binds to the endothelium and thereby enables visualization of the vasculature. Subsequently, the mice were injected with an i.p. overdose of Euthasol (AST Pharma), followed by opening of the chest for intra-cardiac perfusion with 20 mL of ice-cold PBS and 20 mL of ice-cold 4 % PFA. The brains were then isolated and fixated further in 4 % PFA. Thereafter, the brain was cut in two hemispheres. The left hemisphere was made transparent for imaging, the right hemisphere was stored overnight in 30 % sucrose in PBS, snap-frozen in 2-methylbutane and stored at -80 °C for later studies. To make it transparent, the left hemisphere was treated with the CUBIC clearing protocol, which is described in.[19] In short, the hemisphere was washed 2 times for 1 hour in PBS at room temperature (RT) to wash away the PFA, transferred to a 1:1 mix of PBS and CUBIC solution 1 (25 % urea, 25 % quadrol [N,N,N',N'-Tetrakis(2-hydroxypropyl)ethylenediamine, Sigma-Adrich] and 15 % triton weight/weight in MiliQ) and incubated with gentle shaking for 6 hours at 37 °C. Thereafter, the 1:1 mix was replaced with pure CUBIC solution 1 and incubated for 8 days at 37 °C with gentle shaking. During this time, the solution was replaced every 2 days. Afterwards, the CUBIC solution 1 was washed away with 6 PBS washes over the course of 6 hours and the brain tissue was then incubated overnight at RT with a 1:1 mix of PBS and CUBIC solution 2 (50 % sucrose, 25 % urea and 10 % TEA [Triethylamine, Sigma-Aldrich] weight/weight in MiliQ). The next morning, the mix of PBS and solution 2 was replaced with pure CUBIC solution 2, and further incubated for 2 days with gentle shaking at 37 °C. The solution was refreshed once after 1 day. The result of the clearing procedure in terms of tissue transparency is illustrated in figure 1.
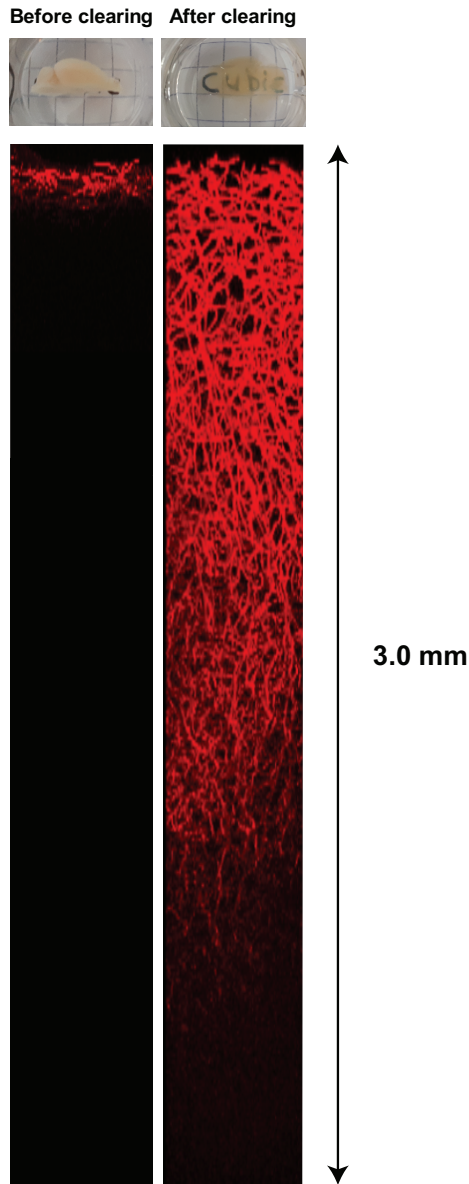
Before clearing   After clearing

3.0 mm

Figure 1: Effect of CUBIC clearing on tissue transparency and penetration depth with imaging. On the top left, a hemisphere is shown before clearing; on the top right the same hemisphere after clearing. On the bottom left, an orthogonal view from a representative Z-stack is shown, acquired in an uncleared hemisphere. On the bottom right, an orthogonal view from a representative Z-stack acquired in a cleared hemisphere, with similar acquisition parameters. Note the increase in penetration depth when imaging cleared tissue. The Z-stacks were acquired at the level of the thalamus, in sagittal orientation, without laser power compensation over imaging depth.

Image acquisition—The hemisphere was imaged in sagittal orientation in a 1:1 mix of
silicone oil (Sigma, product number 175633) and mineral oil (Sigma, product number
M8410) with a Zeiss LSM 710 NLO laser scanning microscope. A Zeiss 20x Clr Plan-
Apochromat objective (NA = 1.0; WD = 5.6 mm; Corr nd = 1,38) and a motorized stage
were used, allowing imaging deep into the tissue together with full-brain coverage in
the XY-direction. The methoxy-XO4 and DyLight594 were simultaneously excited with a
multiphoton Ti:Sapphire laser (Mai Tai, Spectra Physics) at 800 nm and their emission
was filtered and detected with a Zeiss non-descanned Binary GaAsP PMT detector (BiG.2)
equipped with two filters (green 500–550 nm and red 570–610 nm). Even though the
hardware of the microscope allowed imaging with sub-micrometer axial resolution, the
axial resolution was limited to 3.32 µm, with a 9.96 µm step size. This was done to find a
trade-off between data quality on the one hand and acquisition time and file size on the
other hand, which were around 2.5 days and 10 GB per sample, respectively.

Image processing—The resulting Z-stacks were flat-field corrected using a custom macro in
ImageJ and stitched with the Grid/Collection plug-in[20] in ImageJ, using the stage coordinates
as initialization. Stage coordinates were extracted from the metadata of the Zeiss (.czi)
file using a custom Python script. Methoxy-XO4 has a very wide emission spectrum,
therefore amyloid plaques were visible in both the green and red channel (data not shown).
DyLight-594 has a narrow emission spectrum and was thus visible in the red channel only.
To remove the methoxy-XO4 fluorescence from the red channel, the green channel was
first subtracted from the red channel, also for the WT mice for the sake of comparability.
Vessel segmentation was performed with the subtracted data using an Otsu threshold. One
mouse (male, WT) had to be excluded from further analysis, due to wrong segmentation,
which was the result of a low SNR in the raw data, probably a result of inadequate i.v. lectin
injection. After segmentation, the blood volume in the brain was mapped using patches
of 15 x 15 x 5 voxels in which the volume percentage of vessel-segmented voxels was
determined, resulting in mCBV maps with 50 µm³ isotropic resolution. To retrieve Atlas-
based regions of interest (ROIs), the stitched and shading-corrected data (red channel only,
before subtraction) was downsampled to 50 µm³ isotropic resolution and registered to
the Allen Brain template using EVolution, an edge-based variational non-rigid multi-modal
image registration method.[21] Six different ROIs were chosen from the Allen Brain template
and propagated to the blood volume maps of each individual mouse. This process was
verified and adjusted if needed by a user (LPM). If a large vessel was present in a brain
region, this resulted in patches with a high blood volume (> 15 %, see red arrow in
figure 2). To avoid such macro-vascular contribution to the regional blood volume values,
only voxels with values below 15 % of blood volume were included in the analysis. The
impossibility to place the brain tissue exactly orthogonal below the microscope objective
resulted in oblique optical sectioning (supplementary figure 1). Also, decreasing signal

intensity values were observed when deeper parts of tissue were imaged, even though the brain tissue was CUBIC cleared (figure 1). This resulted in decreasing mCBV values over imaging depth. Together with the oblique optical sectioning, this led to mCBV maps with an axial gradient due to differing quantities of tissue present above different tissue regions in one slice (supplementary figure 1). Alignment of the tissue in the Z-direction with a custom MATLAB script removed this axial gradient, but maintained the gradient in the Z-direction, starting after around 10 slices/500 μm (supplementary figure 2). The analysis was therefore restricted to the upper 500 μm of tissue.

MRI

The 6 APP/PS1 and 6 WT control mice were scanned with a Bruker 7 T PharmaScan (Ettlingen, Germany) and a 23 mm volume coil, using the same protocol as described in.[22] The 6 WT mice were the same as used in.[22] In short, the following protocol was used:

Animal preparation—the mice were anesthetized with 3.5 % isoflurane (Pharmachemie BV, Haarlem, Netherlands) for induction and 1.5-2.0 % for maintenance in a 1:1 mix of air and oxygen, to keep breathing rates around 100 bpm. The temperature was kept at 37 °C with a feedback-controlled waterbed (Medres, Cologne, Germany).

Image acquisition—Anatomical T_2-weighted (T_2W) images were first acquired in all three orientations with a standard Bruker T_2RARE sequence for planning the ASL sequences and for registration purposes. Thereafter, the pCASL interpulse phase-increase was optimized with pre-scans, as described before.[23] Then, two pCASL sequences were acquired, one optimized for measuring CBF (standard pCASL), the other for measuring ATT (time-encoded pCASL [te-pCASL]). The standard pCASL consisted of 60 pairs of label and control scans with a labeling duration of 3000 ms, a constant post-labeling delay (PLD) of 300 ms and a total scan time of 7 minutes. The te-pCASL consisted of a 45 times averaged Hadamard12-encoded labeling block with a sub-bolus labeling duration of 50 ms and 11 effective PLDs (30 ms till 530 ms with 50 ms spacing per PLD) and a total scan time of 7 minutes. Both pCASL scans were followed by a 3-slice coronal spin echo EPI readout with identical parameters (17 ms echo time, 0.224 × 0.224 mm² in-plane resolution, 1.5 mm slice thickness and a 1 mm slice gap). To aid quantification, an inversion-recovery scan and a flow-compensated, pCASL-encoded FLASH sequence were additionally acquired for every mouse to measure the tissue T_1 and the labeling efficiency, respectively. One mouse (TG, female) had to be excluded from further analysis, as it died during the scan, probably a result of fragility due to old age.

Image processing—The individual EPIs from both ASL sequences were first aligned to the first EPI of the standard pCASL scan to compensate for motion during the scans. Six different ROIs (auditory/visual cortex, sensory cortex, motor cortex, hippocampus,

thalamus and striatum) were manually drawn on the anatomical images of one arbitrarily chosen mouse (reference dataset), and propagated to the anatomical images of the other animals after registration to the reference dataset. The anatomical images, T_1 maps and te-pCASL scans of all mice were registered to the first EPI of their standard pCASL scan, allowing the propagation of the ROIs to all MRI sequences. All steps were performed in a coarse-to-fine manner using the Elastix image registration toolbox[24] and verified by two independent observers. Buxton's kinetic perfusion model[25] was used to calculate the CBF and ATT. The CBF was derived from the averaged signal difference between the label and control (ΔM) scans from the standard pCASL sequence. The ATT was retrieved after fitting the 11 effective PLDs from the te-pCASL sequence to the perfusion model.

Statistics

For both the microscopy and the MRI data, a mixed ANOVA was used to test whether there was a significant effect of either the genotype or the brain region on the outcome measures mCBV, CBF and ATT. Because Mauchly's test of sphericity was significant in the CBF data, the degrees of freedom for the F-distribution were Greenhouse-Geisser corrected. For ATT and mCBV data, Mauchly's test was not significant, thus sphericity was assumed for the degrees of freedom of the F-distribution. Statistical testing was done using IBM SPSS statistics 23 software (Armonk, New York, NY, USA).

RESULTS

mCBV mapping

A clear improvement in tissue transparency and imaging depth was seen after brain tissue was treated with CUBIC (figure 1). Representative WT and TG examples of cerebrovascular and amyloid-β plaque labeling are shown in the left column in figure 2, confirming that plaques are present in TG mice only. In the vicinity of these plaques, no noticeable morphological changes could be observed in the capillary bed at the spatial resolution set, see vessels indicated with arrowheads in 2d and additional examples in supplementary figure 3. For the quantitative analysis of the mCBV in the volume of hemisphere imaged, the cerebrovascular signal was first segmented with the application of an Otsu threshold (middle column in figure 2). Thereafter, the density of positively segmented voxels was mapped in patches of 50 μm³ isotropic resolution (right column in figure 2). This enabled comparison of blood volumes between WT and TG mice. In figure 3, the first slice of the aligned mCBV maps of all the mice in the study are shown. mCBV estimates were retrieved from 6 different brain regions after registration to the Allen Brain atlas and ranged between 2-5 % (figure 4). No significant difference in mCBV was found between the APP/PS1 and the WT ($F[1,7] = 166$; $p = 0.40$), but there was a significant effect of brain region on mCBV ($F[5,35] = 43.2$; $p < 0.001$), with the highest blood volume in the thalamus (4.9 % average in WT), and the lowest in the white matter (2.0 % average in WT).
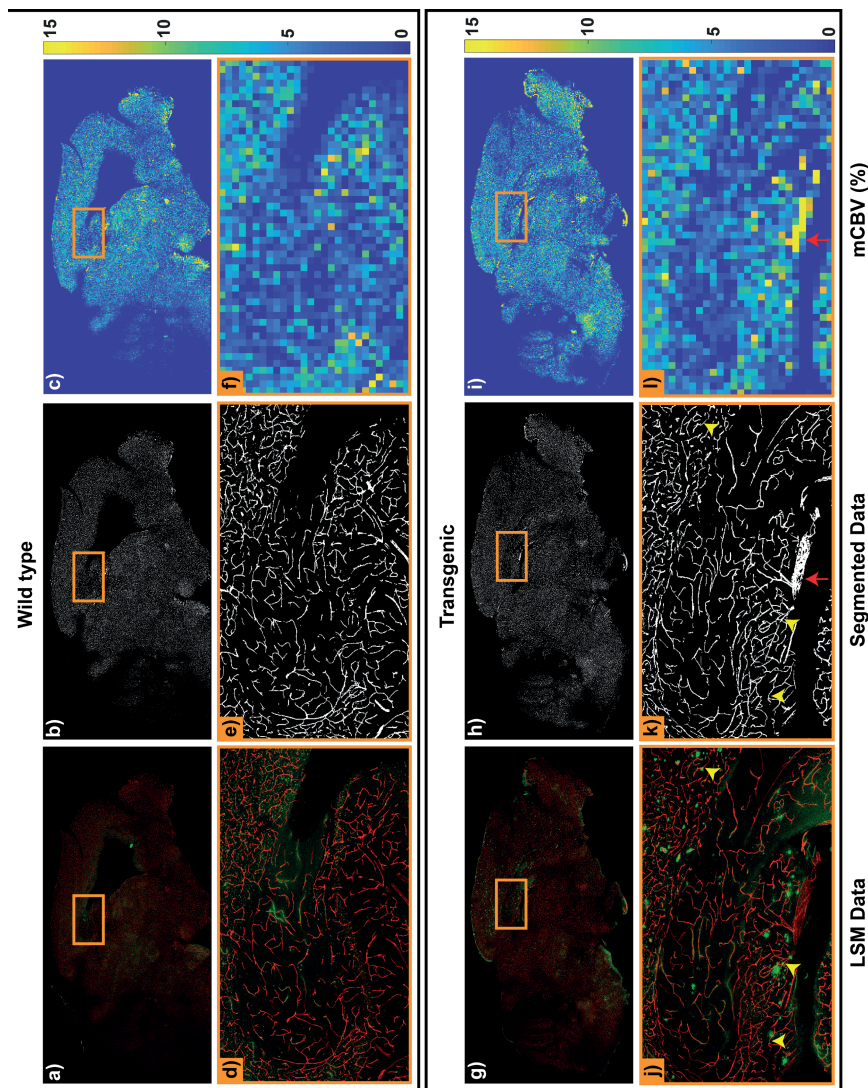
Figure 2: Example of the segmentation and microvascular Cerebral Blood Volume (mCBV) calculation process. A wild type (WT) example is depicted in the upper two rows (a-f), an APP/PS1 transgenic example in the lower two rows (g-l). The images on the second (d-f) and fourth (j-l) rows correspond to the orange squares in the images on the first and third rows. In the images in the left column (a,d,g,j), maximum intensity projections of 5 raw data slices are shown. In the middle column, the result of the Otsu segmentation and on the right column, the resulting mCBV maps. The yellow arrowheads in (j) and (k) point to vessels that are in the close vicinity to plaques, but seem unaffected by them. The red arrow in (k) and (l) points to a large vessel, which results in very high values in mCBV map.
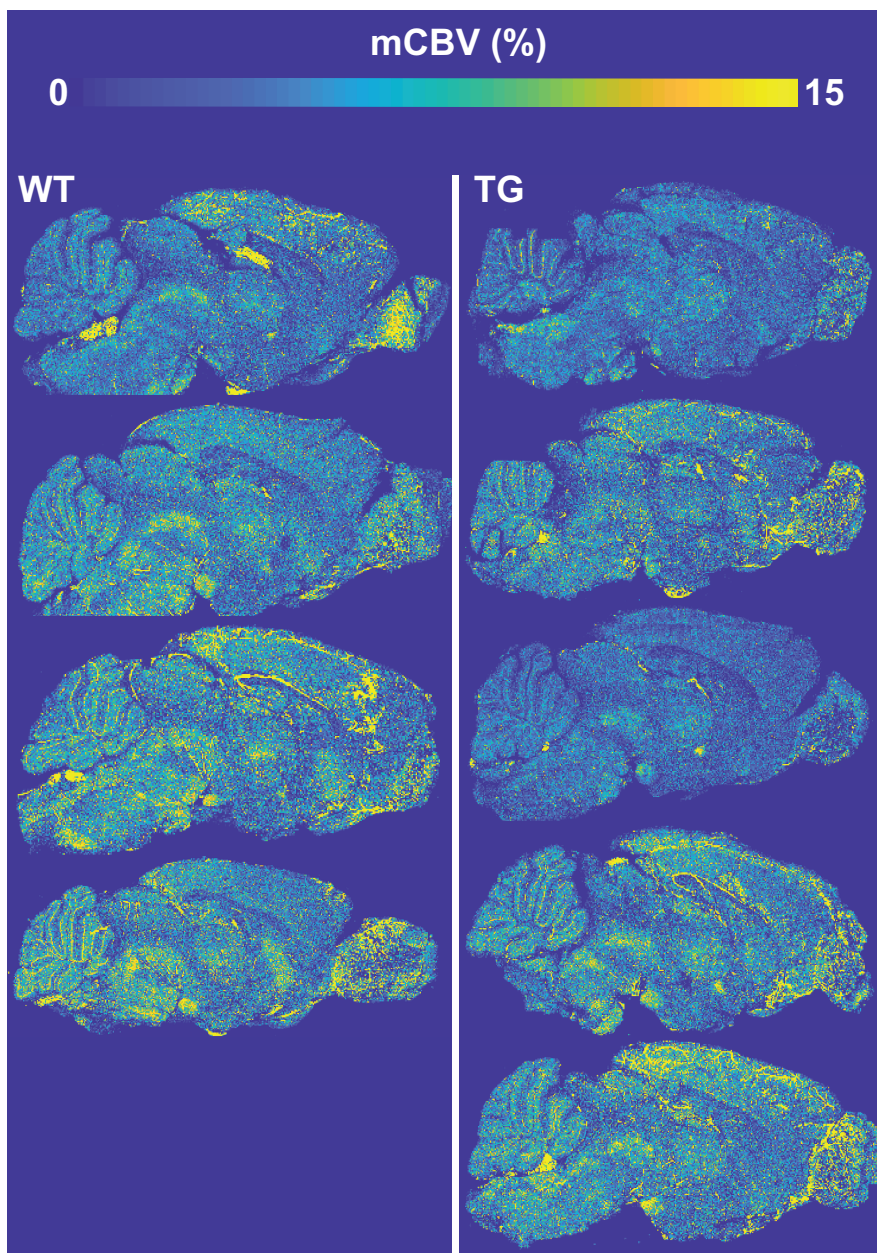
Figure 3: *Microvascular Cerebral Blood Volume (mCBV) maps of all mice in the study. The left column represents wild type (WT) mice, the right column transgenic (TG). All maps represent the most superficial mCBV map with respect to the microscope objective.*
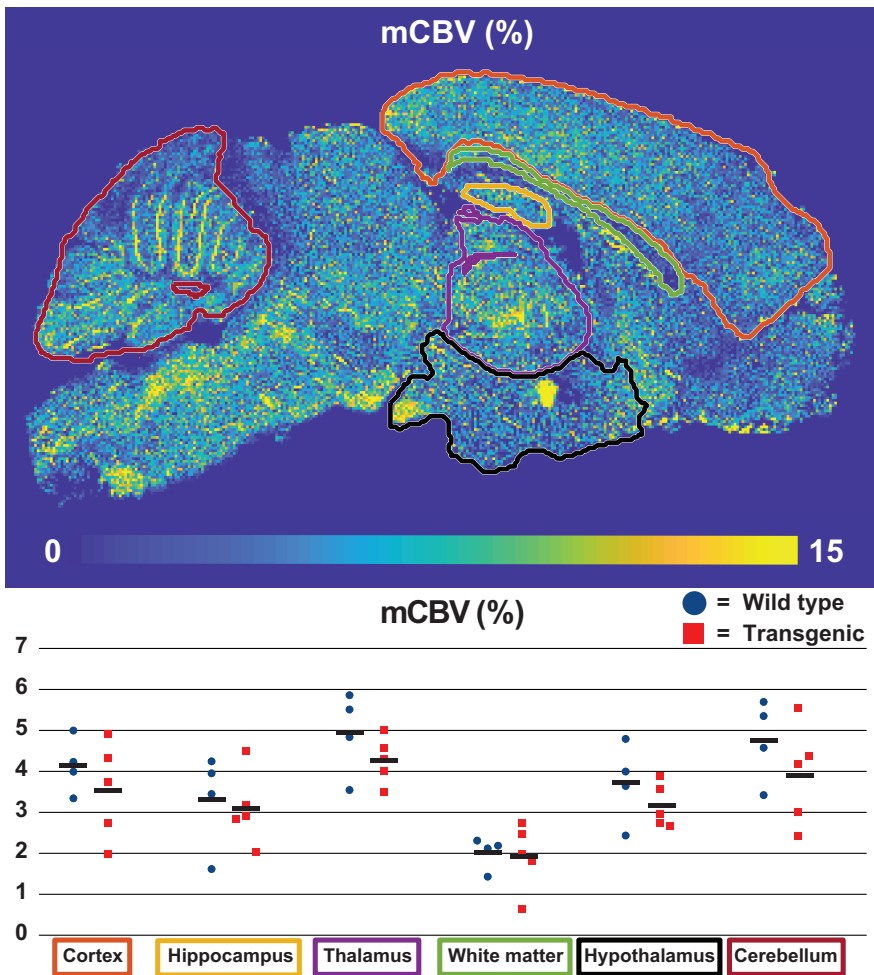
Figure 4: *Microvascular Cerebral Blood Volume (mCBV) quantification. mCBV is quantified in 6 brain regions and full brain. Circles (WT) and squares (TG) represent individual mice, stripes represent group averages.*

CBF and ATT mapping

Characteristic CBF maps for both WT and TG mice are shown in figure 5a. The CBF was compared between WT and TG mice in the 6 different brain regions as displayed on an anatomical T_2W image in figure 5b. Representative ATT maps for both genotypes are shown in figure 6a. ATT was also compared between WT and TG mice in the same brain regions. No differences were observed in either CBF or ATT between the APP/PS1 mice

and the WT mice (F[1,9] = 2.06; p = 0.19 & F[1,9] = 0.056; p = 0.82 respectively). Similar
as in the mCBV data, there was a significant effect of brain region on both CBF and ATT
(F[1.70,15.0] = 4.62; p = 0.031 & F[5,45] = 84.2; p < 0.001 respectively).

DISCUSSION

Alzheimer's disease is characterized by the presence of neuropathological amyloid-β
accumulations and is associated with cerebrovascular dysfunction.[2,7] The exact contributions
of both on AD onset and their interplay are currently not well known and are difficult
to study in humans. Mouse models of disease can provide valuable information, as
microstructural tissue characterization with histology can be performed following *in
vivo* imaging. Also, the many different mouse models reflecting different characteristics
of AD allow studying the relation between different aspects of the disease. Here, we
performed *in vivo* MR imaging and post-mortem microscopy in a large 3D volume in the
APP/PS1 amyloidosis model, which develops extensive amyloid-β plaque accumulation
in the brain parenchyma and to a lesser extent CAA on the leptomeningeal arteries.[26]
The CUBIC clearing protocol together with the implemented image processing pipeline
allowed characterizing amyloid-β plaques and the microvasculature in 3D, including the
quantification of the microvascular blood volume in a brain slab of 0.5 mm and direct
observation of the effect of plaques on the vasculature. *In vivo*, the perfusion parameters
CBF and ATT were measured using ASL-MRI. Given the many connections that have been
made between amyloid-β and cerebrovascular dysfunction, it seems remarkable that in
this study, no cerebrovascular dysfunction was observed using two imaging modalities
in aged APP/PS1 mice with high amyloid burden.

In contrast to our finding, a reduction in CBV has been reported in AD patients compared
to non-demented elderly controls.[4,5] A direct capillary loss might underlie this reduction,
which has indeed been reported in some but not all [30] histology studies based on
human AD brain tissue. Another possible underlying cause of decreased CBV is capillary
constriction. Recently, amyloid-β oligomers have indeed been shown to constrict capillaries
in live human brain tissue, and localized capillary constriction was also observed in post-
mortem fixed AD brain slices [31]. Changes in CBF have been associated with AD as well.
A wealth of studies have shown this, where in the prodromal phase, CBF was shown to be
increased, and decreased when clinical symptoms are overt (for a review see [3]). Similar
capillary affliction as described above may underlie this decrease in CBF in cognitively
impaired AD patients, but arteriolar dysfunction may also play a role. Reasons for the
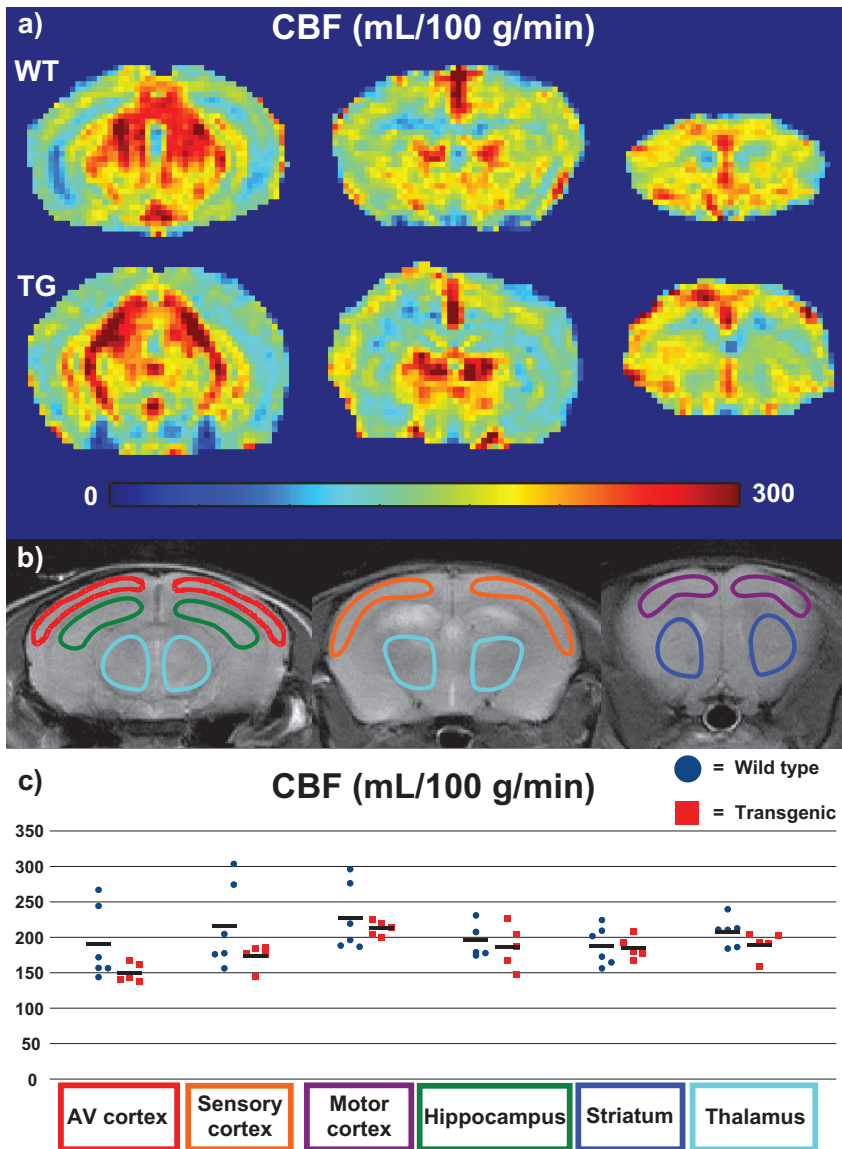latter could be arteriolar CAA and/or atherosclerosis.[9]

4

Figure 5: Cerebral blood flow (CBF) maps and CBF values from the MRI data. (a)—CBF maps (three slices) are shown from an average wild type (WT) mouse on the upper row and an average transgenic (TG) mouse on the second row. (b)—Spatially corresponding anatomical images are shown, with the ROIs indicated in which CBF was quantified. (c)—The resulting CBF values are shown in a graph, where circles (WT) and squares (TG) represent individual mice and stripes represent group averages. AV = auditory/visual.
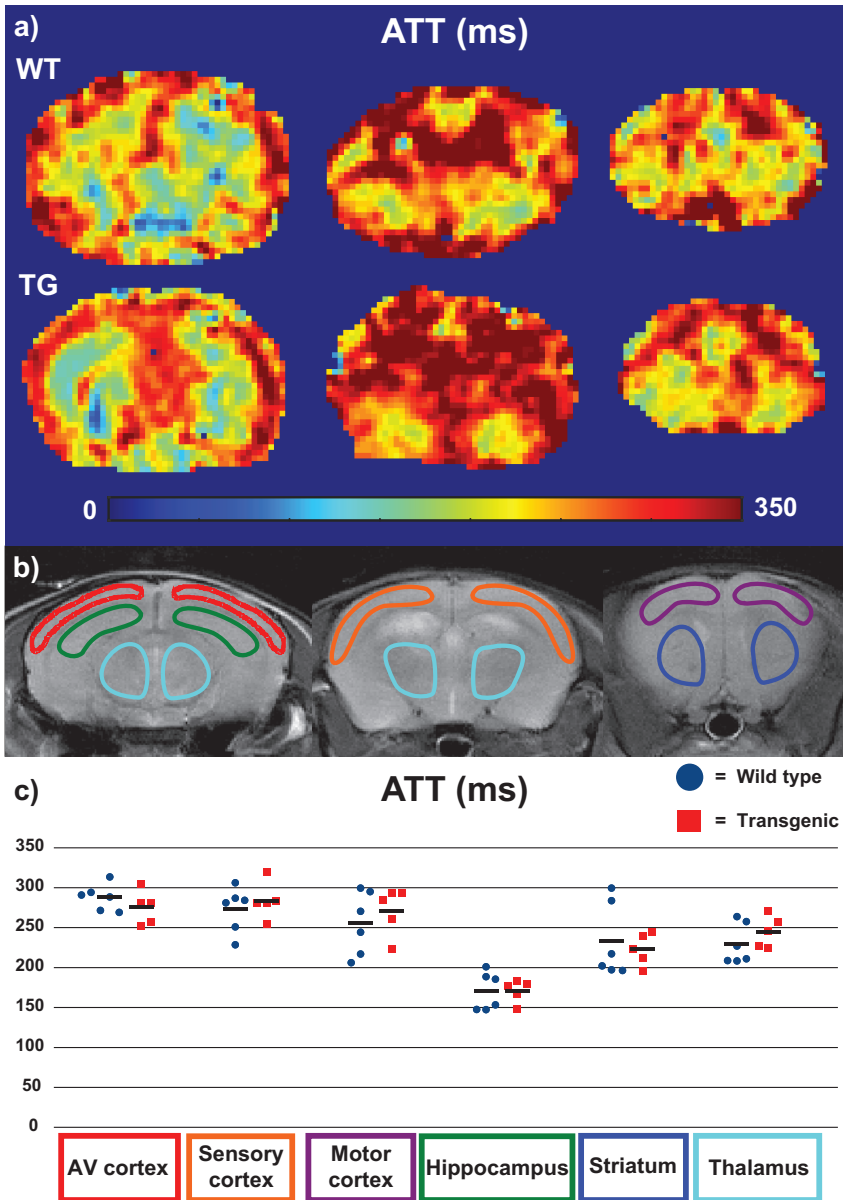
Figure 6: Arterial Transit Time (ATT) maps and ATT values from the MRI data. (a)—ATT maps (three slices) are shown from an average wild type (WT) mouse on the upper row and an average transgenic (TG) mouse on the second row. (b)—Spatially corresponding anatomical images are shown, with the ROIs in which ATT was quantified. (c)—The resulting ATT values are shown in a graph, where circles (WT) and squares (TG) represent individual mice and stripes represent group averages.

In mouse models of amyloidosis, it is ambiguous how CBV and CBF evolve. CBF has been shown to decrease,[32-38] not change[36,39,40] or transiently increase[41] when compared to age-matched WT mice. Studies with some models show reduced capillary density,[42,43] while studies with other models show preserved capillary density.[40,41,44] Regarding the diameter of the microvasculature, both capillary constriction[31] and capillary dilation[41] have been reported. An important flipside of the wide variety of models available is thereby illustrated: results obtained in one mouse model are not generalizable to other models, let alone to patients. On the other hand, the different models may help us understand the possible consequences of different types of amyloid-β accumulation. Interestingly, all studies that report no change or transiently increased CBF are performed with a model with a PS1 insertion.[36,39-41] The question then arises whether the PS1 insertion by some means protects the cerebral vasculature. Important features of models with an additional PS1 insertion are a shift in the amyloid-β-40:amyloid-β-42 ratio towards the more hydrophobic amyloid-β-42, as well as early and aggressive parenchymal plaque development.[45] An increase in hydrophobicity of the amyloid-β monomers has been hypothesized to lead to increased hydrophobicity of the oligomers, resulting in increased binding to cell membranes and increased neurotoxicity.[46] In the same way, it could be hypothesized that the increased hydrophobicity of oligomers reduces the movement of oligomers from the parenchyma to the vasculature, thereby decreasing the constrictive effects of amyloid-β on the vasculature. Indeed, in [36], where three amyloidosis models were directly compared, two models with CAA and without PS1 insertion showed a CBF decrease, and one without CAA and with PS1 insertion did not show a decrease in CBF.

There is much less data available on the relation between ATT and AD. One study in patients shows ATT is preserved in AD patients,[47] whereas another shows a regional ATT increase.[48] To the best of our knowledge, no pre-clinical studies exist with amyloidosis mouse models and ATT. But given the lack of differences in mCBV and CBF, it is not surprising that no differences were found in ATT.

From the brain regions analyzed, the mCBV values found were highest in the thalamus and lowest in the white matter, which is in agreement with other studies.[49-51] There was however a large inter-animal variation in absolute mCBV values. For example, the mCBV values in the thalamus were between 3 and 6 % in WT mice, which is unlikely due to biological variation only. Some of this high variation may be due to varying quantities of lectin that effectively arrived in the brains of the different mice after the 200 μL i.v. injection, thereby creating differences in vessel wall labeling efficiency between animals. Correcting for such differences is complicated, as it is difficult to disentangle vessel wall labeling efficiency differences from true blood volume differences. However, since amyloid-β pathology is present in certain brain regions only, blood volumes could be normalized to un-affected brain regions such as the hypothalamus or cerebellum. This did not change the outcome

however, as the APP/PS1 and WT mice still showed similar mCBV values after normalization to the hypothalamus or cerebellum (data not shown).

Despite the large volumes of tissue that were imaged, only a small number of biological replicates was used, which is the largest limitation of this study. The absence of significant differences between APP/PS1 mice and WT control mice suggests that parenchymal amyloid-β plaques have little or no effect on the structure and function of the cerebral vasculature, at least in mice. However, trends could be observed towards lower mCBV and cortical CBF in the APP/PS1 mice. If these were true, and not due to noise and/or natural variation, they could become significant with larger group sizes. The size of the trend towards lower cortical CBF in this study (10-20 %) is however not on par with the observed CBF decrease in the clinic (42 %).[52] Additionally, one important difference between this mouse model and AD patients is the lack of cerebral atrophy, despite the high amyloid burden. As atrophy is often hypothesized to contribute to cerebral hypoperfusion,[53] our observations do not discount this possibility.

Furthermore, the age- and gender distribution was not fully equal between the groups, where the WT group contained 1 more male and was 1 month older in the microscopy study, and 2 more males and 2 months older in the ASL-MRI study. Preferably, age and gender would have been completely equal. Indeed, gender is known to influence cerebrovascular factors such as stroke risk and outcome.[54,55] Furthermore, female mice have shown higher rates of amyloid-β accumulation.[56] However, baseline brain perfusion and blood volume have been reported to be similar in male and female mice,[55,57] and all transgenic mice showed advanced amyloid-β pathology, making it unlikely that our data was heavily biased by the gender difference. Also, brain perfusion has been shown to be stable in wild type adult mice,[22,36] reducing the likelihood of an age bias. Moreover, there was no trend observable in the data towards lower or higher mCBV, CBF or ATT with age or gender (not shown). Another limitation of this study is the relatively low resolution used, which might not be sufficient to detect small constrictions in capillary diameter, especially if these were to be focal constrictions. It should also be taken into account that red blood cells could be hindered by such focal constrictions, lowering the local hematocrit, but leaving the mCBV, CBF and ATT unchanged. Further research could include imaging small areas at higher resolution to be able to detect such small changes. Also, despite the 3 to 4 mm thickness of imaged tissue, only 0.5 mm was used for mCBV quantification, due to dropping SNR values with deeper tissue areas. Possibly, further optimization of the tissue clearing and/or imaging could improve the SNR in deeper tissue and thereby improve the mCBV mapping. In our hands however, changing the clearing method to a method that results in tissue with a lower refractive index (RI) (*e.g.* ScaleA[58] or PACT[59]) did not give better results, due to extensive tissue expansion (data not shown). The expansion strongly drives up image acquisition times, whereas effectively, similar sizes of tissue are imaged

when corrected for the expansion. Changing to a clearing method resulting in higher tissue RI such as 3DISCO[60] would be sub-optimal given the RI of the microscope objective used here would require the use of solvents that are not compatible with the objective.

In summary, tissue clearing followed by microscopy of the brain vasculature and *in vivo* ASL-MRI was used in this study to measure cerebrovascular morphology and function in the APP/PS1 mouse model of amyloidosis with high parenchymal plaque burden. No changes were measured with either of the two imaging modalities, indicating that structure and function of the in the mouse brain vasculature are not heavily affected by the presence of amyloid-β plaques. The observed cerebrovascular dysfunction in AD patients may therefore not be much related to the presence of amyloid-β plaques, but originate more from other amyloid-β species such as oligomers and CAA, and/or from other non-amyloid-β-related factors.

ACKNOWLEDGEMENTS

REFERENCES

1. Bateman RJ, Xiong C, Benzinger TLS, Fagan AM, Goate A, Fox NC, Marcus DS, Cairns NJ, Xie X, Blazey TM, Holtzman DM, Santacruz A, Buckles V, Oliver A, Moulder K, Aisen PS, Ghetti B, Klunk WE, McDade E, Martins RN, Masters CL, Mayeux R, Ringman JM, Rossor MN, Schofield PR, Sperling RA, Salloway S, Morris JC (2012) Clinical and Biomarker Changes in Dominantly Inherited Alzheimer's Disease. *N. Engl. J. Med.* 367, 795–804.

2. Selkoe DJ, Hardy J (2016) The amyloid hypothesis of Alzheimer's disease at 25 years. *EMBO Mol. Med.* 8, 595–608.

3. Hays CC, Zlatar ZZ, Wierenga CE (2016) The Utility of Cerebral Blood Flow as a Biomarker of Preclinical Alzheimer's Disease. *Cell. Mol. Neurobiol.* 36, 167–79.

4. Bozzao A, Floris R, Baviera ME, Apruzzese A, Simonetti G (2001) Diffusion and perfusion MR imaging in cases of Alzheimer's disease: correlations with cortical atrophy and lesion load. *AJNR. Am. J. Neuroradiol.* 22, 1030–6.

5. Uh J, Lewis-Amezcua K, Martin-Cook K, Cheng Y, Weiner M, Diaz-Arrastia R, Devous M, Shen D, Lu H (2010) Cerebral blood volume in Alzheimer's disease and correlation with tissue structural integrity. *Neurobiol. Aging* 31, 2038–2046.

6. den Abeelen ASSM, Lagro J, van Beek AHEA, Claassen JAHR (2014) Impaired cerebral autoregulation and vasomotor reactivity in sporadic Alzheimer's disease. *Curr. Alzheimer Res.* 11, 11–7.

7. Iturria-Medina Y, Sotero RC, Toussaint PJ, Mateos-Pérez JM, Evans AC, Weiner MW, Aisen P, Petersen R, Jack CR, Jagust W, Trojanowki JQ, Toga AW, et al. (2016) Early role of vascular dysregulation on late-onset Alzheimer's disease based on multifactorial data-driven analysis. *Nat. Commun.* 7, 11934.

8. Broce IJ, Tan CH, Fan CC, Jansen I, Savage JE, Witoelar A, Wen N, Hess CP, Dillon WP, Glastonbury CM, Glymour M, Yokoyama JS, Elahi FM, Rabinovici GD, Miller BL, Mormino EC, Sperling RA, Bennett DA, McEvoy LK, Brewer JB, Feldman HH, Hyman BT, Pericak-Vance M, Haines JL, Farrer LA, Mayeux R, Schellenberg GD, Yaffe K, Sugrue LP, Dale AM, Posthuma D, Andreassen OA, Karch CM, Desikan RS (2019) Dissecting the genetic relationship between cardiovascular risk factors and Alzheimer's disease. *Acta Neuropathol.* 137, 209–226.

9. Toledo JB, Arnold SE, Raible K, Brettschneider J, Xie SX, Grossman M, Monsell SE, Kukull WA, Trojanowski JQ (2013) Contribution of cerebrovascular disease in autopsy confirmed neurodegenerative disease cases in the National Alzheimer's Coordinating Centre. *Brain* 136, 2697–2706.

10. Mroczko B, Groblewska M, Litman-Zawadzka A, Kornhuber J, Lewczuk P (2018) Amyloid-β oligomers (AβOs) in Alzheimer's disease. *J. Neural Transm.* 125, 177–191.

11. Jellinger KA (2002) Alzheimer disease and cerebrovascular pathology: an update. *J. Neural Transm.* 109, 813–836.

12. Jankowsky JL, Slunt HH, Ratovitski T, Jenkins NA, Copeland NG, Borchelt DR (2001) Co-expression of multiple transgenes in mouse CNS: a comparison of strategies. *Biomol. Eng.* 17, 157–65.

13. Radde R, Bolmont T, Kaeser SA, Coomaraswamy J, Lindau D, Stoltze L, Calhoun ME, Jäggi F, Wolburg H, Gengler S, Haass C, Ghetti B, Czech C, Hölscher C, Mathews PM, Jucker M (2006) Aβ42-driven cerebral amyloidosis in transgenic mice reveals early and robust pathology. *EMBO Rep.* 7, 940–946.

14. Sturchler-Pierrat C, Abramowski D, Duke M, Wiederhold K-H, Mistl C, Rothacher S, Ledermann B, Burki K, Frey P, Paganetti PA, Waridel C, Calhoun ME, Jucker M, Probst A, Staufenbiel M, Sommer

B (1997) Two amyloid precursor protein transgenic mouse models with Alzheimer disease-like pathology. *Proc. Natl. Acad. Sci.* 94, 13287–13292.

15. Davis J, Xu F, Deane R, Romanov G, Previti M Lou, Zeigler K, Zlokovic B V, Van Nostrand WE (2004) Early-onset and robust cerebral microvascular accumulation of amyloid beta-protein in transgenic mice expressing low levels of a vasculotropic Dutch/Iowa mutant form of amyloid beta-protein precursor. *J. Biol. Chem.* 279, 20296–306.

16. Gandy S, Simon AJ, Steele JW, Lublin AL, Lah JJ, Walker LC, Levey AI, Krafft GA, Levy E, Checler F, Glabe C, Bilker WB, Abel T, Schmeidler J, Ehrlich ME (2010) Days to criterion as an indicator of toxicity associated with human Alzheimer amyloid-beta oligomers. *Ann. Neurol.* 68, 220–30.

17. Susaki EA, Tainaka K, Perrin D, Kishino F, Tawara T, Watanabe TM, Yokoyama C, Onoe H, Eguchi M, Yamaguchi S, Abe T, Kiyonari H, Shimizu Y, Miyawaki A, Yokota H, Ueda HR (2014) Whole-brain imaging with single-cell resolution using chemical cocktails and computational analysis. *Cell* 157, 726–739.

18. Kilkenny C, Browne WJ, Cuthill IC, Emerson M, Altman DG (2010) Improving Bioscience Research Reporting: The ARRIVE Guidelines for Reporting Animal Research. *PLoS Biol.* 8, e1000412.

19. Susaki EA, Tainaka K, Perrin D, Yukinaga H, Kuno A, Ueda HR (2015) Advanced CUBIC protocols for whole-brain and whole-body clearing and imaging. *Nat. Protoc.* 10, 1709–1727.

20. Preibisch S, Saalfeld S, Tomancak P (2009) Globally optimal stitching of tiled 3D microscopic image acquisitions. *Bioinformatics* 25, 1463–5.

21. Denis de Senneville B, Zachiu C, Ries M, Moonen C (2016) EVolution: an edge-based variational method for non-rigid multi-modal image registration. *Phys. Med. Biol.* 61, 7377–7396.

22. Hirschler L, Munting LP, Khmelinskii A, Teeuwisse WM, Suidgeest E, Warnking JM, van der Weerd L, Barbier EL, van Osch MJP (2018) Transit time mapping in the mouse brain using time-encoded pCASL. *NMR Biomed.* 31, e3855.

23. Hirschler L, Debacker CS, Voiron J, Köhler S, Warnking JM, Barbier EL (2018) Interpulse phase corrections for unbalanced pseudo-continuous arterial spin labeling at high magnetic field. *Magn. Reson. Med.* 79, 1314–1324.

24. Klein S, Staring M, Murphy K, Viergever MA, Pluim J (2010) elastix: A Toolbox for Intensity-Based Medical Image Registration. *IEEE Trans. Med. Imaging* 29, 196–205.

25. Buxton RB, Frank LR, Wong EC, Siewert B, Warach S, Edelman RR (1998) A general kinetic model for quantitative perfusion imaging with arterial spin labeling. *Magn. Reson. Med.* 40, 383–96.

26. Garcia-Alloza M, Robbins EM, Zhang-Nunes SX, Purcell SM, Betensky RA, Raju S, Prada C, Greenberg SM, Bacskai BJ, Frosch MP (2006) Characterization of amyloid deposition in the APPswe/PS1dE9 mouse model of Alzheimer disease. *Neurobiol. Dis.* 24, 516–524.

27. Fischer VW, Siddiqi A, Yusufaly Y (1990) Altered angioarchitecture in selected areas of brains with Alzheimer's disease. *Acta Neuropathol.* 79, 672–9.

28. Buée L, Hof PR, Delacourte A (1997) Brain microvascular changes in Alzheimer's disease and other dementias. *Ann. N. Y. Acad. Sci.* 826, 7–24.

29. Brown WR, Moody DM, Thore CR, Challa VR, Anstrom JA (2007) Vascular dementia in leukoaraiosis may be a consequence of capillary loss not only in the lesions, but in normal-appearing white matter and cortex as well. *J. Neurol. Sci.* 257, 62–6.

30. Bell MA, Ball MJ Neuritic plaques and vessels of visual cortex in aging and Alzheimer's dementia. *Neurobiol. Aging* 11, 359–70.

31. Nortley R, Korte N, Izquierdo P, Hirunpattarasilp C, Mishra A, Jaunmuktane Z, Kyrargyri V, Pfeiffer T, Khennouf L, Madry C, Gong H, Richard-Loendt A, Huang W, Saito T, Saido TC, Brandner S, Sethi H, Attwell D (2019) Amyloid-β oligomers constrict human capillaries in Alzheimer's disease via signaling to pericytes. *Science* 365, eaav9518.

32. Niwa K, Kazama K, Younkin SG, Carlson GA, Iadecola C (2002) Alterations in Cerebral Blood Flow and Glucose Utilization in Mice Overexpressing the Amyloid Precursor Protein. *Neurobiol. Dis.* 9, 61–68.

33. Massaad CA, Amin SK, Hu L, Mei Y, Klann E, Pautler RG (2010) Mitochondrial Superoxide Contributes to Blood Flow and Axonal Transport Deficits in the Tg2576 Mouse Model of Alzheimer's Disease. *PLoS One* 5, e10561.

34. Faure A, Verret L, Bozon B, El Tannir El Tayara N, Ly M, Kober F, Dhenain M, Rampon C, Delatour B (2011) Impaired neurogenesis, neuronal loss, and brain functional deficits in the APPxPS1-Ki mouse model of Alzheimer's disease. *Neurobiol. Aging* 32, 407–18.

35. Hébert F, Grand'Maison M, Ho M-K, Lerch JP, Hamel E, Bedell BJ (2013) Cortical atrophy and hypoperfusion in a transgenic mouse model of Alzheimer's disease. *Neurobiol. Aging* 34, 1644–1652.

36. Maier FC, Wehrl HF, Schmid AM, Mannheim JG, Wiehr S, Lerdkrai C, Calaminus C, Stahlschmidt A, Ye L, Burnet M, Stiller D, Sabri O, Reischl G, Staufenbiel M, Garaschuk O, Jucker M, Pichler BJ (2014) Longitudinal PET-MRI reveals β-amyloid deposition and rCBF dynamics and connects vascular amyloidosis to quantitative loss of perfusion. *Nat. Med.* 20, 1485–1492.

37. Ni R, Rudin M, Klohs J (2018) Cortical hypoperfusion and reduced cerebral metabolic rate of oxygen in the arcAβ mouse model of Alzheimer's disease. *Photoacoustics* 10, 38–47.

38. Cruz Hernández JC, Bracko O, Kersbergen CJ, Muse V, Haft-Javaherian M, Berg M, Park L, Vinarcsik LK, Ivasyk I, Rivera DA, Kang Y, Cortes-Canteli M, Peyrounette M, Doyeux V, Smith A, Zhou J, Otte G, Beverly JD, Davenport E, Davit Y, Lin CP, Strickland S, Iadecola C, Lorthois S, Nishimura N, Schaffer CB (2019) Neutrophil adhesion in brain capillaries reduces cortical blood flow and impairs memory function in Alzheimer's disease mouse models. *Nat. Neurosci.* 22, 413–420.

39. Hooijmans CR, Rutters F, Dederen PJ, Gambarota G, Veltien A, van Groen T, Broersen LM, Lütjohann D, Heerschap A, Tanila H, Kiliaan AJ (2007) Changes in cerebral blood volume and amyloid pathology in aged Alzheimer APP/PS1 mice on a docosahexaenoic acid (DHA) diet or cholesterol enriched Typical Western Diet (TWD). *Neurobiol. Dis.* 28, 16–29.

40. Delafontaine-Martel P, Lefebvre J, Tardif P-L, Lévy BI, Pouliot P, Lesage F (2018) Whole brain vascular imaging in a mouse model of Alzheimer's disease with two-photon microscopy. *J. Biomed. Opt.* 23, 1.

41. Guo Y, Li X, Zhang M, Chen N, Wu S, Lei J, Wang Z, Wang R, Wang J, Liu H (2019) Age- and brain region-associated alterations of cerebral blood flow in early Alzheimer's disease assessed in AβPPSWE/PS1ΔE9 transgenic mice using arterial spin labeling. *Mol. Med. Rep.*

42. Miao J, Xu F, Davis J, Otte-Höller I, Verbeek MM, Van Nostrand WE (2005) Cerebral Microvascular Amyloid-β Protein Deposition Induces Vascular Degeneration and Neuroinflammation in Transgenic Mice Expressing Human Vasculotropic Mutant Amyloid-β Precursor Protein. *Am. J. Pathol.* 167, 505–515.

43. Ielacqua GD, Schlegel F, Füchtemeier M, Xandry J, Rudin M, Klohs J (2016) Magnetic Resonance Q Mapping Reveals a Decrease in Microvessel Density in the arcAβ Mouse Model of Cerebral Amyloidosis. *Front. Aging Neurosci.* 7, 241.

44. Zerbi V, Jansen D, Dederen PJ, Veltien A, Hamans B, Liu Y, Heerschap A, Kiliaan AJ (2013) Microvascular cerebral blood volume changes in aging APPswe/PS1dE9 AD mouse model: a voxel-wise approach. *Brain Struct. Funct.* 218, 1085–1098.

45. Jankowsky JL, Fadale DJ, Anderson J, Xu GM, Gonzales V, Jenkins NA, Copeland NG, Lee MK, Younkin LH, Wagner SL, Younkin SG, Borchelt DR (2004) Mutant presenilins specifically elevate the levels of the 42 residue β-amyloid peptide in vivo: evidence for augmentation of a 42-specific γ secretase. *Hum. Mol. Genet.* 13, 159–170.

4

46. Iljina M, Garcia GA, Dear AJ, Flint J, Narayan P, Michaels TCT, Dobson CM, Frenkel D, Knowles TPJ, Klenerman D (2016) Quantitative analysis of co-oligomer formation by amyloid-beta peptide isoforms. *Sci. Rep.* 6, 28658.

47. Yoshiura T, Hiwatashi A, Yamashita K, Ohyagi Y, Monji A, Takayama Y, Nagao E, Kamano H, Noguchi T, Honda H (2009) Simultaneous Measurement of Arterial Transit Time, Arterial Blood Volume, and Cerebral Blood Flow Using Arterial Spin-Labeling in Patients with Alzheimer Disease. *Am. J. Neuroradiol.* 30, 1388–1393.

48. Mak HKF, Chan Q, Zhang Z, Petersen ET, Qiu D, Zhang L, Yau KKW, Chu L-W, Golay X (2012) Quantitative Assessment of Cerebral Hemodynamic Parameters by QUASAR Arterial Spin Labeling in Alzheimer's Disease and Cognitively Normal Elderly Adults at 3-Tesla. *J. Alzheimer's Dis.* 31, 33–44.

49. Zhao R, Pollack GM (2009) Regional differences in capillary density, perfusion rate, and P-glycoprotein activity: A quantitative analysis of regional drug exposure in the brain. *Biochem. Pharmacol.* 78, 1052–1059.

50. Bohn KA, Adkins CE, Mittapalli RK, Terrell-Hall TB, Mohammad AS, Shah N, Dolan EL, Nounou MI, Lockman PR (2016) Semi-automated rapid quantification of brain vessel density utilizing fluorescent microscopy. *J. Neurosci. Methods* 270, 124–131.

51. Xiong B, Li A, Lou Y, Chen S, Long B, Peng J, Yang Z, Xu T, Yang X, Li X, Jiang T, Luo Q, Gong H (2017) Precise Cerebral Vascular Atlas in Stereotaxic Coordinates of Whole Mouse Brain. *Front. Neuroanat.* 11, 128.

52. Asllani I, Habeck C, Scarmeas N, Borogovac A, Brown TR, Stern Y (2008) Multivariate and univariate analysis of continuous arterial spin labeling perfusion MRI in Alzheimer's disease. *J. Cereb. Blood Flow Metab.* 28, 725–36.

53. Zonneveld H, Loehrer E, Hofman A, Niessen WJ, van der Lugt A, Krestin GP, Ikram MA, Vernooij MW (2015) The bidirectional association between reduced cerebral blood flow and brain atrophy in the general population. *J. Cereb. Blood Flow Metab.* 35, 1882–7.

54. Zuloaga KL, Davis CM, Zhang W, Alkayed NJ (2014) Role of aromatase in sex-specific cerebrovascular endothelial function in mice. *Am. J. Physiol. Heart Circ. Physiol.* 306, H929-37.

55. Jullienne A, Salehi A, Affeldt B, Baghchechi M, Haddad E, Avitua A, Walsworth M, Enjalric I, Hamer M, Bhakta S, Tang J, Zhang JH, Pearce WJ, Obenaus A (2018) Male and Female Mice Exhibit Divergent Responses of the Cortical Vasculature to Traumatic Brain Injury. *J. Neurotrauma* 35, 1646–1658.

56. Wang J, Tanila H, Puoliväli J, Kadish I, Van Groen T (2003) Gender differences in the amount and deposition of amyloidβ in APPswe and PS1 double transgenic mice. *Neurobiol. Dis.* 14, 318–327.

57. Apostolova I, Wunder A, Dirnagl U, Michel R, Stemmer N, Lukas M, Derlin T, Gregor-Mamoudou B, Goldschmidt J, Brenner W, Buchert R (2012) Brain perfusion SPECT in the mouse: normal pattern according to gender and age. *Neuroimage* 63, 1807–17.

58. Hama H, Kurokawa H, Kawano H, Ando R, Shimogori T, Noda H, Fukami K, Sakaue-Sawano A, Miyawaki A (2011) Scale: a chemical approach for fluorescence imaging and reconstruction of transparent mouse brain. *Nat. Neurosci.* 14, 1481–8.

59. Yang B, Treweek JB, Kulkarni RP, Deverman BE, Chen C-K, Lubeck E, Shah S, Cai L, Gradinaru V (2014) Single-Cell Phenotyping within Transparent Intact Tissue through Whole-Body Clearing. *Cell* 158, 945–958.

60. Ertürk A, Becker K, Jährling N, Mauch CP, Hojer CD, Egen JG, Hellal F, Bradke F, Sheng M, Dodt H-U (2012) Three-dimensional imaging of solvent-cleared organs using 3DISCO. *Nat. Protoc.* 7, 1983–1995.
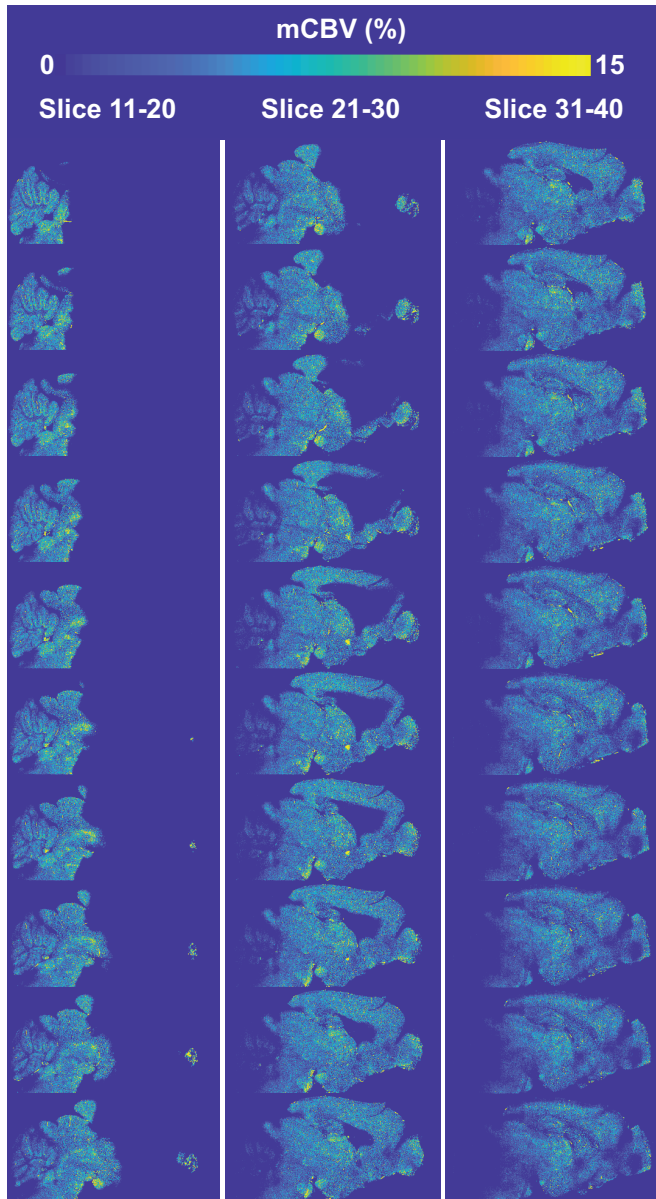
Supplementary figure 1: *Oblique optical sectioning of the microvascular Cerebral Blood Volume (mCBV) maps, showing an axial gradient in mCBV values.*
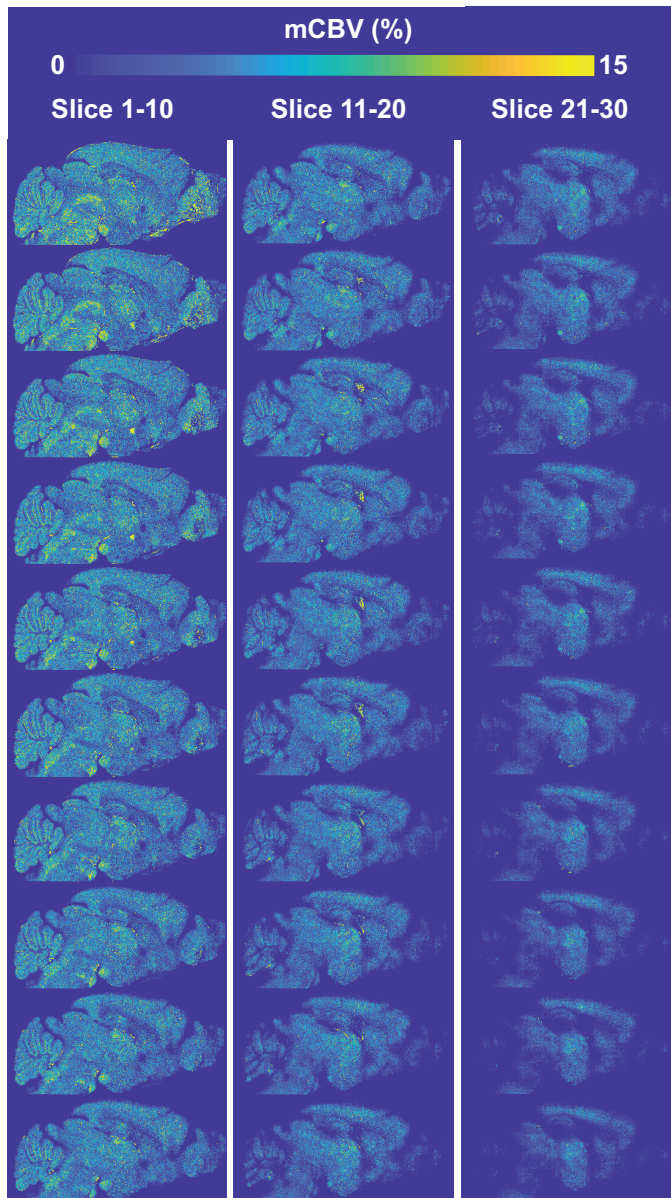
Supplementary figure 2: *Aligned microvascular Cerebral Blood Volume (mCBV) maps, showing decreasing mCBV values with increasing imaging depth.*

Segmented Data

LSM Data

Mouse 1

Mouse 2

4
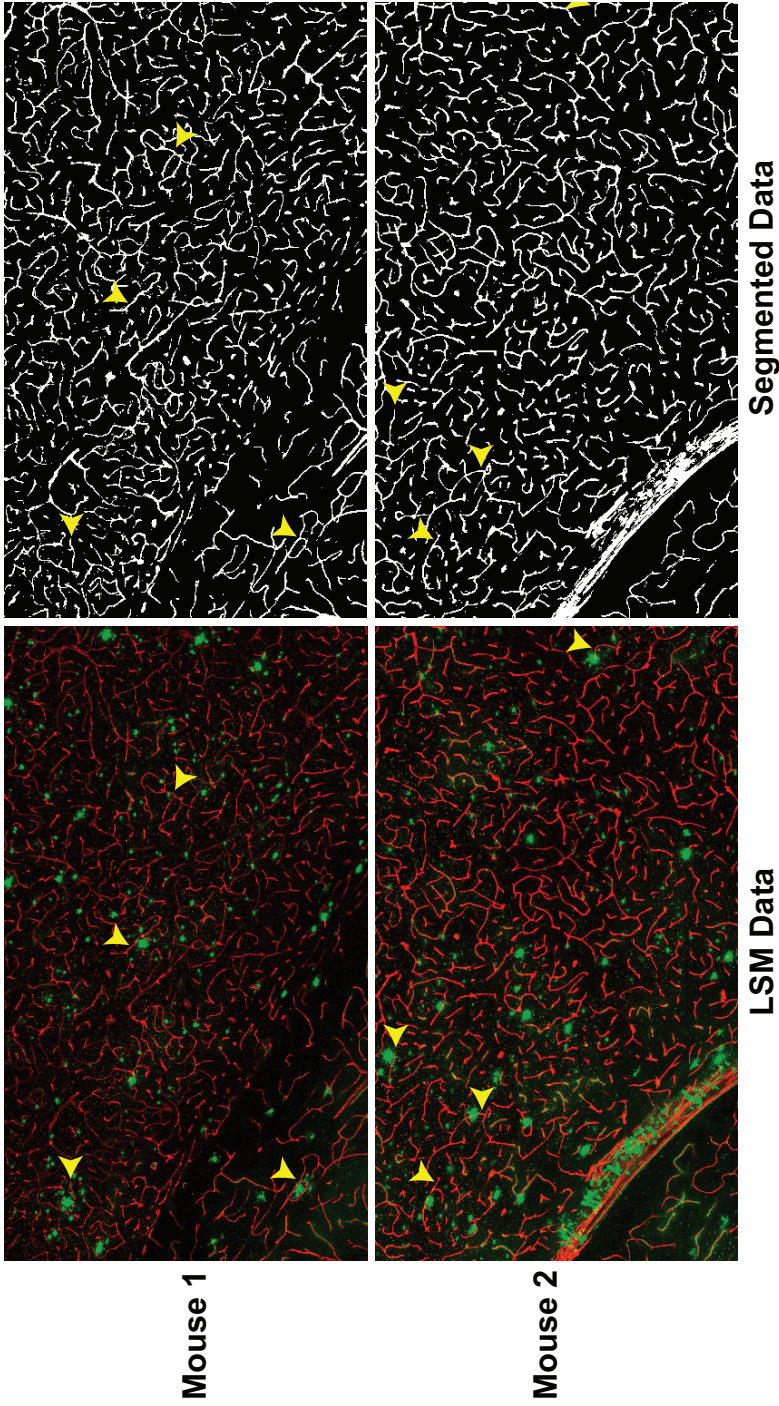
Supplementary figure 3: *Examples of preserved vascular architecture around plaques. The yellow arrowheads point to vessels that are in the close vicinity to plaques, but seem unaffected by them.*

5

Cerebral blood flow and cerebrovascular reactivity are preserved in a mouse model of cerebral microvascular amyloidosis

Leon P Munting[1,2], Marc Derieppe[1,3], Ernst Suidgeest[1], Lydiane Hirschler[1], Matthias JP van Osch[1], Baudouin Denis de Senneville[4,5], Louise van der Weerd[1,2,*]

[1]Department of Radiology, Leiden University Medical Center, Leiden, the Netherlands.
[2]Department of Human Genetics, Leiden University Medical Center, Leiden, the Netherlands.
[3]Present address: Princess Máxima Center for Pediatric Oncology, Utrecht, the Netherlands.
[4]Department of Radiotherapy, University Medical Center Utrecht, Utrecht, the Netherlands.
[5]Institut de Mathématiques de Bordeaux, Université Bordeaux/CNRS UMR 5251/INRIA, Bordeaux-Sud-Ouest, France.

*Correspondence:
Dr. Louise van der Weerd
P.O. Box 9600, Leiden University Medical Center, Albinusdreef 2, 2300 RC Leiden, the Netherlands
Email: l.van_der_weerd@lumc.nl
Tel: +31 71 526 4760

ABSTRACT

Impaired cerebrovascular function is an early biomarker for cerebral amyloid angiopathy (CAA), a neurovascular disease characterized by amyloid-β accumulation in the cerebral vasculature, leading to stroke and dementia. The transgenic Swedish Dutch Iowa (Tg-SwDI) mouse model develops cerebral microvascular amyloid-β deposits, but whether this leads to similar functional impairments is incompletely understood. We assessed cerebrovascular function longitudinally in Tg-SwDI mice with arterial spin labeling (ASL)-MRI and laser Doppler flowmetry (LDF) over the course of amyloid-β deposition. Unexpectedly, Tg-SwDI mice showed similar baseline perfusion and cerebrovascular reactivity estimates as age-matched wild type control mice, irrespective of modality (ASL or LDF) or anesthesia (isoflurane or urethane and α-chloralose). Hemodynamic changes were however observed as an effect of age and anesthesia. Our findings contradict earlier results obtained in the same model and question to what extent microvascular amyloidosis as seen in Tg-SwDI mice is representative of cerebrovascular dysfunction observed in CAA patients.

INTRODUCTION

Cerebral amyloid angiopathy (CAA) is a neurovascular disease characterized by accumulation of the amyloid-β peptide in the brain vasculature, which ultimately leads to stroke and cognitive decline.[1] In both hereditary and sporadic variants of CAA, measurements in patients have shown that impairments in cerebrovascular function can be found early in the disease process.[2,3] These measurements were performed with BOLD-fMRI and a visual stimulation paradigm, allowing to characterize the cerebrovascular response to neuronal activation in the occipital cortex, where visual processing occurs. The occipital cortex is also where CAA burden is highest,[4] likely contributing to the sensitivity of the fMRI measurement.

Mouse models of cerebral amyloidosis are invaluable tools for testing safety and effectiveness of greatly needed novel therapies for amyloid-β-related diseases, including CAA. However, for the results to be translatable to the clinic, it is essential that the amyloidosis model shows similar structural and functional phenotypes as the patient. The transgenic Swedish Dutch Iowa (Tg-SwDI) mouse model is an amyloidosis model expressing low levels of the human amyloid-β precursor protein (APP) gene with 3 familial mutations, of which the Dutch and Iowa mutations are located in the amyloid-β coding region of APP.[5] The neuronal expression of the mutated APP in this model leads to early amyloid-β accumulation in the brain, starting around 6 months. Amyloid-β accumulates predominantly around capillaries in the Tg-SwDI model, which is similar to a subtype of CAA pathology observed in pathological examinations of patient tissue and sometimes referred to as capCAA.[6] It is unknown to what extent amyloid-β accumulation around capillaries contributes to the observed impairments in cerebrovascular function in patients. Unlike patients, vascular pathology in the Tg-SwDI model is most severe in the thalamus.[7] Previous studies have measured cortical vascular reactivity using laser Doppler flowmetry (LDF) after removal of the skull in Tg-SwDI and wild type (WT) mice. They reported, similar to CAA patients, early impairments in CVR in Tg-SwDI mice.[8,9] It is unknown however, whether skull removal has affected the outcome, and whether the thalamus is more strongly affected, as the thalamus is not readily accessible with LDF.

Here, we therefore used the non-invasive arterial spin labeling (ASL)-MRI technique to study the cerebrovascular function in the Tg-SwDI brain. With ASL, arterial blood is magnetically labeled and used as endogenous tracer flowing into the tissue of interest, which is most often the brain. The distribution of the label over the different brain regions reflects local tissue perfusion and can be converted into absolute cerebral blood flow (CBF) values, expressed as mL/100 g/min. When combined with a hypercapnic challenge, both CBF and CVR can be determined for different brain regions. A known unfavorable characteristic of ASL is a possible underestimation of CBF in case of slow flow. In that case, a delayed

5

Arterial Transit Time (ATT) – the time that it takes for the label to travel from the labeling plane to the brain tissue – could be misinterpreted as decreased CBF. ATT evaluation is therefore valuable to prevent a potential underestimation of the ASL-based CBF estimates, as well as indicative in itself of vascular pathology.[10]

The non-invasive nature of ASL was fully exploited in our study with the use of a longitudinal study design in which CBF and CVR were repeatedly measured during increasing amyloid-β accumulation in the brain vasculature of Tg-SwDI mice. As it is conceivable that high microvascular amyloid burden could lead to delayed ATT in Tg-SwDI mice, an ATT measurement was added to the protocol by means of a modified ASL sequence optimized to capture the inflow of the tracer into the brain tissue.[11] To allow for repeated measurements, a minimally invasive isoflurane anesthesia protocol was used. Moreover, to be able to compare the results to literature, additional end-point measurements were performed under a terminal anesthesia protocol with urethane and α-chloralose (U&A). Furthermore, a subgroup of mice was used to directly compare ASL-MRI to LDF. The study design is summarized in Figure 1.
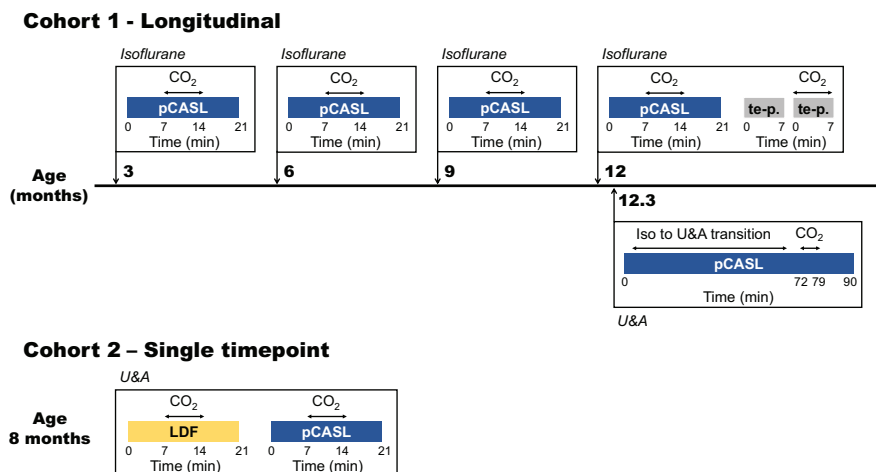
Figure 1: Study design. Two different cohorts were used in this study, of which the first was followed longitudinally. The timeline of the first cohort is illustrated in the upper part of the figure, with scan moments indicated with orthogonal arrows projected onto the time line. The most relevant scans performed at these moments are indicated within the boxes adjoined to the orthogonal arrows and the type of anesthesia used is indicated in italic on top of the boxes. The lower part of the figure illustrates the single time point measurements performed in cohort 2. pCASL = pseudo-continuous arterial spin labeling; te p. = time-encoded pseudo-continuous arterial spin labeling; U&A = urethane and α-chloralose; LDF = laser Doppler flowmetry.

RESULTS

Hypercapnia consistently induced a CBF increase in both WT and Tg-SwDI mice under isoflurane anesthesia (Figure 2 and Figure 3), which was mainly located in cortical regions (Figure 2)). Surprisingly, the CBF maps and CBF time profiles acquired in the mid-brain of the Tg-SwDI mice resembled those of the WT mice at every time point. Hence no significant differences were observed in baseline CBF nor CVR between the two genotypes at any time point (Figure 3b; see Figure 3-figure supplement 1 for individual animal trends). A significant effect of age on CBF was however observed in both WT and Tg-SwDI mice, $\chi^2(3)$ = 13.00, p = 0.005 and $\chi^2(3)$ = 8.49, p = 0.037, respectively. Post-hoc analysis indicated that this was attributable to a decrease in baseline CBF between the ages of 3 and 6 months. Between these time points, median (iqr) CBF significantly decreased from 155 (143-159) to 121 (112-124) mL/100 g/min in WT mice, p = 0.008. In Tg-SwDI mice, a similar trend was observed, from 147 (133-151) to 126 (103-135) mL/100 g/min, p = 0.036, but this was not significant (cut-off p-value of 0.017 after Bonferroni correction). From 6 months of age, the baseline CBF remained stable inside each group. Age also had a significant effect on CVR in WT mice, $\chi^2(3)$ = 8.33, p = 0.040. No differences were observed with post-hoc analysis however, besides a trend towards increased CVR between the ages of 3 and 6 months, from 13 (7-17) to 31 (23-37) %, p = 0.038. Age had no significant effect on CVR in Tg-SwDI mice, $\chi^2(3)$ = 6.94, p = 0.074. Additional analysis in cortical and thalamic areas did not reveal any difference between WT and Tg-SwDI mice either (Figure 3-figure supplement 2). Similarly, no differences were observed in brain volume, body weight, change in tc-pCO_2 upon the hypercapnia challenges, respiration rate and inversion efficiency between WT and Tg-SwDI mice (Figure 3-figure supplement 1, Figure 3-figure supplement 3 and Figure 3-figure supplement 4). Of note, the CBF at 12 months showed higher variability in the WT group, and the body weights showed higher variability in the Tg-SwDI group.

Median (iqr) baseline ATT values in the mid-brain were also similar for both WT and Tg-SwDI mice, i.e. 206 (186-240) milliseconds (ms) and 223 (202-246) ms respectively at 12 months of age (Figure 4). The hypercapnia challenge shortened the ATT to 192 (189-205) for WT and 197 (187-207) for Tg-SwDI mice, which was significant for Tg-SwDI mice (Z = -2.20 and p = 0.028), but did not reach significance for WT mice (Z = -1.84 and p = 0.066).

5

CBF baseline (mL/100 g/min)

CBF during CO_2 (mL/100 g/min)

Cerebrovascular reactivity (%)
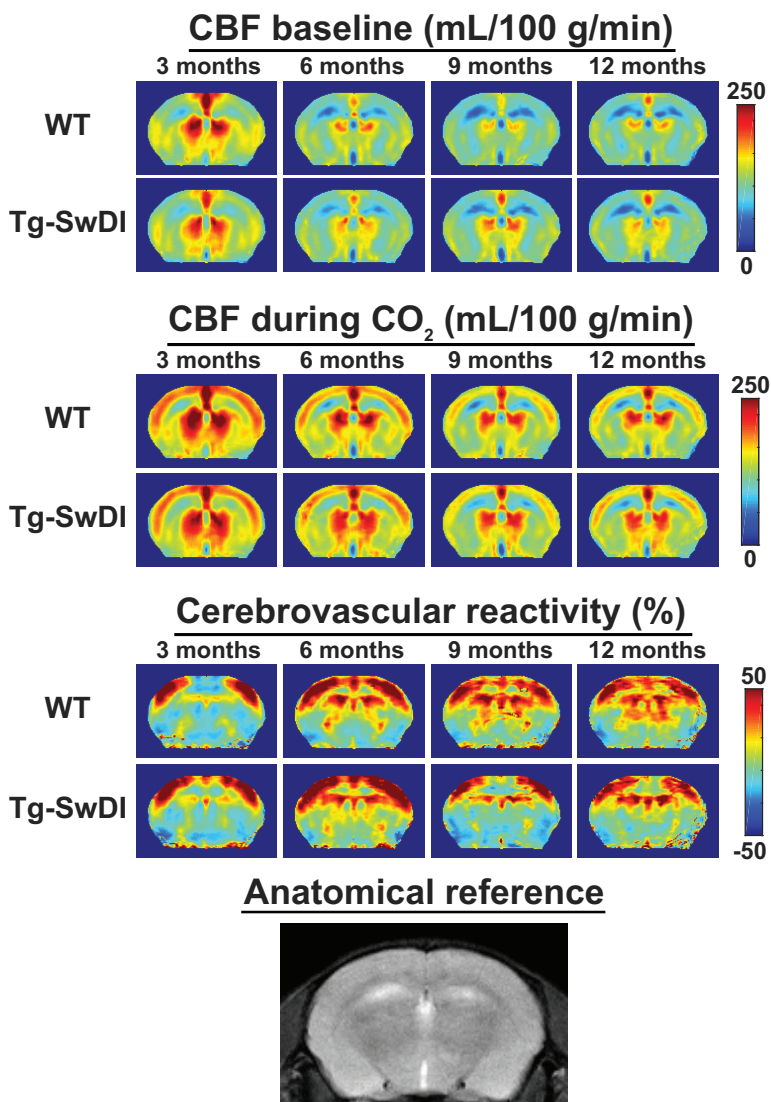

Anatomical reference

Figure 2: Average mid-brain cerebral blood flow (CBF) and cerebrovascular reactivity (CVR) maps for wild type (WT) and transgenic Swedish Dutch Iowa (Tg-SwDI) mice in cohort 1. From left to right, the different ages are displayed. From top to bottom, respectively CBF maps at baseline, CBF maps during CO_2 and CVR maps are displayed, with WT and Tg-SwDI mice alternating per row. On the bottom row, an anatomical MRI scan of the same brain slice is shown. Note that the CBF increase during the CO_2 challenge is most profound in the cortex, and that the WT and Tg-SwDI mice show similar CBF and CVR maps.
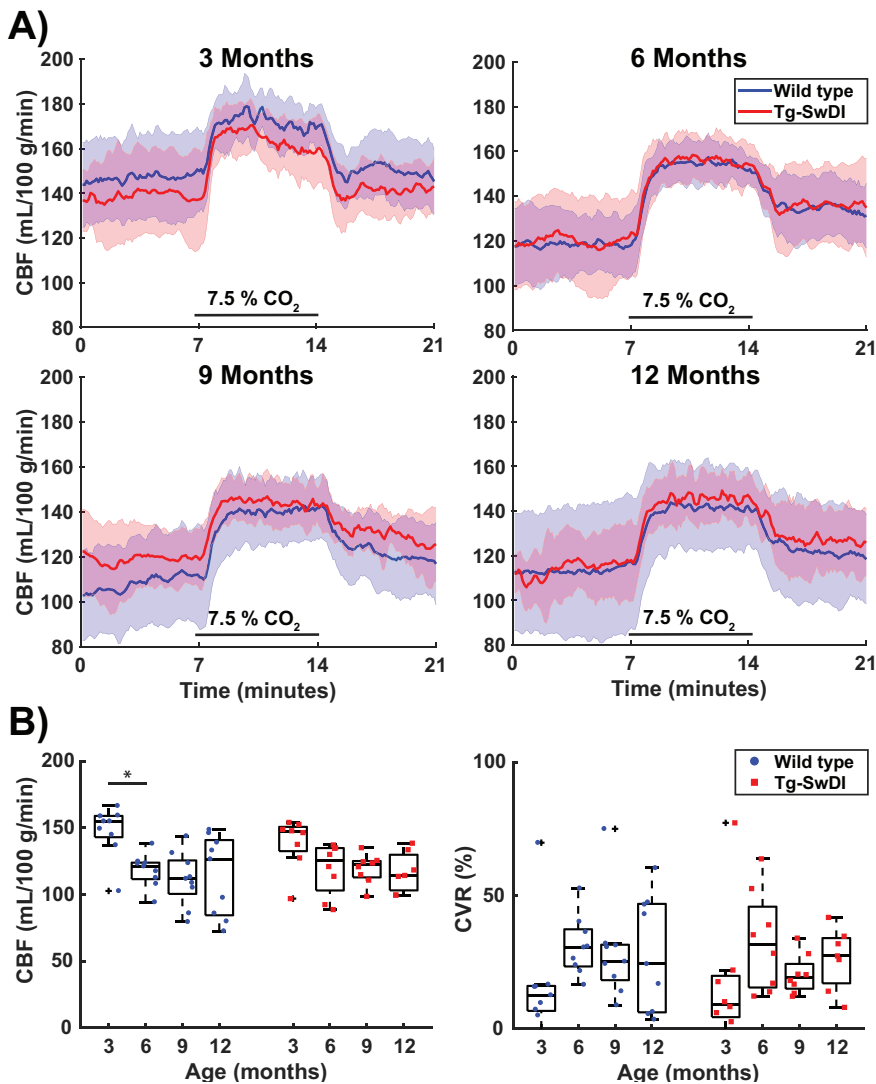
Figure 3: Cerebral blood flow (CBF) and cerebrovascular reactivity (CVR) values acquired in the mid-brain in cohort 1. A) displays 21-minute CBF time profiles (mean ± standard deviation) that were retrieved in a full mid-brain slice at the ages of 3,6,9 and 12 months old shows for wild type (WT) and transgenic Swedish Dutch Iowa (Tg-SwDI) mice. CO_2 was administered between minute 7 and 14.B) shows boxplot representations of baseline CBF (average of the last 2.3 minutes before the start of CO_2 administration) and CVR (ratio of average of the last 2.3 minutes during CO_2 to baseline CBF). Circles and squares represent individual mice. No significant differences were observed between the two genotypes, but there was a significant effect of age (Friedman test, $p = 0.005$ for CBF in WT, $p = 0.037$ for CBF in TG, $p = 0.040$ for CVR in WT). From the post-hoc analysis, only the drop in CBF in WT mice between 3 and 6 months old ($p = 0.008$) reached the Bonferroni-corrected significance threshold ($p = 0.017$).

To evaluate if a functional deficit could have been masked by the vasodilatory effect of isoflurane during the MRI sessions, additional CBF and CVR measurements were performed in the same cohort of mice under urethane and alpha-chloralose (U&A) anesthesia. This was done at 12.3 months, 10 days after the last MRI measurement under isoflurane. The change of anesthesia protocol resulted in profound hemodynamic changes: baseline CBF was markedly reduced and the hypercapnic response was higher in amplitude, but also slower (Figure 5a), and more widespread in the brain tissue (Figure 5b). The CBF and CVR estimates were indeed significantly impacted by the change in anesthesia protocol (Figure 5c), with the median CBF (iqr) decreasing from 126 (84-141) to 28 (26-30) mL/100 g/min in WT mice, Z = -2.67 and p = 0.008, and median (iqr) CVR increasing from 26 (6-47) to 233 (193-245) %, Z = -2.67 and p = 0.008. These changes were again comparable to those in Tg-SwDI mice, with the median CBF (iqr) and CVR (iqr) respectively changing from 114 (103-130) to 25 (21-40) mL/100 g/min, Z = - 2.37 and p = 0.018, and from 30 (17-34) to 265 (178-312) %, Z = -2.37 and p = 0.018. The CBF response at the induction phase of U&A anesthesia was also similar in Tg-SwDI and WT mice (Figure 5-figure supplement 1). The higher CVR during U&A was unlikely due to a higher CO_2 absorption, as the tc-pCO$_2$ responses to the hypercapnia challenges only increased from an average of 15 mmHG during isoflurane to an average of 19 mmHG during U&A (Figure 5-figure supplement 2).
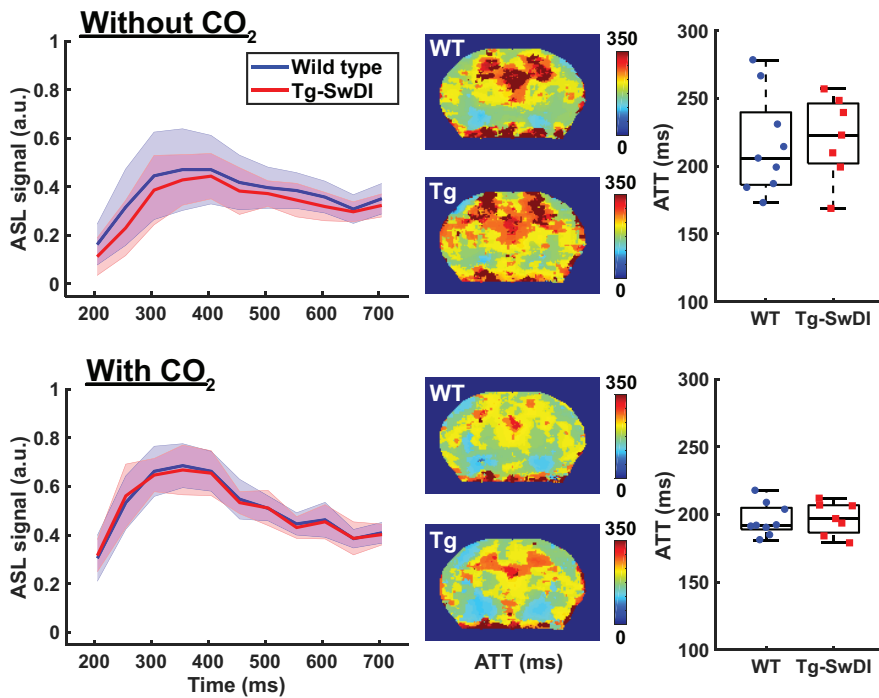
Figure 4: Arterial Transit Time (ATT) measurements acquired in the mid-brain of 12-months old wild type (WT) and transgenic Swedish Dutch Iowa (Tg-SwDI) mice. On the top row, measurements acquired at baseline are displayed, on the bottom row measurements acquired while administering 7.5 % CO_2. On the left column, graphs display the measured arterial spin labeling (ASL) signal (mean ± standard deviation) plotted against increasing post-label delay times. In the middle, maps are displayed that show averaged arrival times of the ASL signal. The maps were acquired in a mid-brain slice and are averaged for WT (top) and Tg-SwDI mouse (bottom). On the right, boxplot representations of the ATT values obtained in all mice are displayed, where circles and squares represent individual mice.

5
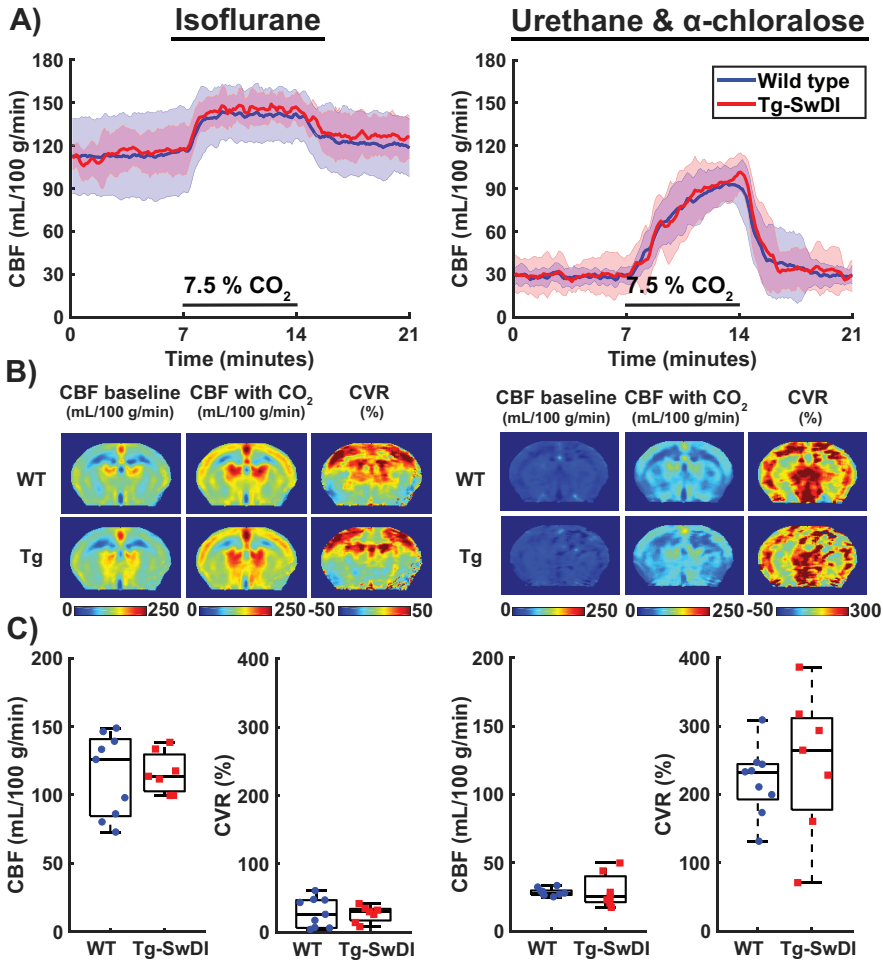
Figure 5: Cerebral blood flow (CBF) and cerebrovascular reactivity (CVR) acquired during isoflurane anesthesia and urethane & α-chloralose (U&A) anesthesia. A) displays 21-minute CBF time profiles acquired in the mid-brain in wild type (WT) and transgenic Swedish Dutch Iowa (Tg-SwDI) mice under either isoflurane anesthesia (left, 12 months old) or U&A anesthesia (right, 10 days later in the same mice). CO_2 was administered between minute 7 and 14. B) displays mid-brain CBF and CVR maps averaged for WT (top) and Tg-SwDI (bottom) mice. Note that the CVR maps during U&A anesthesia are scaled differently than the CVR maps under isoflurane due to the marked difference in CVR. C) displays boxplot representations of the baseline CBF and CVR group values, where dots and circles represent individual mice.

An additional smaller second cohort of mice was used to cross-validate our MRI findings with the previously used LDF readout as imaging modality to assess cerebrovascular function in this mouse model.[8,9] After a unilateral craniotomy (right side), LDF measurements were performed with two probes at the same time: one through the skull in the left hemisphere and the other directly above the brain tissue in the right hemisphere. MRI measurements were performed directly after the LDF measurement in the same mice and the brain region analyzed with the MRI data was restricted to the somatosensory cortex, where the LDF measurements were also collected. No differences in CVR could be observed between WT and Tg-SwDI mice, neither with MRI, nor with LDF (Figure 6). Of note, removal of the skull severely reduced the CVR for both imaging modalities (Figure 6-figure supplement 1).
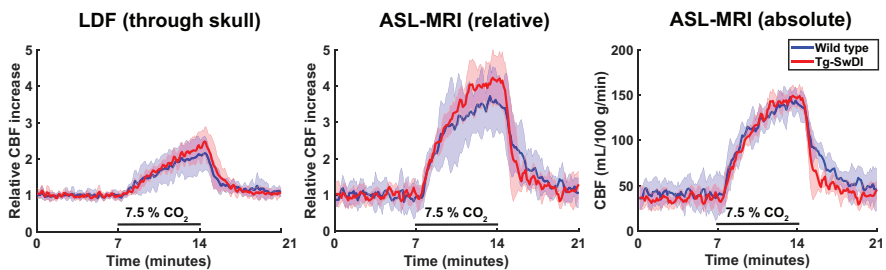
Figure 6: *Cerebral blood flow (CBF) time profiles acquired with laser Doppler flowmetry (LDF) and Arterial Spin Labeling (ASL)-MRI.* On the left, 21-minute CBF time profiles acquired with LDF in the somatosensory cortex are displayed for wild type (WT) and transgenic Swedish Dutch Iowa (Tg-SwDI) mice. In the middle, 21-minute CBF time profiles are displayed that are acquired with ASL-MRI in the left somatosensory cortex, after baseline correction, so the profiles can be compared to the LDF time profiles. On the right are the same profiles as in the middle, without baseline correction.

Lastly, the brain tissue was stained for amyloid-β to assess the degree of pathological burden. All Tg-SwDI mice developed extensive amyloid-β plaque pathology by the end of the experiment, with mainly diffuse parenchymal plaques in the cortex and microvascular plaques in the hippocampus and thalamus, but none of the WT mice displayed any amyloid-β deposition (Figure 7).
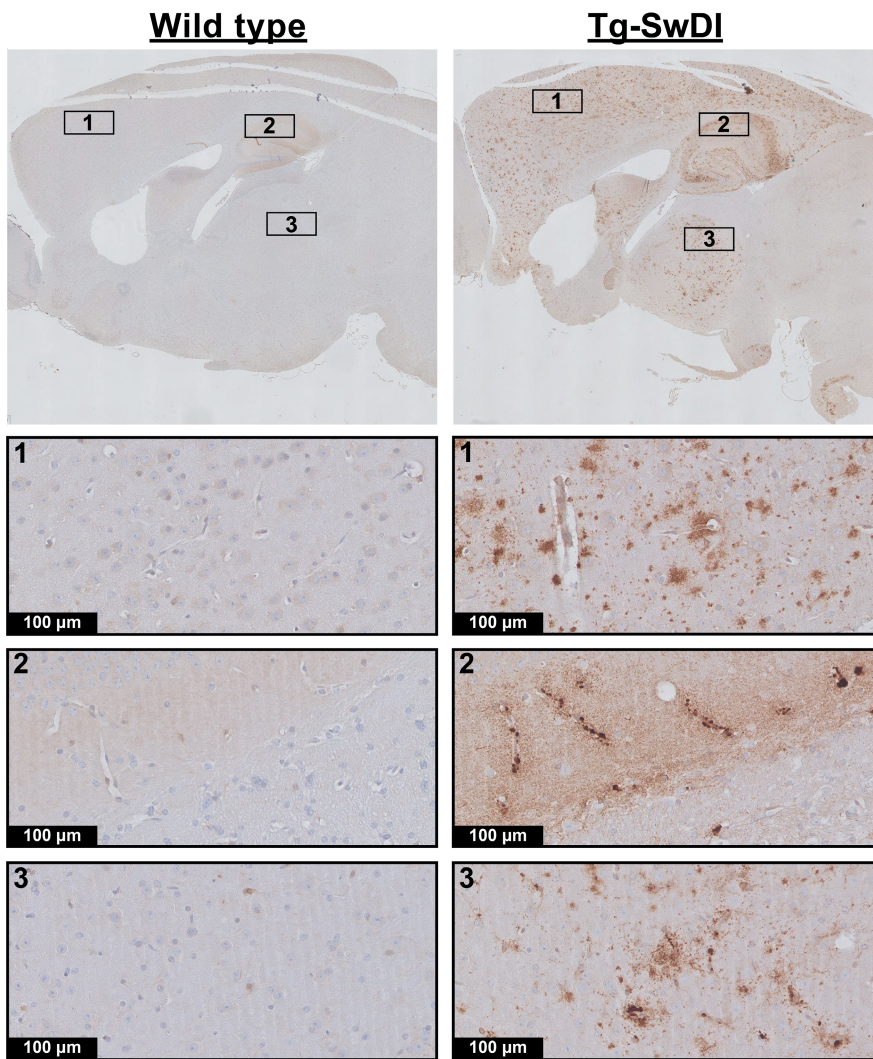
Figure 7: Amyloid-β histology. Shown are representative stainings of wild type (WT) and transgenic Swedish Dutch Iowa (Tg-SwDI) mice of 12.3 months old. The upper row is an overview image, the other rows are zoomed in regions from the overview image.

DISCUSSION

This longitudinal study characterized cerebrovascular function in the Tg-SwDI mouse model of microvascular amyloidosis over the full course of amyloid-β pathogenesis. No significant impairment in cerebrovascular function could be found in the Tg-SwDI model, no matter the age or functional parameter explored. This contradicts previous findings, which showed early impairments in cerebrovascular reactivity (CVR) in the cerebral cortex in Tg-SwDI mice using LDF.[8,9] In our study, cerebrovascular function was first assessed using Arterial Spin Labeling (ASL)-MRI and a CO_2 challenge, allowing to measure absolute CBF as well as CVR in the entire brain. The ASL-MRI perfusion data were acquired longitudinally using a low-level isoflurane anesthesia protocol to capture the dynamics of decreasing cerebrovascular function over increasing microvascular amyloid-β loads. This study setup was substantially different from literature studies, where relative CBF measurements performed using LDF under a terminal anesthesia protocol with urethane and α-chloralose (U&A), after removal of the skull, showed impaired hemodynamics in the Tg-SwDI mouse model.[8,9] Therefore, additional experiments were performed to determine whether differences in experimental design could explain this discrepancy. A likely candidate was the difference in anesthesia protocol, as this has been shown to significantly influence CVR experiments.[12,13] Another likely candidate was the difference in imaging modality, as ASL-MRI and LDF are sensitive to different blood components, namely flux of blood plasma (ASL-MRI) or velocity of red blood cells (LDF). However, after differences in anesthesia protocol and imaging modality were accounted for, cerebrovascular function was in our hands still found to be preserved in the Tg-SwDI model. Practically, it is very difficult to replicate an experiment up to the smallest detail in a different laboratory, as small differences might remain. However, by showing similar findings for two modalities and two anesthesia protocols, including the ones used before, we think that our study convincingly shows that microvascular amyloidosis in the Tg-SwDI mouse model does not induce cerebrovascular dysfunction. Moreover, the robustness to sense local hemodynamic changes could be confirmed based on the observed reduced CBF and CVR as a function of age and anesthesia. The CBF time profiles of Tg-SwDI mice were in fact remarkably similar to their wild type controls, even when CBF was monitored for up to 1.5 hours (Figure 5-figure supplement 1). Everything considered, our functional results indicate that the causal link between microvascular amyloidosis and cerebrovascular function, which was established in past studies in the Tg-SwDI model, is to be mitigated and remains to be fully uncovered.

Some remaining differences between our approach and those of others are however useful to mention and could possibly provide explanations for the different outcomes found between studies. For instance Chow *et al.*,[8] and also Park *et al.*,[9] used heterozygotic Tg-SwDI mice, whereas in this study, homozygotic Tg-SwDI mice were used. Homozygotic Tg-SwDI mice have been reported to develop more extensive amyloid-β pathology, but with

5

a similar distribution on the micro- and macro-scale in the brain, and similar amyloid-β-40/amyloid-β-42 ratios as hemizygous mice.[14] It seems however unlikely that the more severe pathology would result in a reversal of the functional phenotype. Furthermore, the amyloid-β pathology found here (Figure 7) is comparable to what is described in the literature for both hemizygous and homozygous mice, namely diffuse parenchymal plaques in the cortex and microvascular accumulation in the thalamus and hippocampus.[7] Secondly, we used a higher percentage of CO_2 for our vascular challenge, i.e. 7.5 % for 7 minutes here, versus 5 % for 5 minutes in literature.[9] However, it is unlikely that higher pCO_2 intake would reverse the phenotype of the Tg-SwDI mice. Furthermore, the pCO_2 increase measured here through the skin during U&A is comparable to that reported with blood gas sampling in Park *et al.*[9] (approximately 20 mmHg). Possibly, a lower sensitivity of the transcutaneous pCO_2 measurement versus blood gas sampling could explain why our pCO_2 increase was not higher. It is also important to mention that in most patient studies,[2,3] as well as in Chow *et al.*,[8] vascular responses to neuronal activity were measured, not baseline perfusion and hypercapnia, which might be differently affected by vascular amyloid-β. However, this is not likely to explain the differences in outcomes, as Park *et al.*,[9] showed impaired responses in Tg-SwDI mice to both hypercapnia and neuronal activity. Furthermore, patient studies have also shown baseline perfusion deficits.[3] Lastly, in Chow *et al.*,[8] and Park *et al.*,[9] a craniotomy was performed right before the LDF measurement, whereas here, most of the measurements were performed non-invasively. An attempt was made to account for this difference in experimental set-up by preparing an acute craniotomy in the second cohort of mice. However, even though the brain surface in these animals was visually normal (Figure 6-figure supplement 1) after the craniotomy, edema was observed with MRI, and with both imaging modalities marked reductions in CBF and CVR were measured in the underlying brain regions in both WT and Tg-SwDI mice. A likely explanation for the functional impairments after craniotomy is the occurrence of a cortical spreading depression (CSD), which occurs even at minor manipulations on the dura.[15] In mice specifically, CSDs have been reported to cause a CBF reduction of 40-50 %, and enhanced resistance to relaxation by acetylcholine.[15] It could be hypothesized that the presence of amyloid-β in the Tg-SwDI model enhances the sensitivity of the brain tissue to a CSD. Thus, when measured just after craniotomy, the unnoticed presence of a CSD might give the false idea of direct amyloid-β induced cerebrovascular dysfunction. Interestingly, a recent study also reported that skull removal was necessary to detect cerebrovascular dysfunction in a different mouse model of amyloid-β accumulation, providing some support for this hypothesis.[16] Nevertheless, because our wild type mice showed similar functional deficits as the Tg-SwDI mice, we currently cannot substantiate this hypothesis. It is important to mention that the researcher that performed the craniotomy in this study is highly skilled in this procedure, underlining that this is not merely a matter of experience. Hence, it is of interest to elucidate in future research if our surgical procedure indeed triggers a CSD, and whether Tg-SwDI mice are more susceptible to CSDs.

Alternatively, our results could indicate that the mouse cerebral circulation is less affected by amyloid-β accumulation than the human cerebral circulation. However, other amyloidosis models did show early impairments in cerebrovascular function, even in a non-invasive set-up, such as the APP23 model.[17,18] Because the APP23 model mainly shows arteriolar CAA pathology,[19] altogether this might indicate that predominantly CAA pathology on the *arteriolar* side of the vasculature is responsible for the observed CBF and CVR impairments in patients. It is important to note however, that even without CBF limiting pathology, capillary dysfunction could lead to inefficient oxygen extraction from the capillary network.[20] Indeed, hypoxia-induced factor angiopoietin-4 was found to be highly expressed in capCAA patients,[21] indicating that possibly capCAA could induce hypoxic conditions. It would thus be interesting to validate whether similar conditions are found in the Tg-SwDI mouse model.

To the best of our knowledge, this is the first study with ASL-MRI in mice where the CBF responses to hypercapnia under isoflurane and U&A anesthesia were directly compared. Large differences in hemodynamic parameters were observed, with the very low CBF during U&A anesthesia as the most striking observation. The low CBF during U&A is non-physiological and thus forms a limitation of this study. Interestingly, U&A is considered one of the more suitable anesthesia protocols for cerebral hemodynamic studies in mice, as this protocol has been reported to have relatively mild hemodynamic effects[22,23] and to maintain cerebral autoregulation.[24] However, these studies did not provide absolute CBF estimates, and our results indicate that the stable hemodynamics come together with very low baseline CBF, which may not always be favorable and certainly do not represent normal baseline physiology. It would be of interest to identify the underlying cause for this low CBF.

This is also one of the few studies where a direct comparison was established between hypercapnic CBF responses measured with ASL-MRI versus LDF. The results must however be interpreted with care due to the small group size and the ± 0.5-hour delay between the two measurements. Both readouts consistently reported preservation of cerebrovascular function in Tg-SwDI mice and a severe reduction of CVR after craniotomy, but CVR measurements with ASL-MRI were nearly twice as high compared to those obtained with LDF. It is unclear where this difference comes from. As the two imaging modalities are sensitive to different blood components (plasma or red blood cells), it could be argued that local hematocrit changes during hypercapnia could explain this difference. Indeed, hematocrit has been reported to decrease during hypercapnia in the rat brain,[25] but with only a 10 % decrease during a 10 % CO_2 challenge, which is too low to explain the observed difference. A more convincing explanation could be found in an interesting study where ASL-MRI and LDF were performed simultaneously,[26] and point in the direction of an underestimation by LDF. The authors showed that by varying the fiber separation distance in the LDF probe, which changes the measured cortical depth, a different CBF response was measured. Consequently, the magnitude of the CBF response was either comparable to that measured with ASL-MRI, or up to two times lower, which

5

is comparable to our results. The authors measured CBF responses to electrical whisker stimulation through a thinned skull in rats under urethane anesthesia, and concluded that when larger cortical depths were measured, LDF underestimated the CBF response. It is unclear how these results would exactly translate to our different set-up (smaller cortical thickness in the mouse, intact skull, different vascular challenge), but indicates that investigating the cortical depth measured with a set-up like ours is a compelling area for future research. Interestingly, the absolute CBF responses measured with ASL-MRI by He *et al.*,[26] were comparable to those measured here.

Lastly, another finding in our study that is of interest, is the observation of edema and the local reduction in CBF and CVR with MRI after craniotomy. This was observed in all animals, while the brain tissue was normal by visual inspection. Normal appearance of brain tissue is therefore not enough to conclude that the brain tissue is healthy when working with acutely prepared cranial windows.

In conclusion, this study shows that cerebrovascular function in the Tg-SwDI mouse model of microvascular amyloidosis is preserved up to 12 months of age, despite the high amyloid-β burden observed at that age. This observation was confirmed using two different anesthesia protocols and two different imaging modalities. These observations call into question to what extent microvascular amyloidosis as seen in the Tg-SwDI mouse model is a correct model for cerebrovascular dysfunction as observed in CAA patients, and calls for further research to clear up the discrepancy in results.

MATERIALS AND METHODS

Key Resources Table

Reagent type (species) or resource	Designation	Source or reference	Identifiers	Additional information
Strain, strain background (*Mus musculus*)	C57Bl/6J (WT)	Jackson lab	Stock No: 000664	
Strain, strain background (*Mus musculus*)	C57BL/6-Tg(Thy1-APPSwDutIowa) BWevn/Mmjax (Tg-SwDI)	Jackson lab	MMRRC Stock No: 34843-JAX	
Antibody	Anti-beta amyloid antibody (rabbit polyclonal)	Abcam	ab2539	1:1000 dilution
Antibody	Anti-rabbit IgG antibody (pig polyclonal)	Dako	E0431	1:300 dilution
Chemical compound, drug	α-Chloralose	Sigma-Aldrich	C0128	50 mg/kg
Chemical compound, drug	Urethane	Sigma-Aldrich	U2500	750 mg/kg
Software, algorithm	DASYLab	National Instruments		Version 13
Software, algorithm	MATLAB	Mathworks	RRID:SCR_001622	
Software, algorithm	ImageJ	NIH	RRID:SCR_003070	
Software, algorithm	SPSS	IBM	RRID: SCR_002865	Version 26
Software, algorithm	EVolution	Denis de Senneville et al.	Phys Med Biol 2016	
Software, algorithm	MIA / MP3	Brossard et al.	Front Neuroinform 2020	
Software, algorithm	G*Power	Faul et al.	Behav Res Methods 2007	
Other	Avidin-Biotin Complex kit	Vector Laboratories	Vectastain	

Animals

All the experiments were approved by the local ethics committee ("Leiden University Medical Center Instantie voor Dierenwelzijn") and the national ethical committees ("Centrale Commissie Dierproeven") under OZP PE.18.029.002 of AVD116002017859, and the experiments have been reported in compliance with the ARRIVE guidelines.[27]

Two cohorts of homozygous Tg-SwDI mice and age- and gender-matched WT controls on a C57Bl/6J background were ordered from the Jackson Laboratory (Bar Harbor, ME, USA). The first cohort was used for a hypothesis-driven study. Based on a previous report by Park *et al.,*[9] we expected an effect size of 30 percentage points difference - in cortical CBF response to a hypercapnia challenge - between Tg-SwDI and wild type mice, and a standard deviation of 12 % in both groups. With a power calculation done with G*Power software,[28] where we assumed an alpha of 0.05 and a power of 80 % for a two-sided Mann-Whitney U test, we estimated 4 animals would be needed to detect a significant difference in cortical CVR. However, to counteract the possibility of a lower effect size, higher standard deviation and/or animal drop-out, we chose to increase our sample size with 5 animals per group, thus to 9 animals per group in total. The cohort consisted of all male mice which were followed longitudinally, i.e. they were imaged at 3, 6, 9, 12, and 12.3 months of age. The second cohort was used for an exploratory study and consisted of 4 Tg-SwDI (2 females) and 4 WT mice (2 females) which were imaged once at 8 months of age. No blinding was performed when the mice were imaged. Two of the transgenic mice were taken out of the longitudinal study, which was not related to the study itself: the first mouse was severely wounded by a cage mate (at 2.5 months of age), the other due to ulcerative dermatitis (at 10 months of age). The mice in the longitudinal cohort were initially co-housed, however, after the aggression incident at 2.5 months, all mice were housed individually to prevent further aggression and to keep the conditions between the mice comparable. Two study-related dropouts occurred in the second cohort (1 wild type and 1 transgenic), due to failure of the intubation procedure (see below). Housing consisted of individually ventilated cages in rooms with a 12-hour day/night rhythm. The cages were supplied with cage bedding, cage enrichment (a small roll to hide in and a block of wood), and unlimited chow food and water. The body weights of the mice were measured monthly.

Animal preparation – the isoflurane anesthesia protocol during the first 4 imaging sessions in cohort 1 was similar to the "low isoflurane protocol" as described in Munting *et al.*, 2019.[13] In this protocol, the isoflurane concentration is kept low both during induction (2.0 % for 5 minutes) and maintenance (1.25 %), to limit the vasodilatory effects of the anesthetic, which would impact the reactivity measurements. The mouse was freely breathing during the scan. During the 5th imaging session, anesthesia was maintained using 750 mg/kg urethane and 50 mg/kg alpha-chloralose (U&A), similar to the concentrations

used by Park *et al.*, 2014.[9] Anesthesia induction with U&A was performed using isoflurane (3.5 %), which was thereafter decreased to 1.75 %. Then, the trachea of the animal was surgically intubated for mechanical ventilation at 80 bpm, 25 % inspiration rate and 1.7 psi (MRI-1 ventilator, CWE Inc., USA). Additionally, an i.p. catheter was placed to administer U&A anesthesia during the MRI scans. Thirty-five minutes after U&A injection, the isoflurane was decreased over the course of 10 minutes to 0 %. During all sessions, transcutaneous partial pressure of carbon dioxide (tc-pCO$_2$) was monitored (TCM Radiometer, Denmark) with a neonate probe attached to the previously shaved skin on the right flank of the mouse.[29] Breathing rates were monitored using a pressure-sensitive pad placed below the animal (SA Instruments, NY, USA). Temperature was maintained at 36.5 ˚C using a feedback-controlled waterbed with rectal probe (Medres, Germany) and the head was stabilized with a bite bar and ear bars.

The second cohort was also anesthetized with U&A, however, in this cohort, the i.p. injection was given directly after the induction with 3.5 % isoflurane. Again, isoflurane was kept at 1.75 % for 35 minutes after injection, after which it was decreased to 0 % over the course of 10 minutes. While still at 1.75 % isoflurane, the trachea was surgically intubated for mechanical ventilation and additionally, a craniotomy of 3 mm in diameter was prepared over the right somatosensory cortex. The dura mater was left intact and kept moist with sterile PBS. Similar physiological monitoring was performed as in the first cohort. Fifteen minutes after the isoflurane reached 0 %, the LDF recording was started. After the LDF measurement, and before the animal was placed in the MRI scanner, the skin was placed back over the exposed skull and brain and sutured to limit susceptibility artefacts.

Image acquisition

MRI acquisition – a 7 T Pharmascan MRI scanner (Bruker, Germany) with a 23 mm transmit-receive volume coil was used. After proper placement of the mouse head in the bore was confirmed with a scout scan, 3 standard Bruker T2-weighted RARE scans (TE/TR = 35.0 ms/2500 ms; 78 × 78 x 700 µm³ resolution) were performed in all 3 directions for consistent planning across animals of the subsequent pseudo-continuous ASL (pCASL) scans. The coronal slice package with 21 slices was additionally used for quantification of the brain volume. The pCASL scan protocol was similar as in Munting *et al.*, 2019.[13] In short, the phase of the pCASL labeling was first optimized using pre-scans.[30] Thereafter, CBF and CVR were measured using a 21 minute pCASL scan with 180 dynamics, a labeling duration (τ) of 3000 ms, a post-labeling delay (PLD) of 300 ms and a 5 slice spin-echo echo planar imaging (SE-EPI) readout with 225 µm² resolution and 1.5 mm slice thickness (no slice gap). 7.5 % CO$_2$ was administered to the mouse from minute 7 till minute 14. For the last imaging session (12.3 months) of the mice in the first cohort, the number of dynamics of the pCASL scan was extended to 767 (scan duration of 90 minutes) to also

5

capture the effect of switching from isoflurane to U&A anesthesia on CBF. Specifically, the following steps were performed during the 1.5-hour ASL scan: at 5 minutes, U&A was injected, between minutes 40-50 isoflurane was decreased from 1.75 % till 0 % and between minute 72-79, 7.5 % CO_2 was administered. At the fourth scan session (12 months), two time-encoded pCASL (te-pCASL) sequences were additionally acquired per mouse for measuring the ATT. The second te-pCASL sequence was performed while administering 7.5 % CO_2 to the mouse, which allowed measuring the effect of arterial pCO_2 elevation on the ATT. The scan parameters of the te-pCASL sequence were the same as in Hirschler *et al.*, 2018,[11] except for the resolution, which was decreased from 225 to 337 μm^2 to increase the signal-to-noise ratio (SNR). A 3 slice SE-EPI readout was used, with the same slice orientation as slice 1, 3 and 5 of the standard pCASL scan (thus with a slice gap of 1.5 mm). During every imaging session, for CBF quantification purposes, the T_1 of the tissue (T_{1t}) and the tissue magnetization (M_{0t}) were estimated by collecting an additional inversion recovery scan with the same 5 slice SE-EPI readout as the pCASL scans. Furthermore, a pCASL flow-compensated FLASH was acquired at the level of the carotids, 3 mm downstream of the labeling plane, to measure the labeling efficiency (α). An additional T_2-weighted (T2W) RARE anatomical sequence was acquired with the same slice orientation as that of the pCASL scan for registration purposes.

LDF acquisition – A PeriFlux system with a PF 5010 LDPM unit and two Laser Doppler probes was used for LDF monitoring (Perimed Instruments, Sweden). Both probes were placed at the somatosensory cortex, one directly on the exposed skull above the left hemisphere, the other approximately 0.5 mm above the exposed brain tissue of the right hemisphere (hereafter referred to as the left and right probe, respectively). Extraction of the LDF signal profile was done through DASYLab software (version 13, National Instruments, Germany).

After the last MRI measurement, a subgroup of mice (6 Tg-SwDI and 6 WT) was i.v. injected with 200 μL of DyLight-594-coupled lectin (lycopersicum esculentum, VectorLabs, CA, USA) in the tail vein for staining of the endothelium. This was followed 3 minutes later by an i.p. overdose of pentobarbital after which the mouse was transcardially perfused with 20 mL of ice-cold PBS and 20 mL of ice-cold 4 % PFA. The brain was isolated and overnight fixed in 4 % PFA. The tissue was thereafter preserved at 4 ˚C in PBS with 0.02 % sodium azide until further processing. The other mice followed the exact same steps, but without the i.v. lectin injection.

Image processing

T2W processing – One full-brain volume of interest (VOI) was manually drawn on one of the 21-slice T2W RARE scans, after which the VOI was propagated to the T2W RARE scans of the other datasets (both to other mice and to other time points) using the EVolution algorithm.[31] To derive the brain volume, the number of voxels in the VOI was multiplied

by the voxel volume.

ASL image processing – The ASL image processing pipeline was the same as used in Munting *et al.*, 2019.[13] In short, the SE-EPI frames within one pCASL scan were aligned using the image processing toolbox of MATLAB (version 2018b, Mathworks, USA). Subsequently CBF, CVR and ATT were calculated using the MATLAB based "Multi-Image Analysis (MIA)" software developed at the Grenoble Institute of Neuroscience (Grenoble, France).[32] CBF was calculated for each pair of label/control images, expressed in mL/100 g/min, and derived using Buxton's general kinetic perfusion model,[33] with the following equation:

$$CBF = \frac{\lambda \cdot \Delta M \cdot \exp(PLD/T_{1b})}{2 \cdot \alpha \cdot T_{1t} \cdot M_{0t} \cdot (1 - \exp(-\tau/T_{1t}))}$$

where λ is the blood-brain partition coefficient, i.e. 0.9 mL/g,[34] ΔM is the signal difference of the label and control images from the standard pCASL scans and T_{1b} is the longitudinal relaxation time of blood, i.e. 2230 ms at 7 T.[35] Baseline CBF was defined as the average of the last 20 repetitions ($\approx$ 2.3 minutes) before the start of CO_2 administration. CVR was defined as the ratio calculated from the average of the last 20 repetitions during CO_2, over the average of the last 20 repetitions before CO_2 administration. To calculate ATT, the decoded signal from the te-pCASL scans was used, as described in Hirschler *et al.*, 2018.[11] Cortical, thalamic and full mid-brain brain (ROIs) were manually drawn on one of the T2W RARE scans, after which they were propagated to the T2W RARE scans of the other datasets (both to other mice and to other time points) using the EVolution algorithm.[31] This image registration method was also applied to position the ROIs in the corresponding SE-EPIs. This allowed to retrieve CBF, CVR and ATT values for different brain regions. CBF time profiles were all filtered using a sliding window of 3 time points (after CBF calculation), besides the profiles acquired in cohort 2 in the cortical ROI of the hemisphere where the skull was removed (supplementary Figure 5), which were filtered with a sliding window of 7 time points.

LDF processing - The LDF signal time profiles extracted with DasyLab were filtered with a sliding window of 3 time points and normalized to the average signal during the first 7 minutes of the measurement (baseline signal).

Immunohistochemistry (IHC)

The fixed brains were embedded in paraffin, and subsequently cut in sections of 5 μm. After deparaffinization with xylene and rehydration through graded ethanol series, the slides were cooked for 20 minutes in citrate buffer for antigen retrieval. Slides were then stained overnight at 4 °C with anti-amyloid-β antibody (1:1000; Abcam ab2539) followed by a one-hour room temperature incubation with biotinylated secondary antibody (1:300;

5

Dako E0431). Immunodetection was visualized using an Avidin-Biotin Complex kit (Vector Laboratories, UK), and sections were counterstained with haematoxylin before mounting. The slides were digitized with an automatic bright field microscope (Philips Ultra Fast Scanner, Philips, the Netherlands) and assessed by one examiner (LPM) for positivity for amyloid-β.

Statistical testing

To test the effect of genotype on CBF, CVR, ATT, and tc-pCO$_2$, Mann-Whitney U tests were performed. For the longitudinal cohort, Friedman tests were performed to test the effect of age on CBF and CVR, post-hoc followed by Wilcoxon signed-rank tests to determine which of the individual age groups differed from each other. Only consecutive age-groups were compared to each other to restrict the stringency of the Bonferroni correction for multiple comparisons. Wilcoxon signed-rank tests were used to test the effect of anesthesia on CBF and CVR and to test the effect of CO$_2$ on the ATT. No statistical testing was performed in cohort 2, given the small group size. All tests were performed in the SPSS statistics software package, version 26 (IBM, Armonk, NY, USA).

ACKNOWLEDGEMENTS

COMPETING INTEREST

The authors declare that there is no conflict of interest.

REFERENCES

1. Banerjee G, Carare R, Cordonnier C, et al. The increasing impact of cerebral amyloid angiopathy: Essential new insights for clinical practice. *Journal of Neurology, Neurosurgery and Psychiatry* 2017; 88: 982–994.

2. Dumas A, Dierksen GA, Gurol ME, et al. Functional magnetic resonance imaging detection of vascular reactivity in cerebral amyloid angiopathy. *Ann Neurol* 2012; 72: 76–81.

3. van Opstal AM, van Rooden S, van Harten T, et al. Cerebrovascular function in presymptomatic and symptomatic individuals with hereditary cerebral amyloid angiopathy: a case-control study. *Lancet Neurol* 2017; 16: 115–122.

4. Yamada M, Tsukagoshi H, Otomo E, et al. Cerebral amyloid angiopathy in the aged. *J Neurol* 1987; 234: 371–376.

5. Davis J, Xu F, Deane R, et al. Early-onset and Robust Cerebral Microvascular Accumulation of Amyloid β-Protein in Transgenic Mice Expressing Low Levels of a Vasculotropic Dutch/Iowa Mutant Form of Amyloid β-Protein Precursor. *J Biol Chem* 2004; 279: 20296–20306.

6. Thal DR, Ghebremedhin E, Rüb U, et al. Two types of sporadic cerebral amyloid angiopathy. *J Neuropathol Exp Neurol* 2002; 61: 282–93.

7. Miao J, Xu F, Davis J, et al. Cerebral Microvascular Amyloid β Protein Deposition Induces Vascular Degeneration and Neuroinflammation in Transgenic Mice Expressing Human Vasculotropic Mutant Amyloid β Precursor Protein. *Am J Pathol* 2005; 167: 505–515.

8. Chow N, Bell RD, Deane R, et al. Serum response factor and myocardin mediate arterial hypercontractility and cerebral blood flow dysregulation in Alzheimer's phenotype. *Proc Natl Acad Sci U S A* 2007; 104: 823–828.

9. Park L, Koizumi K, El Jamal S, et al. Age-dependent neurovascular dysfunction and damage in a mouse model of cerebral amyloid angiopathy. *Stroke* 2014; 45: 1815–1821.

10. Alsop DC, Detre JA, Golay X, et al. Recommended implementation of arterial spin-labeled perfusion MRI for clinical applications: A consensus of the ISMRM perfusion study group and the European consortium for ASL in dementia. *Magn Reson Med*. Epub ahead of print 8 April 2014. DOI: 10.1002/mrm.25197.

11. Hirschler L, Munting LP, Khmelinskii A, et al. Transit time mapping in the mouse brain using time-encoded pCASL. *NMR Biomed* 2018; 31: e3855.

12. Petrinovic MM, Hankov G, Schroeter A, et al. A novel anesthesia regime enables neurofunctional studies and imaging genetics across mouse strains. *Sci Rep* 2016; 6: 24523.

13. Munting LP, Derieppe MPP, Suidgeest E, et al. Influence of different isoflurane anesthesia protocols on murine cerebral hemodynamics measured with pseudo-continuous arterial spin labeling. *NMR Biomed*; 32. Epub ahead of print 1 August 2019. DOI: 10.1002/nbm.4105.

14. Xu F, Grande AM, Robinson JK, et al. Early-onset subicular microvascular amyloid and neuroinflammation correlate with behavioral deficits in vasculotropic mutant amyloid β-protein precursor transgenic mice. *Neuroscience* 2007; 146: 98–107.

15. Ayata C, Shin HK, Salomone S, et al. Pronounced hypoperfusion during spreading depression in mouse cortex. *J Cereb Blood Flow Metab* 2004; 24: 1172–1182.

16. Sharp PS, Ameen-Ali KE, Boorman L, et al. Neurovascular coupling preserved in a chronic mouse model of Alzheimer's disease: Methodology is critical. *J Cereb Blood Flow Metab* 2019; 271678X19890830.

17. Mueggler T, Sturchler-Pierrat C, Baumann D, et al. Compromised hemodynamic response in amyloid precursor protein transgenic mice. *J Neurosci* 2002; 22: 7218–7224.

5

18. Maier FC, Wehrl HF, Schmid AM, et al. Longitudinal PET-MRI reveals β-amyloid deposition and rCBF dynamics and connects vascular amyloidosis to quantitative loss of perfusion. *Nat Med* 2014; 20: 1485–1492.

19. Sturchler-Pierrat C, Abramowski D, Duke M, et al. Two amyloid precursor protein transgenic mouse models with Alzheimer disease-like pathology. *Proc Natl Acad Sci* 1997; 94: 13287–13292.

20. Østergaard L, Engedal TS, Moreton F, et al. Cerebral small vessel disease: Capillary pathways to stroke and cognitive decline. *Journal of Cerebral Blood Flow and Metabolism* 2016; 36: 302–325.

21. Chakraborty A, Kamermans A, Van Het Hof B, et al. Angiopoietin like-4 as a novel vascular mediator in capillary cerebral amyloid angiopathy. *Brain* 2018; 141: 3377–3388.

22. Janssen BJA, De Celle T, Debets JJM, et al. Effects of anesthetics on systemic hemodynamics in mice. *Am J Physiol - Hear Circ Physiol*; 287. Epub ahead of print October 2004. DOI: 10.1152/ajpheart.01192.2003.

23. Wang Z, Schuler B, Vogel O, et al. What is the optimal anesthetic protocol for measurements of cerebral autoregulation in spontaneously breathing mice? *Exp Brain Res* 2010; 207: 249–258.

24. Dalkara T, Irikura K, Huang Z, et al. Cerebrovascular responses under controlled and monitored physiological conditions in the anesthetized mouse. *J Cereb Blood Flow Metab* 1995; 15: 631–8.

25. Keyeux A, Ochrymowicz-Bemelmans D, Charlier AA. Induced response to hypercapnia in the two-compartment total cerebral blood volume: Influence on brain vascular reserve and flow efficiency. *J Cereb Blood Flow Metab* 1995; 15: 1121–1131.

26. He J, Devonshire IM, Mayhew JEW, et al. Simultaneous laser Doppler flowmetry and arterial spin labeling MRI for measurement of functional perfusion changes in the cortex. *Neuroimage* 2007; 34: 1391–1404.

27. Kilkenny C, Browne WJ, Cuthill IC, et al. Improving Bioscience Research Reporting: The ARRIVE Guidelines for Reporting Animal Research. *PLoS Biol* 2010; 8: e1000412.

28. Faul F, Erdfelder E, Lang AG, et al. G*Power 3: A flexible statistical power analysis program for the social, behavioral, and biomedical sciences. In: *Behavior Research Methods*. Psychonomic Society Inc., pp. 175–191.

29. Ramos-Cabrer P, Weber R, Wiedermann D, et al. Continuous noninvasive monitoring of transcutaneous blood gases for a stable and persistent BOLD contrast in fMRI studies in the rat. *NMR Biomed* 2005; 18: 440–6.

30. Hirschler L, Debacker CS, Voiron J, et al. Interpulse phase corrections for unbalanced pseudo-continuous arterial spin labeling at high magnetic field. *Magn Reson Med* 2018; 79: 1314–1324.

31. Denis de Senneville B, Zachiu C, Ries M, et al. EVolution: an edge-based variational method for non-rigid multi-modal image registration. *Phys Med Biol* 2016; 61: 7377–7396.

32. Brossard C, Montigon O, Boux F, et al. MP3: Medical Software for Processing Multi-Parametric Images Pipelines. *Front Neuroinform* 2020; 14: 16.

33. Buxton RB, Frank LR, Wong EC, et al. A general kinetic model for quantitative perfusion imaging with arterial spin labeling. *Magn Reson Med* 1998; 40: 383–96.

34. Herscovitch P, Raichle ME. What is the correct value for the brain--blood partition coefficient for water? *J Cereb Blood Flow Metab* 1985; 5: 65–69.

35. Dobre MC, Uğurbil K, Marjanska M. Determination of blood longitudinal relaxation time (T1) at high magnetic field strengths. *Magn Reson Imaging* 2007; 25: 733–735.
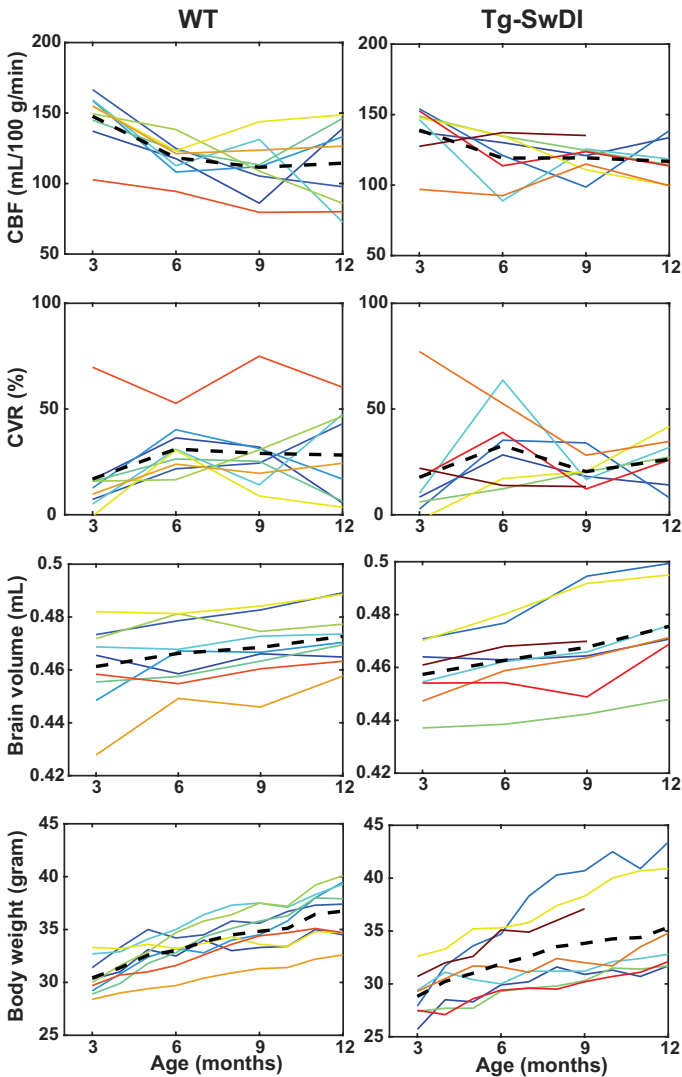
SUPPLEMENTARY INFORMATION

Figure 3-figure supplement 1: Animal-by-animal cerebral blood flow (CBF), cerebrovascular reactivity (CVR), brain volume and body weight progression with increasing age. On the top row, CBF trends are displayed, on the second row CVR trends, on the third row brain volume and on the last row body weight. The left column shows wild type (WT) mice, the right column transgenic Swedish Dutch Iowa (Tg-SwDI) mice. Every animal is represented with the same line color in the four graphs. The black dashed line represents the group mean.
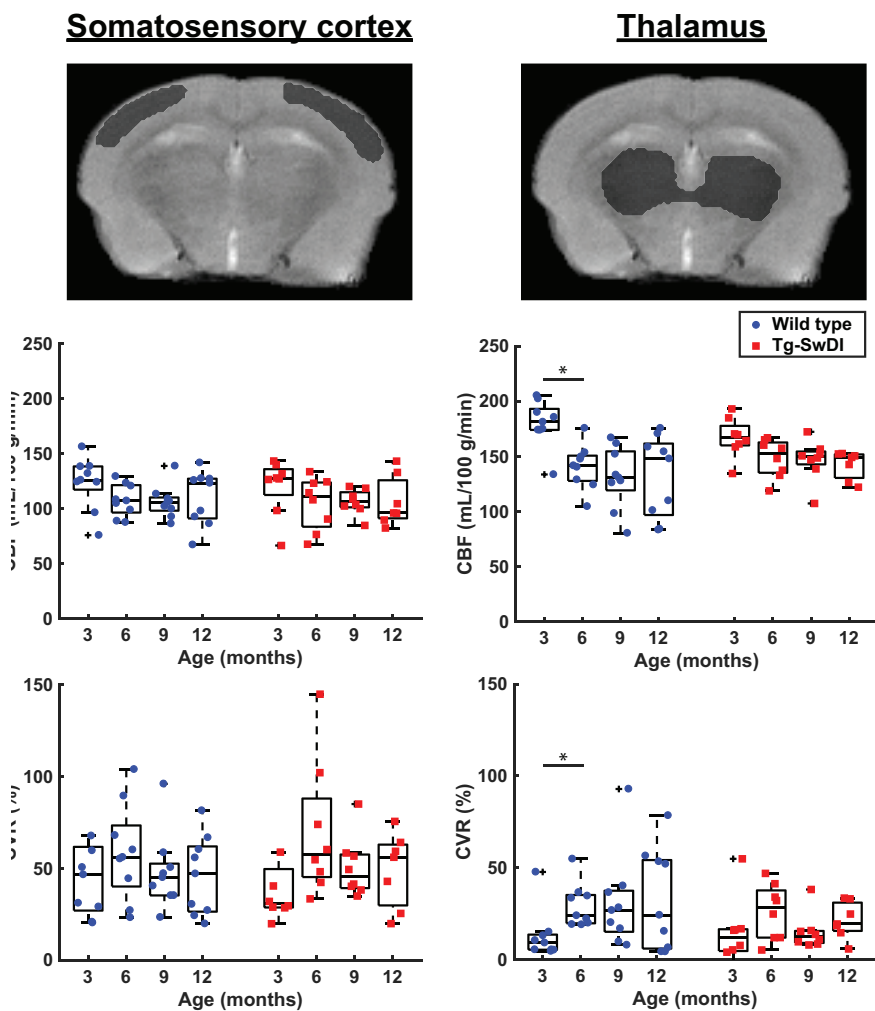
Figure 3-figure supplement 2: Cerebral blood flow (CBF) measurements in cortical (left) and thalamic (right) ROIs. On the top row, representative T2 weighted images are shown with overlaying areas (in gray) representing the brain regions that were analyzed. The middle row shows boxplot representations of baseline CBF (average of the last 2.3 minutes before the start of CO_2 administration) and bottom rows shows CVR (ratio of average of the last 2.3 minutes during CO_2 to baseline CBF). Circles and squares represent individual mice.
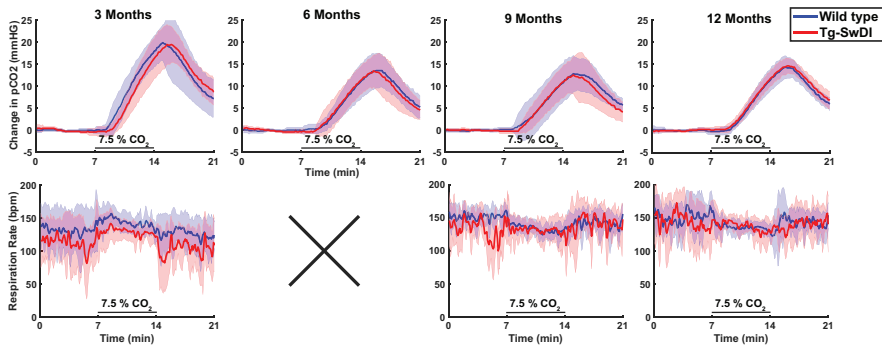
Figure 3-figure supplement 3: Change in transcutaneously measured pCO2 and respiration profiles during the pCASL measurements. On the first row, the pCO2 time profiles (mean ± standard deviation) acquired during the pCASL scans in cohort 1 for both wild types (WT) and transgenic Swedish Dutch Iowa (Tg-SwDI) are displayed. On the second row, the respiration profiles (mean ± standard deviation) are displayed. Note that the respiration profiles were not captured during the 2nd time point due to technical difficulties.
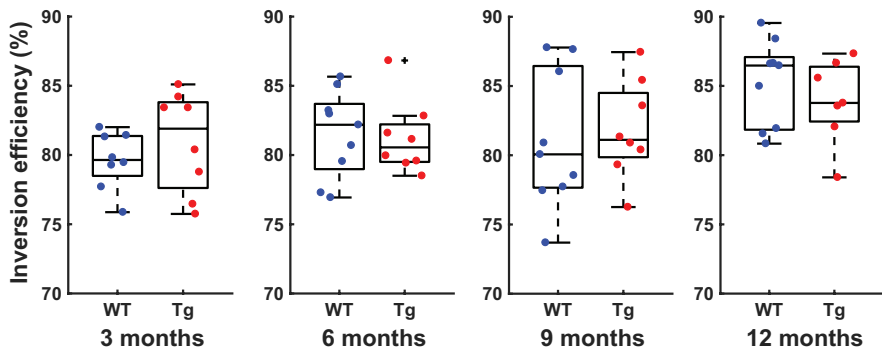
Figure 3-figure supplement 4: Inversion efficiency values measured at the different time points in cohort 1. In the graphs from left to right, increasing ages are shown. Within each graph, wild types (WT) and transgenic Swedish Dutch Iowa (Tg) mice are displayed.

5
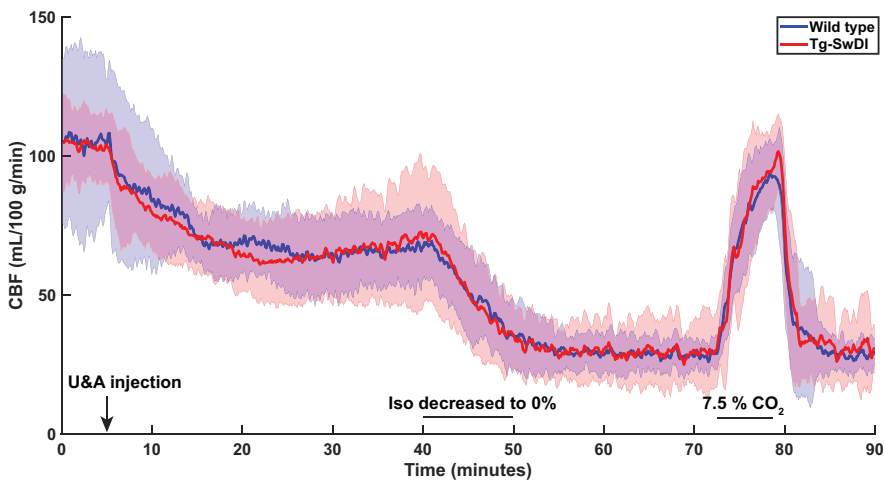
Figure 5-figure supplement 1: CBF change observed during switching from isoflurane anesthesia to urethane and α-chloralose (U&A). 90-minute CBF time profiles (mean ± standard deviation) are displayed acquired in cohort 1 for wild type and transgenic Swedish Dutch Iowa (Tg-SwDI) mice at an age of 12.3 months old. U&A was injected 5 minutes after the start of the arterial spin labeling-MRI scan. Isoflurane (iso) was decreased between minute 40 and 50. CO_2 was administered between minute 72 and 79.
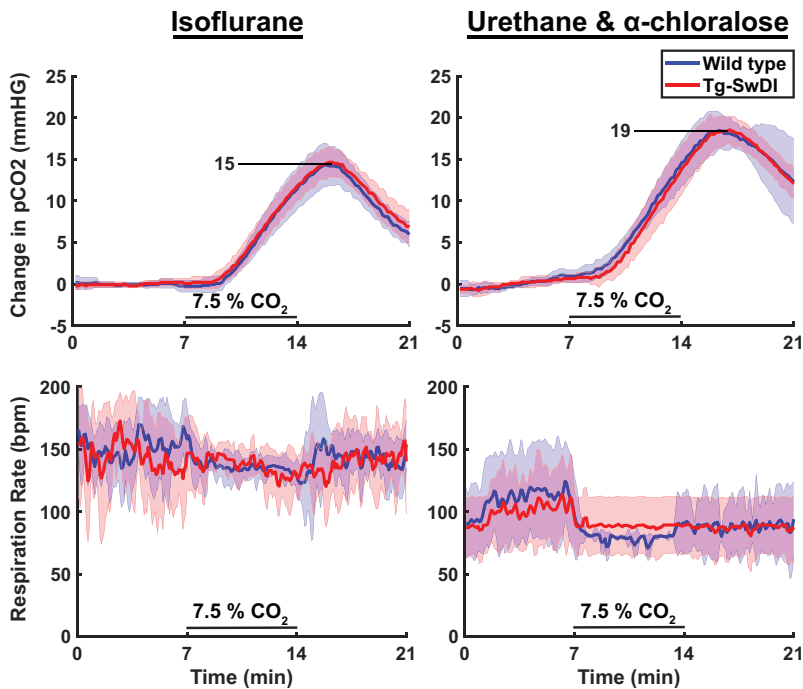
Figure 5-figure supplement 2: Change in transcutaneously measured pCO2 and respiration profiles under different anesthesia protocols. On the first row, the pCO$_2$ time profiles (mean ± standard deviation) acquired during the pseudo-continuous arterial spin labeling (pCASL) scans for both wild types (WT) and transgenic Swedish Dutch Iowa (Tg-SwDI) in the last two time-points of cohort 1 are displayed, with the acquisition under isoflurane on the left, the acquisition under urethane and α-chloralose on the right. On the second row, the respiration profiles (mean ± standard deviation) for the same time-points are displayed.
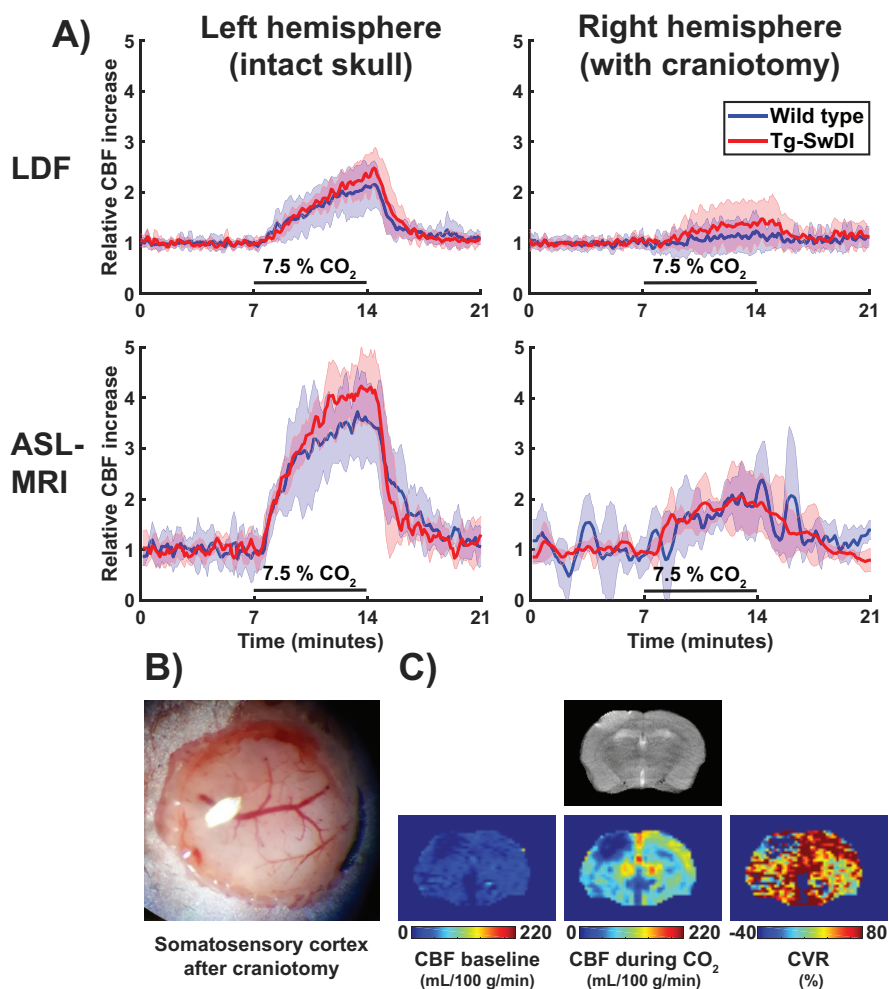
5

Figure 6-figure supplement 1: Cerebrovascular reactivity (CVR) measurements with Laser Doppler flowmetry (LDF) and arterial spin labeling (ASL MRI) with and without skull removal. A) displays CVR time profiles acquired either with LDF (top row) or ASL-MRI (bottom row). The left column shows the CVR time profiles from the intact, left hemisphere, the right column the profiles from the right hemisphere after craniotomy. B) shows a photograph of the somatosensory cortex of a representative mouse after craniotomy. C) On the top row, a T2 weighted image that was acquired with MRI after craniotomy. On the bottom row, cerebral blood flow (CBF) and CVR images that were acquired in the same scan session. Note that the left hemisphere is displayed on the right, according to radiological convention.

6

Summary

&

discussion

Summary

Alzheimer's disease (AD) and cerebral amyloid angiopathy (CAA) are both characterized by cerebral amyloidosis, i.e. deposition of amyloid-β in the brain, and impaired cerebrovascular function. The central goal in this thesis was to create a deeper understanding of the relation between amyloid-β deposition and cerebrovascular function. To that end, imaging techniques for the measurement of cerebrovascular function were optimized and applied in mouse models of amyloidosis.

Chapter 1 introduced some of the key concepts of structure and function of the brain vasculature during health and disease. Furthermore, different mouse models of amyloidosis were introduced, as well as techniques that exist to measure cerebrovascular function. One of the techniques, arterial spin labeling (ASL)-MRI, can measure brain perfusion quantitatively, dynamically and in a completely non-invasive manner, and was therefore the main technique used in this thesis for measuring cerebrovascular function. In chapter 2, a modified ASL sequence was described that not only measures brain perfusion, but also arterial transit time (ATT) of labeled blood into the mouse brain. ATT is an important parameter for the quantification of brain perfusion, but a change in ATT can in itself also indicate an underlying vascular pathology. With the modified ASL sequence, ATT could be time-efficiently measured in the mouse brain for the first time.

Since anesthesia is typically used with mouse MRI, which is known to influence hemodynamics, chapter 3 focused on the effect of different anesthesia protocols on the murine brain hemodynamics. A low induction, low maintenance isoflurane protocol was identified for repeated measurements of brain perfusion both under baseline conditions and during hypercapnia.

In chapters 4 and 5, the knowledge from the previous chapters was used to measure cerebrovascular function in mouse models of amyloidosis. The APP/PS1 mouse model was used in chapter 4. This particular mouse model develops parenchymal plaques and limited leptomeningeal amyloid-β accumulation, and thus reflects an AD-like distribution of amyloid-β pathology. These APP/PS1 mice surprisingly showed similar CBF and ATT values as the WT control group. In chapter 5, the transgenic Swedish Dutch Iowa (Tg-SwDI) mouse model was the topic of research, which develops extensive microvascular amyloid-β pathology, and thus reflects a more CAA-like distribution of amyloid-β pathology. However, also here, no cerebrovascular dysfunction was found, despite previous reports of impaired cerebrovascular function in Tg-SwDI mice by other groups.

The sequence of negative findings regarding cerebrovascular function and amyloid-β deposition in this thesis leaves us with additional questions. What is the validity of our models? And why do our results differ from those of other labs? In this chapter, these

questions will be discussed in more detail. But first, new findings from this thesis will be highlighted and put in context. Furthermore, some potentially interesting directions for future research will be indicated.

Discussion

New methodologies

The first part of this thesis mainly focused on the development of new methodologies for assessing cerebrovascular function. Firstly, a new time-encoded ASL sequence was developed in chapter 2, with which ATT values were measured for the first time in the mouse brain. ATT values were found in a range between 169 millisecond (ms) and 284 ms. This seems plausible given that similar values have been reported for the rat brain (Thomas *et al.*, 2006; Wells *et al.*, 2010). It was also shown that after carotid occlusion, CBF severely decreased and ATT mildly increased. This confirms that CBF and ATT measurements with ASL-MRI are sensitive to detect changes in vascular condition. Furthermore, the ATT values that were found are lower than the typically used post-label delay (PLD) values in pre-clinical ASL-MRI studies (Duhamel *et al.*, 2012). This indicates that previously carried out ASL studies in mice are probably not biased by incomplete arrival of the label, a potential source of error in perfusion MRI by ASL in humans (Alsop *et al.*, 2014). Also in contrast to humans, is that the CBF and ATT measurements could not be combined in a single "free-lunch approach" scan (Teeuwisse *et al.*, 2014). This is because a very high temporal resolution was required to measure the fast inflow times of the label in the mouse brain, which in turn required a high amount of averaging for sufficient ASL signal. The high amount of averaging would however have led to too long scan times when combined with the long labeling duration required for a CBF measurement. It is still unclear why the signal decay measured with the time-encoded ASL sequence was not consistent with the T_1 decay as measured with a standard inversion recovery scan, i.e. the T_1 decay of the ASL signal was much faster. Possibly, ASL signal still residing in the larger arteries plays a role, as described previously (Chappell *et al.*, 2010). In this case, after the label is initially detected in a certain voxel, it goes on to perfuse downstream tissue located in different voxels, thus leading to an artefactual signal decrease in the voxel where it is initially detected. It would be of interest for future developments to focus on removing this signal, for example by including vascular crushers, or by explicitly modeling the arterial signal (Chappell *et al.*, 2010). In the last part of chapter 2, ATT and CBF values were measured in the context of ageing, with a group comparison of baseline CBF and ATT values in wild type adult mice (6 months) and wild type old mice (24 months old). Both parameters were shown to remain stable in the ageing mouse brain.

Anesthesia is used in the vast majority of pre-clinical MRI studies, given the many practical and ethical restrictions associated with MRI in awake mice. Therefore, before

6

performing hemodynamic MRI studies with mouse models of amyloidosis, the effect of anesthesia on hemodynamics was first further explored in two strains of wild type mice in chapter 3. The study was limited to isoflurane and medetomidine protocols only, as these anesthetics allow for longitudinal imaging, in contrast to other anesthetics such as urethane, alpha-chloralose or etomidate. However, isoflurane is known to cause vasodilatation (Matta *et al.*, 1999), whereas medetomidine causes vasoconstriction (Sinclair, 2003). In this study, baseline CBF was measured, as well as the CVR to a hypercapnic challenge. It was shown that there was no CBF increase detectable to the challenge when the anesthetic isoflurane was used at a relatively standard concentration (3.5 % for induction, 1.5 % to 2.0 % for maintenance), referred to as the "medium isoflurane" protocol. This was in contrast to when medetomidine was used, with which strong CVR was observed. However, medetomidine did not induce sufficient depth of anesthesia in one of the two mouse strains tested, and furthermore led to relatively unstable CBF over time. Adaptations of the standard isoflurane protocol were therefore further explored. It was found that with either a lower induction and lower maintenance isoflurane protocol (2.0 % and 1.25 % respectively, referred to as "low isoflurane"), or with a protocol with mechanical ventilation under medium isoflurane concentrations, CBF increases upon hypercapnia were detected, albeit with smaller CVR than when medetomidine was used. Interestingly, an equal magnitude of the CVR response was observed between both adapted isoflurane protocols. However, when the same procedures were performed on a mouse strain with known ventilatory abnormalities – mice on a partial C3H background (Tankersley *et al.*, 1994) – no CBF response to hypercapnia could be detected with the low isoflurane protocol, but a similar CVR was found as compared to C57Bl/6J mice when the ventilation protocol was used. Together, this indicates that respiratory depression is likely an important factor in the attenuation of the CBF response to hypercapnia in mice anesthetized under medium isoflurane. However, intubation and mechanical ventilation requires highly skilled researchers, since it is a difficult procedure, while also dedicated hardware is needed. Furthermore, the procedure might cause damage to the mouse trachea. As such, the low isoflurane protocol is a much more attractive protocol, as it allows for similar CVR measurements, but without the aforementioned complications, as long as mice without ventilatory abnormalities are used. Thus, in short, this study identified a straight-forward and minimally invasive anesthesia protocol for repeated measurements of cerebrovascular function in mice, including a positive CVR upon hypercapnia. For future studies it would be interesting to implement a protocol for MRI in awake mice. Awake MRI has long been deemed impractical, however, in the field of intravital microscopy, awake imaging is becoming more and more standard, with sophisticated set-ups reducing the stress for the animals. Awake imaging not only removes the bias that anesthesia introduces in hemodynamic measurements, it also allows for studying stimulus-evoked neurovascular coupling.

Chapter 4 also had a more methodological character, as a pipeline was described to obtain quantitative values of the microvascular cerebral blood volume (mCBV) at microscopic resolution. Normally with microscopy, the high spatial resolution comes together with limited penetration depth, thereby limiting the assessed tissue volume to only a superficial slice. However, recent advances in tissue processing has enabled to optically clear tissue, which greatly increases the penetration depth of light. In this chapter, it was assessed whether tissue clearing could be used to image and quantify the volume of the microvasculature with a larger coverage. Specifically, the CUBIC clearing protocol (Susaki *et al.*, 2014) was applied to create transparent mouse brains in which the vasculature had previously been labeled *in vivo* with an intravenous injection of fluorescent lectin. After transparent tissue was created, a laser scanning microscope (LSM) was used, with a long working distance objective and an automated stage, to image a full hemisphere at high spatial resolution. Lastly, an extensive image post-processing pipeline was designed to calculate, for different brain regions, the microvascular blood volume (mCBV) as a percentage of the total tissue volume. With cleared tissue, normally, a light sheet microscope is used for imaging, as its sheet of excitation greatly speeds up acquisition times compared to the point excitation of a laser scanning microscope as used in this study. However, there is much less availability of light sheet microscopes at research institutes than that of laser scanning microscopes, and no light sheet microscope was available at our institute. But with the presented methodology, it was made possible to image large volumes of cleared tissue with laser scanning microscopy, albeit at the cost of an examination time of 2 to 3 days per hemisphere. From the brain regions analyzed, the mCBV values were highest in the thalamus and lowest in the white matter, which is in correspondence with other studies (Bohn *et al.*, 2016; Xiong *et al.*, 2017; Zhao & Pollack, 2009). An interesting area for future research would be to design a pipeline for registering MR images to microscopy images of transparent tissue, acquired in the same animal. This would allow to link areas in which dysfunctional measures found with MRI, such as reduced perfusion with ASL-MRI, can be linked to underlying pathology as visualized with microscopy.

Cerebrovascular function in amyloidosis models

The second part of this thesis consisted of the application of the newly developed methodologies to assess how amyloid-β accumulation affects cerebrovascular function in mouse models of amyloidosis. In chapter 4, cerebrovascular function was studied in the APP[swe]/PS1[dE9] mouse model (J L Jankowsky *et al.*, 2001) at old age. The model develops extensive parenchymal plaques and limited leptomeningeal CAA. CBF and ATT were measured (without a hypercapnic challenge), and compared to age-matched WT mice. Additionally, mCBV values obtained post-mortem with the implemented tissue clearing pipeline were compared to WT mice. However, no differences were found in

6

any of the three parameters. No previous studies have investigated ATT in AD mouse models, but regarding CBF and blood volume, there is some controversy in the literature about the APP^{swe}/PS1^{dE9} model. Reports vary from observations of CBF decrease (Cruz Hernández *et al.*, 2019), to no change (Delafontaine-Martel *et al.*, 2018; Hooijmans *et al.*, 2007), to even CBF increase (Guo *et al.*, 2019). The latter finding was, however, only at very young age. Regarding mCBV, there is also controversy, with one study reporting decreased mCBV (Zerbi *et al.*, 2013), and another reporting no change (Delafontaine-Martel *et al.*, 2018). Studies that found perfusion or blood volume changes, reported that the change was mainly restricted to the cortex and relatively small (<20 %). Thus, when taking these studies together with the results from chapter 4, at worst, APP^{swe}/PS1^{dE9} mice have mild cerebrovascular dysfunction. This is in contrast with other models, such as the APP23 model (Maier *et al.*, 2014), Tg2576 model (Maier *et al.*, 2014; Niwa *et al.*, 2002) or the Tg-SwDI model (Chow *et al.*, 2007; Park *et al.*, 2014), which have been reported to have much more severe cerebrovascular dysfunction. Common amongst these models is more severe amyloid-β accumulation in the brain vasculature. As such, the cerebrovascular dysfunction associated with AD and CAA seems thus to be linked to vascular amyloid-β accumulation in particular, as already suggested earlier (Maier *et al.*, 2014). Interestingly, another model with also a PS1 insertion - PS1^{L166} - also shows hardly any vascular amyloid-β accumulation and similarly no cerebrovascular dysfunction (Maier *et al.*, 2014). It therefore appears that a PS1 insertion in APP transgenic mice somehow leaves the cerebral vasculature unaffected. Likely, this is mediated through a shift in amyloid-β-40:amyloid-β-42 ratio towards amyloid-β-42, which is caused by the familial mutations in the PS1 insertions. This shifted ratio is known to cause early and extensive parenchymal plaque pathology (Joanna L. Jankowsky *et al.*, 2004). It could be hypothesized that the early accumulation of amyloid-β in parenchymal plaques also reduces the clearance of the peptide via the vasculature, thereby indirectly protecting the cerebral vasculature. In short, no cerebrovascular dysfunction was found in this thesis in the APP^{swe}/PS1^{dE9} model, which could be explained by its limited deposition of amyloid-β in the vasculature. Therefore, a model with profound amyloid-β deposition in the vasculature was assessed in the next chapter.

The Tg-SwDI model develops vascular amyloid-β accumulation starting at an age of 6 months. Specifically, amyloid-β accumulates around capillaries in several brain regions, including the thalamus, hippocampus and cortex. Thalamic and hippocampal capillaries are particularly heavily affected as compared to cortical capillaries, which are more mildly affected. However, the cortex is also additionally affected by the accumulation of diffuse parenchymal plaques (Davis *et al.*, 2004; Xu *et al.*, 2007). Impairments in cerebrovascular function in Tg-SwDI mice had already previously been shown by other groups (Chow *et al.*, 2007; Park *et al.*, 2014), even at the age of 3 months, which is before vascular amyloidosis can be observed. In these studies, CVR was measured with laser Doppler flowmetry

(LDF) under a terminal anesthesia protocol with α-chloralose and urethane, where the LDF probe was placed on exposed cortical brain tissue after craniotomy. In chapter 5 of this thesis, both baseline CBF and CVR were measured non-invasively in Tg-SwDI mice and WT controls, with ASL-MRI under the low isoflurane anesthesia protocol. The ASL measurements were performed in a longitudinal fashion, from an age when no amyloid-β pathology was present (3 months), up to an age when the brain microvasculature was heavily affected by amyloid-β pathology (12 months). To better compare our findings to previous reports, additional CVR measurements were performed under α-chloralose and urethane anesthesia, and with LDF. In contrast to previous studies, no cerebrovascular dysfunction was found in this study in Tg-SwDI mice. The mice even showed remarkably similar CBF and CVR values as their controls, irrespective of the anesthesia protocol or imaging modality used. It is unclear what difference in protocols could be the reason for the discrepancy. But one difference that has not been fully accounted for in this thesis, is that in the aforementioned studies, part of the skull was removed before carrying out the cerebrovascular function measurements, whereas here, the measurements were performed non-invasively. We hypothesize that skull removal may in fact be a needed second hit to evoke cerebrovascular dysfunction in Tg-SwDI mice, which has also been recently reported by another group for a different amyloidosis mouse model (Sharp *et al.*, 2019). An attempt was made to support this hypothesis with data. However, in our hands, when part of the skull was removed to expose brain tissue for a CVR measurement, the CVR was blunted in both genotypes. Furthermore, we noticed pronounced edema with MRI in the region of the craniotomy, despite the fact that the brain tissue appeared normal by eye. Possibly, a difference in the surgical protocol of others (Chow *et al.*, 2007; Park *et al.*, 2014) preferentially affected the cerebral vasculature in Tg-SwDI mice, and accounts for the difference in outcome. For future research, it would be interesting to examine how different craniotomy procedures affect cerebrovascular function, and how this might differently affect vulnerable vessels, i.e. with pre-existing vascular pathology.

Validity of the models
The second part of this thesis repeatedly reported the same finding: measurements of cerebrovascular function in the models of amyloidosis yielded comparable values as their wild type controls. This is, however, not consistent with observations in AD and CAA patients, for which there is a large and consistent body of evidence pointing towards dysfunction of the brain vasculature (den Abeelen *et al.*, 2014; Dumas *et al.*, 2012; Iturria-Medina *et al.*, 2016; van Opstal *et al.*, 2017). It is still unclear why the mouse models do not reflect this. Perhaps, it could be explained by differences in the underlying amyloid-β pathology in the patients versus the animal models. The extent to which the studied models reflect the amyloid-β pathology as observed in human patients will therefore be further discussed. Alternative possible reasons for the discrepancy will also be indicated.

6

Mice do not naturally develop amyloid-β pathology, because endogenous murine amyloid-β is not as aggregation-prone as human amyloid-β (Joanna L. Jankowsky *et al.*, 2007). The human *amyloid-β precursor protein (APP) gene* is therefore inserted as a transgene in the mouse genome to allow for build-up of amyloid-β peptides in the mouse brain. In some models, human *PS1* or *PS2*, which code for APP cleavage proteins, are inserted together with *APP*. The inserted transgenes are usually combined with a promotor that drives high expression by neurons, and contain one or more familial AD mutations to speed up the amyloid-β accumulation in the mouse (Joanna L. Jankowsky & Zheng, 2017).

APP/PS1 mice and familial AD
The first mouse model used in this thesis contained both *APP* with the Swedish mutation (APP^swe) and *PS1* without exon 9 (PS1^dE9)(J L Jankowsky *et al.*, 2001). Patients with both APP^swe and PS1^dE9 likely do not exist, which already questions whether the model represents a specific patient population. For simplicity however, the APP/PS1 model will here be compared to PS1^dE9 patients, as APP^swe is known to only increase amyloid-β production (Citron *et al.*, 1994), whereas PS1^dE9 is known to also shift the amyloid-β-40:amyloid-β-42 ratio (Joanna L. Jankowsky *et al.*, 2004). Pathologically, patients with a PS1^dE9 mutation show early and extensive amyloid-β parenchymal plaque formation. A specific type of amyloid-β plaque that sometimes occurs in tissue of these patients is the so-called cotton wool plaque. Additionally, the patients also develop CAA, both in parenchymal and leptomeningeal vessels (Brooks *et al.*, 2003). The patients develop early and severe cognitive decline, but hemorrhages are rare (Verkkoniemi *et al.*, 2000). Not many studies have focused on cerebrovascular function in PS1^dE9 patients. However, like for other AD patient populations, reduced CBF has been reported for pre-symptomatic patients with different PS1 mutations, albeit in a small and heterogenous cohort (McDade *et al.*, 2014). APP/PS1 mice also have early and extensive parenchymal plaque formation, and they also develop CAA to some extent, thus showing some clear pathological similarities to the patients. However, cotton wool plaques are not observed in these mice (Joanna L. Jankowsky *et al.*, 2004). Furthermore, CAA only occurs in the leptomeningeal vessels, not in the parenchymal vessels (Garcia-Alloza *et al.*, 2006). The mice thus do not fully recapitulate the pathology of the patient, which could perhaps play a role in the limited cerebrovascular dysfunction observed in our studies.

Tg-SwDI mice and familial CAA
The second mouse model used in this thesis was the Tg-SwDI mouse model. It has only 1 transgene (*APP*), but the transgene contains three mutations, i.e. the Swedish, Dutch and Iowa mutations. Such a triple mutation does not occur in patients. But given that the Dutch and Iowa mutations lead to similar structural changes in two neighboring amino acids in the amyloid-β peptide (an exchange of a negatively charged amino acid for a neutral amino acid), this combination has been deemed a mere amplification of either

mutation. As already mentioned, the Swedish mutation causes an absolute increase in production of the peptide itself. Interestingly, in contrast to many other models, the *APP* transgene is expressed at very low quantities in Tg-SwDI mice, lower than endogenous murine *APP*. Given that in many amyloidosis models, the phenotype might be biased by the unphysiologically high expression of APP, the low expression is a favorable characteristic of the Tg-SwDI mouse model. Despite low *APP* expression, the model develops early capillary amyloid-β accumulation, starting at 6 months, which is illustrative of the aggressive aggregation properties of the amyloid-β peptide with both a Dutch and an Iowa mutation (Davis *et al.*, 2004). It is unsure what patient population the Tg-SwDI mouse model can be best compared to, as neither Dutch nor Iowa CAA patients develop such extensive capillary CAA. Dutch CAA patients have relatively spared capillaries, and hardly any parenchymal plaques. Iowa CAA patients have both affected arterioles and capillaries, as well as some degree of parenchymal plaques (Kamp *et al.*, 2014). Tg-SwDI mice thus better resemble the Iowa CAA pathology. However, no functional data is available in the Iowa patients, given there are very few of these patients, and thus functional effects of the pathology in mouse and human cannot be compared. Yet another group of patients, also known as type 1 CAA or capCAA patients, does develop extensive capillary CAA, albeit sporadically, i.e. without any of the familial AD or CAA mutations (Thal *et al.*, 2002). Tg-SwDI mice thus also show some degree of pathological similarity to these patients. However, no studies have been performed which report cerebrovascular function specifically for capCAA patients, probably related to the fact that there are no criteria for *in vivo* diagnosis of capCAA. It is thus unclear whether the preserved cerebrovascular function with capCAA, as found here in the Tg-SwDI mice, is comparable to the effect that this pathology would have in humans. Possibly, the data here could even be an indication that also in humans, capCAA is not likely to severely affect baseline CBF, nor CBF responses to systemic challenges such as hypercapnia. However, it is important to mention that capillary dysfunction might still lead to inefficient oxygen uptake from the capillary network, even in the absence of CBF limiting pathology (Østergaard *et al.*, 2016). Interestingly, angiopoietin-4, a hypoxia inducible factor, was found to be highly expressed in brain tissue of capillary CAA patients (Chakraborty *et al.*, 2018), thus providing support for the notion that capillary CAA can induce hypoxic conditions.

Late onset AD
No good mouse model exists for an older dementia patient that comes to the memory clinic without any genetic history of AD or CAA. Even though AD pathology is the most common underlying pathology in patients with dementia, most patients have mixed pathologies, which can include amongst others parenchymal and vascular amyloid-β accumulation, microbleeds, microinfarcts and Lewy bodies ("2020 Alzheimer's disease facts and figures," 2020). Furthermore, histories of diabetes, smoking, alcohol abuse, etc., can cloud the picture even more. Current mouse models only reflect a minor part

6

of that complex picture. It is thus likely that results obtained in mouse models translate poorly to an elderly demented patient.

In conclusion on model validity, globally, amyloid-β pathology in the mouse models of amyloidosis used here are relatively comparable to that observed in familial AD and CAA patients: the transgenes with familial AD mutations cause parenchymal plaque formation in the mouse, like in a familial AD patient; the transgene with familial CAA mutations causes vascular amyloidosis in the mouse, like in a familial CAA patient. However, in more detail, pathology in the patients and the models shows differences, such as the type of parenchymal plaque and the localization of amyloid-β along the vascular tree. These differences could lead to the observed discrepancies regarding the effect of the pathology on cerebrovascular function between the patients and the models. However, additionally, species-specific differences in molecules that interact with both amyloid-β and the vasculature, such as APOE or fibrinogen, could also play a role. Furthermore, artefacts related to the unphysiologically high expression of APP or the double or triple mutations might also be involved. The lack of vascular dysfunction in the mouse models of amyloidosis used here, is not a unique discrepancy between the models and patients. For example, a wide variety of novel or repurposed treatments have been tested in mouse models and yielded positive results such as reduction of amyloid-β accumulation and improvement of cognition. However, all these treatments failed when tested in humans. Either they were not safe, or they failed to show any efficacy in improving the outcome markers (Sabbagh *et al.*, 2013). Other examples of discrepancies between the models and patients are the lack of macro-bleeds in CAA-like mouse models, or the lack of true tau tangle development in AD-like mouse models (Joanna L. Jankowsky & Zheng, 2017).

Alternative models
Given the limited translatability of the findings in the amyloidosis models used here, one may wonder if there are better models for amyloidosis as observed in AD and CAA. Other models do exist, such as other animal models, or *in vitro* models. Other animal models include other mouse models, rats, and even monkeys. One interesting alternative mouse model is the APP23 model, a model which overexpresses APP with only the Swedish mutation, thus not containing any mutation in the amyloid-β coding regions. The model shows late-onset, but prominent arteriolar CAA (Calhoun *et al.*, 1999). In a previous study (Maier *et al.*, 2014), two different mouse models of amyloidosis were studied at different ages with ASL-MRI for baseline perfusion measurements (with a FAIR sequence, which is different from the pCASL sequence used here). Additionally, PiB-PET measurements were performed for detection of amyloid-β deposition. The authors showed that only the APP23 model developed a perfusion decrease, which coincided with an increase in amyloid-β deposition as measured with PiB-PET. The wild type mice and a parenchymal amyloidosis model both showed preserved perfusion up to a high age. Thus, perhaps arteriolar CAA

is the main driver for cerebrovascular dysfunction, at least in mice. Unfortunately, the APP23 model could not be obtained in Leiden while the research in this thesis was carried out. It would thus be interesting for future research to further assess cerebrovascular function in the APP23 mouse model, including CVR and ATT, and compare whether these measures are earlier or later affected than baseline CBF. Rat models with AD and CAA-like pathology also exist, and they have in general been reported to better reflect human aspects of AD or CAA. For example, rat models with tau tangles already exist (Cohen *et al.*, 2013), as well as models with vessel ruptures (Zhu *et al.*, 2020). Furthermore, the range of cognitive tests that can be applied are much larger in rats than in mice, which would allow assessing the effect of the pathology on cognition, as well as the effect of novel treatments on cognitive performance. However, the genetic modification possibilities for rats are still lagging those of mice, and housing of rats is more expensive, but these disadvantages could be overcome. One could also consider higher order animals as models of AD or CAA, such as monkeys. However, this puts in much more weight on the ethical side, which may not be worth the gain in model improvement.

Recent developments in cell culture techniques are also promising. Induced pleuripotent stem (iPS) cells, derived from AD and CAA patient's skin cells, have already been differentiated into neurons, and grown in a 3D cell culture environment. The results are truly fascinating, and include 3D human cell cultures that produce amyloid-β plaques and tau tangles (Choi *et al.*, 2014). As an advantage over animal models, such models have a genetic background that is the same as in humans. Species-specific protein isoforms, such as aggregating amyloid-β in the human versus non-aggregating amyloid-β in the mouse, are not an issue in these models. Such models are therefore advantageous in certain conditions, for example when performing a target engagement screen for novel drugs, for which the outcome heavily relies on protein isoforms. In the near future, hopefully these models will start to replace some of the more standardized safety and target engagement screens of novel drugs for which animals are now still used. However, more fundamental research, such as research focusing on the relation between amyloid-β accumulation and cerebrovascular function, cannot be carried out in such *in vitro* models, as they lack perfusion and a functioning vasculature. Even if artificial perfusion would be included in the near future in an *in vitro* model, this will still be very different from a living brain, supplied with oxygenated blood by the heart and lungs, with systemic regulation, autoregulatory capabilities and neurovascular coupling. We should never stop to strive for replacing animal studies with *in vitro* studies, and hopefully the need for animal studies will reach zero one day. However, the painful truth is that proper *in vitro* models that reflect the complexity of organ systems are not available, neither at the moment, nor in the near future. A proper *in vitro* model will also not suddenly appear when a government decides to make a country free of animal testing in e.g. 2025.

6

In conclusion, mouse models of amyloidosis reflect human AD or CAA only up to a limited extent. Translation of findings from the mouse to the human should thus always be done with care and may be sometimes be invalid. Newer and better options are however becoming available. Likely, screens for target engagement of novel drug compounds in animal models will be replaced by *in vitro* models, and rat models will likely replace mice for research questions that require a more realistic model of AD or CAA. However, research questions that require sophisticated genetic modification tools, such as enabling optogenetic control of specific cell types, will probably continue to be performed in mice for some time, given the advanced tools available for genetic modification in mice.

Reproducibility in research
Another problem in this thesis was the discrepancy of our studies with the results of other pre-clinical studies. This is again a problem that is not unique to vascular dysfunction in mouse models of amyloidosis. Shockingly low numbers of reproducibility were reported in studies that were dedicated to reproducing findings from other labs. In the fields of oncology, drug target discovery and psychology, the reproducibility estimates were 11 % (Begley & Ellis, 2012), 20-25 % (Prinz *et al.*, 2011) and 39 % (Collaboration, 2015), respectively. Furthermore, in a Nature survey from 2016 amongst 1576 researchers, 52 % responded that there is a reproducibility crisis going on in research (Baker & Penny, 2016). However, with more than half of the surveyed researchers in 2016 indicating that there is a crisis going on, surprisingly little has been done since. A long list of causes has been put forward in the Nature publication, of which selective reporting and pressure to publish have been deemed the most important. Another long list of potential remedies was proposed, of which better understanding of statistics and better mentoring were rated as likely the most effective.

Personally, I do not think that the highest rated remedies are going to be very effective. A better understanding of statistics and better mentoring are not going to fundamentally change the way that data acquisition is performed. It seems to me that the real problem is that there is not enough incentive to actually perform reproducibility checks before starting new research. If one lab decides that their researchers must first replicate the previous findings which are key for their new hypothesis, before actually continuing to carry out the research needed to test their new hypothesis, then this will significantly slow down the research output of that lab. In the long run, this will mean that the lab will not be able to compete with other labs in terms of funding. It is therefore much better to start testing new hypotheses immediately, which independent of its outcome, and whether it actually builds on previous research or not, thereby already has the important value of newness attached to it. This will lead to the publication of new scientific papers, which will subsequently lead to new funding. As a result of this system, the outcome of the research lines from different labs have become disconnected, with a lack of understanding

of the underlying reasons for the outcome of the individual experiments from other labs. Improving the understanding of statistics of (young) researchers, requires teaching one or several courses, which is relatively easy to do, and may give a feeling that we are doing something to tackle this crisis. Sometimes, it may even lead to a researcher interpreting his or her data differently. However, if the process of data collection remains the same, I fear that this is not going to turn around the shockingly low numbers of reproducibility. One lab cannot change on its own, because then it will just succumb in the competition. Perhaps mandatory components on reproducibility could be included in grants, where researchers have to report the results of their replication studies before continuing with their new hypothesis. It may seem initially that this will slow down "scientific progress". However, on the long run, it may significantly reduce the $28 billion per year that is spent on irreproducible research in the USA alone (Freedman *et al.*, 2015). Only in a collaborative effort, in which reproducibility becomes engrained in the way we do science, will we be able to resolve the crisis. Small steps are already taken in that direction, with initiatives such as FAIR (findable, accessible, interoperable and reusable) principles to support reuse of data (Wilkinson *et al.*, 2016), and the introduction of meta-analyses in the pre-clinical research community (Sena *et al.*, 2014)

In summary, in this thesis, the methodology for pre-clinical assessment of cerebrovascular function was further refined. Additionally, several cerebrovascular function measurements were performed in mouse models of amyloidosis, but no differences were found when compared to their healthy controls. Despite the negative connotation of that finding, it is another small step towards better understanding the exact relationship between cerebrovascular dysfunction and amyloid-β deposition in AD and CAA patients.

6

REFERENCES

1. 2020 Alzheimer's disease facts and figures. (2020). *Alzheimer's and Dementia*, *16*(3), 391–460. https://doi.org/10.1002/alz.12068

2. Alsop, D. C., Detre, J. A., Golay, X., Günther, M., Hendrikse, J., Hernandez-Garcia, L., Lu, H., Macintosh, B. J., Parkes, L. M., Smits, M., van Osch, M. J. P., Wang, D. J. J., Wong, E. C., & Zaharchuk, G. (2014). Recommended implementation of arterial spin-labeled perfusion MRI for clinical applications: A consensus of the ISMRM perfusion study group and the European consortium for ASL in dementia. *Magnetic Resonance in Medicine : Official Journal of the Society of Magnetic Resonance in Medicine / Society of Magnetic Resonance in Medicine*. https://doi.org/10.1002/mrm.25197

3. Baker, M., & Penny, D. (2016). Is there a reproducibility crisis? In *Nature* (Vol. 533, Issue 7604, pp. 452–454). Nature Publishing Group. https://doi.org/10.1038/533452A

4. Begley, C. G., & Ellis, L. M. (2012). Drug development: Raise standards for preclinical cancer research. *Nature*, *483*(7391), 531–533. https://doi.org/10.1038/483531a

5. Bohn, K. A., Adkins, C. E., Mittapalli, R. K., Terrell-Hall, T. B., Mohammad, A. S., Shah, N., Dolan, E. L., Nounou, M. I., & Lockman, P. R. (2016). Semi-automated rapid quantification of brain vessel density utilizing fluorescent microscopy. *Journal of Neuroscience Methods*, *270*, 124–131. https://doi.org/10.1016/j.jneumeth.2016.06.012

6. Brooks, W. S., Kwok, J. B. J., Kril, J. J., Broe, G. A., Blumbergs, P. C., Tannenberg, A. E., Lamont, P. J., Hedges, P., & Schofield, P. R. (2003). Alzheimer's disease with spastic paraparesis and`cotton and`cotton wool' plaques: two pedigrees with PS-1 exon 9 deletions. *Brain*, *126*, 783–791. https://doi.org/10.1093/brain/awg084

7. Calhoun, M. E., Burgermeister, P., Phinney, A. L., Stalder, M., Tolnay, M., Wiederhold, K. H., Abramowski, D., Sturchler-Pierrat, C., Sommer, B., Staufenbiel, M., & Jucker, M. (1999). Neuronal overexpression of mutant amyloid precursor protein results in prominent deposition of cerebrovascular amyloid. *Proceedings of the National Academy of Sciences of the United States of America*, *96*(24), 14088–14093. https://doi.org/10.1073/pnas.96.24.14088

8. Chakraborty, A., Kamermans, A., Van Het Hof, B., Castricum, K., Aanhane, E., Van Horssen, J., Thijssen, V. L., Scheltens, P., Teunissen, C. E., Fontijn, R. D., Van Der Flier, W. M., & De Vries, H. E. (2018). Angiopoietin like-4 as a novel vascular mediator in capillary cerebral amyloid angiopathy. *Brain*, *141*(12), 3377–3388. https://doi.org/10.1093/brain/awy274

9. Chappell, M. A., MacIntosh, B. J., Donahue, M. J., Günther, M., Jezzard, P., & Woolrich, M. W. (2010). Separation of macrovascular signal in multi-inversion time arterial spin labelling MRI. *Magnetic Resonance in Medicine*, *63*(5), 1357–1365. https://doi.org/10.1002/mrm.22320

10. Choi, S. H., Kim, Y. H., Hebisch, M., Sliwinski, C., Lee, S., D'Avanzo, C., Chen, H., Hooli, B., Asselin, C., Muffat, J., Klee, J. B., Zhang, C., Wainger, B. J., Peitz, M., Kovacs, D. M., Woolf, C. J., Wagner, S. L., Tanzi, R. E., & Kim, D. Y. (2014). A three-dimensional human neural cell culture model of Alzheimer's disease. *Nature*, *515*(7526), 274–278. https://doi.org/10.1038/nature13800

11. Chow, N., Bell, R. D., Deane, R., Streb, J. W., Chen, J., Brooks, A., Van Nostrand, W., Miano, J. M., & Zlokovic, B. V. (2007). Serum response factor and myocardin mediate arterial hypercontractility and cerebral blood flow dysregulation in Alzheimer's phenotype. *Proceedings of the National Academy of Sciences of the United States of America*, *104*(3), 823–828. https://doi.org/10.1073/pnas.0608251104

12. Citron, M., Vigo-Pelfrey, C., Teplow, D. B., Miller, C., Schenk, D., Johnston, J., Winblad, B., Venizelos, N., Lannfelt, L., & Selkoe, D. J. (1994). Excessive production of amyloid-β-protein by peripheral

cells of symptomatic and presymptomatic patients carrying the Swedish familial Alzheimer disease mutation. *Proceedings of the National Academy of Sciences of the United States of America*, *91*(25), 11993–11997. https://doi.org/10.1073/pnas.91.25.11993

13. Cohen, R. M., Rezai-Zadeh, K., Weitz, T. M., Rentsendorj, A., Gate, D., Spivak, I., Bholat, Y., Vasilevko, V., Glabe, C. G., Breunig, J. J., Rakic, P., Davtyan, H., Agadjanyan, M. G., Kepe, V., Barrio, J. R., Bannykh, S., Szekely, C. A., Pechnick, R. N., & Town, T. (2013). A transgenic alzheimer rat with plaques, tau pathology, behavioral impairment, oligomeric Aβ, and frank neuronal loss. *Journal of Neuroscience*, *33*(15), 6245–6256. https://doi.org/10.1523/JNEUROSCI.3672-12.2013

14. Collaboration, O. S. (2015). Estimating the reproducibility of psychological science. *Science*, *349*(6251), aac4716–aac4716. https://doi.org/10.1126/science.aac4716

15. Cruz Hernández, J. C., Bracko, O., Kersbergen, C. J., Muse, V., Haft-Javaherian, M., Berg, M., Park, L., Vinarcsik, L. K., Ivasyk, I., Rivera, D. A., Kang, Y., Cortes-Canteli, M., Peyrounette, M., Doyeux, V., Smith, A., Zhou, J., Otte, G., Beverly, J. D., Davenport, E., … Schaffer, C. B. (2019). Neutrophil adhesion in brain capillaries reduces cortical blood flow and impairs memory function in Alzheimer's disease mouse models. *Nature Neuroscience*, *22*(3), 413–420. https://doi.org/10.1038/s41593-018-0329-4

16. Davis, J., Xu, F., Deane, R., Romanov, G., Previti, M. Lou, Zeigler, K., Zlokovic, B. V., & Van Nostrand, W. E. (2004). Early-onset and Robust Cerebral Microvascular Accumulation of Amyloid-β-Protein in Transgenic Mice Expressing Low Levels of a Vasculotropic Dutch/Iowa Mutant Form of Amyloid-β-Protein Precursor. *Journal of Biological Chemistry*, *279*(19), 20296–20306. https://doi.org/10.1074/jbc.M312946200

17. Delafontaine-Martel, P., Lefebvre, J., Tardif, P.-L., Lévy, B. I., Pouliot, P., & Lesage, F. (2018). Whole brain vascular imaging in a mouse model of Alzheimer s disease with two-photon microscopy. *Journal of Biomedical Optics*, *23*(07), 1. https://doi.org/10.1117/1.JBO.23.7.076501

18. den Abeelen, A. S. S. M., Lagro, J., van Beek, A. H. E. A., & Claassen, J. A. H. R. (2014). Impaired cerebral autoregulation and vasomotor reactivity in sporadic Alzheimer's disease. *Current Alzheimer Research*, *11*(1), 11–17. http://www.ncbi.nlm.nih.gov/pubmed/24251392

19. Duhamel, G., Callot, V., Tachrount, M., Alsop, D. C., & Cozzone, P. J. (2012). Pseudo-continuous arterial spin labeling at very high magnetic field (11.75 T) for high-resolution mouse brain perfusion imaging. *Magnetic Resonance in Medicine : Official Journal of the Society of Magnetic Resonance in Medicine / Society of Magnetic Resonance in Medicine*, *67*(5), 1225–1236. https://doi.org/10.1002/mrm.23096

20. Dumas, A., Dierksen, G. A., Gurol, M. E., Halpin, A., Martinez-Ramirez, S., Schwab, K., Rosand, J., Viswanathan, A., Salat, D. H., Polimeni, J. R., & Greenberg, S. M. (2012). Functional magnetic resonance imaging detection of vascular reactivity in cerebral amyloid angiopathy. *Annals of Neurology*, *72*(1), 76–81. https://doi.org/10.1002/ana.23566

21. Freedman, L. P., Cockburn, I. M., & Simcoe, T. S. (2015). The Economics of Reproducibility in Preclinical Research. *PLOS Biology*, *13*(6), e1002165. https://doi.org/10.1371/journal.pbio.1002165

22. Garcia-Alloza, M., Robbins, E. M., Zhang-Nunes, S. X., Purcell, S. M., Betensky, R. A., Raju, S., Prada, C., Greenberg, S. M., Bacskai, B. J., & Frosch, M. P. (2006). Characterization of amyloid deposition in the APPswe/PS1dE9 mouse model of Alzheimer disease. *Neurobiology of Disease*, *24*(3), 516–524. https://doi.org/10.1016/j.nbd.2006.08.017

23. Guo, Y., Li, X., Zhang, M., Chen, N., Wu, S., Lei, J., Wang, Z., Wang, R., Wang, J., & Liu, H. (2019). Age- and brain region-associated alterations of cerebral blood flow in early Alzheimer's disease assessed in AβPPSWE/PS1ΔE9 transgenic mice using arterial spin labeling. *Molecular Medicine Reports*. https://doi.org/10.3892/mmr.2019.9950

6

24. Hooijmans, C. R., Rutters, F., Dederen, P. J., Gambarota, G., Veltien, A., van Groen, T., Broersen, L. M., Lütjohann, D., Heerschap, A., Tanila, H., & Kiliaan, A. J. (2007). Changes in cerebral blood volume and amyloid pathology in aged Alzheimer APP/PS1 mice on a docosahexaenoic acid (DHA) diet or cholesterol enriched Typical Western Diet (TWD). *Neurobiology of Disease*, *28*(1), 16–29. https://doi.org/10.1016/j.nbd.2007.06.007

25. Iturria-Medina, Y., Sotero, R. C., Toussaint, P. J., Mateos-Pérez, J. M., Evans, A. C., Weiner, M. W., Aisen, P., Petersen, R., Jack, C. R., Jagust, W., Trojanowki, J. Q., Toga, A. W., Beckett, L., Green, R. C., Saykin, A. J., Morris, J., Shaw, L. M., Khachaturian, Z., Sorensen, G., … Furst, A. J. (2016). Early role of vascular dysregulation on late-onset Alzheimer's disease based on multifactorial data-driven analysis. *Nature Communications*, *7*, 11934. https://doi.org/10.1038/ncomms11934

26. Jankowsky, J L, Slunt, H. H., Ratovitski, T., Jenkins, N. A., Copeland, N. G., & Borchelt, D. R. (2001). Co-expression of multiple transgenes in mouse CNS: a comparison of strategies. *Biomolecular Engineering*, *17*(6), 157–165. http://www.ncbi.nlm.nih.gov/pubmed/11337275

27. Jankowsky, Joanna L., Fadale, D. J., Anderson, J., Xu, G. M., Gonzales, V., Jenkins, N. A., Copeland, N. G., Lee, M. K., Younkin, L. H., Wagner, S. L., Younkin, S. G., & Borchelt, D. R. (2004). Mutant presenilins specifically elevate the levels of the 42 residue β-amyloid peptide in vivo: evidence for augmentation of a 42-specific γ secretase. *Human Molecular Genetics*, *13*(2), 159–170. https://doi.org/10.1093/hmg/ddh019

28. Jankowsky, Joanna L., Younkin, L. H., Gonzales, V., Fadale, D. J., Slunt, H. H., Lester, H. A., Younkin, S. G., & Borchelt, D. R. (2007). Rodent Aβ modulates the solubility and distribution of amyloid deposits in transgenic mice. *Journal of Biological Chemistry*, *282*(31), 22707–22720. https://doi.org/10.1074/jbc.M611050200

29. Jankowsky, Joanna L., & Zheng, H. (2017). Practical considerations for choosing a mouse model of Alzheimer's disease. In *Molecular Neurodegeneration* (Vol. 12, Issue 1). BioMed Central Ltd. https://doi.org/10.1186/s13024-017-0231-7

30. Kamp, J. A., Moursel, L. G., Haan, J., Terwindt, G. M., Lesnik Oberstein, S. A. M. J., Van Duinen, S. G., & Van Roon-Mom, W. M. C. (2014). Amyloid-β in hereditary cerebral hemorrhage with amyloidosis-Dutch type. *Reviews in the Neurosciences*, *25*(5), 641–651. https://doi.org/10.1515/revneuro-2014-0008

31. Maier, F. C., Wehrl, H. F., Schmid, A. M., Mannheim, J. G., Wiehr, S., Lerdkrai, C., Calaminus, C., Stahlschmidt, A., Ye, L., Burnet, M., Stiller, D., Sabri, O., Reischl, G., Staufenbiel, M., Garaschuk, O., Jucker, M., & Pichler, B. J. (2014). Longitudinal PET-MRI reveals β-amyloid deposition and rCBF dynamics and connects vascular amyloidosis to quantitative loss of perfusion. *Nature Medicine*, *20*(12), 1485–1492. https://doi.org/10.1038/nm.3734

32. Matta, B. F., Heath, K. J., Tipping, K., & Summors, A. C. (1999). Direct cerebral vasodilatory effects of sevoflurane and isoflurane. *Anesthesiology*, *91*(3), 677–680. http://www.ncbi.nlm.nih.gov/pubmed/10485778

33. McDade, E., Kim, A., James, J., Sheu, L. K., Kuan, D. C. H., Minhas, D., Gianaros, P. J., Ikonomovic, S., Lopez, O., Snitz, B., Price, J., Becker, J., Mathis, C., & Klunk, W. (2014). Cerebral perfusion alterations and cerebral amyloid in autosomal dominant Alzheimer disease. *Neurology*, *83*(8), 710–717. https://doi.org/10.1212/WNL.0000000000000721

34. Niwa, K., Kazama, K., Younkin, S. G., Carlson, G. A., & Iadecola, C. (2002). Alterations in Cerebral Blood Flow and Glucose Utilization in Mice Overexpressing the Amyloid Precursor Protein. *Neurobiology of Disease*, *9*(1), 61–68. https://doi.org/10.1006/NBDI.2001.0460

35. Østergaard, L., Engedal, T. S., Moreton, F., Hansen, M. B., Wardlaw, J. M., Dalkara, T., Markus, H. S., & Muir, K. W. (2016). Cerebral small vessel disease: Capillary pathways to stroke and cognitive decline. In *Journal of Cerebral Blood Flow and Metabolism* (Vol. 36, Issue 2, pp. 302–325). Nature

Publishing Group. https://doi.org/10.1177/0271678X15606723

36. Park, L., Koizumi, K., El Jamal, S., Zhou, P., Previti, M. Lou, Van Nostrand, W. E., Carlson, G., & Iadecola, C. (2014). Age-dependent neurovascular dysfunction and damage in a mouse model of cerebral amyloid angiopathy. *Stroke*, *45*(6), 1815–1821. https://doi.org/10.1161/STROKEAHA.114.005179

37. Prinz, F., Schlange, T., & Asadullah, K. (2011). Believe it or not: How much can we rely on published data on potential drug targets? In *Nature Reviews Drug Discovery* (Vol. 10, Issue 9, pp. 712–713). Nature Publishing Group. https://doi.org/10.1038/nrd3439-c1

38. Sabbagh, J. J., Kinney, J. W., & Cummings, J. L. (2013). Animal systems in the development of treatments for alzheimer's disease: Challenges, methods, and implications. In *Neurobiology of Aging* (Vol. 34, Issue 1, pp. 169–183). Neurobiol Aging. https://doi.org/10.1016/j.neurobiolaging.2012.02.027

39. Sena, E. S., Currie, G. L., McCann, S. K., Macleod, M. R., & Howells, D. W. (2014). Systematic reviews and meta-analysis of preclinical studies: Why perform them and how to appraise them critically. In *Journal of Cerebral Blood Flow and Metabolism* (Vol. 34, Issue 5, pp. 737–742). Nature Publishing Group. https://doi.org/10.1038/jcbfm.2014.28

40. Sharp, P. S., Ameen-Ali, K. E., Boorman, L., Harris, S., Wharton, S., Howarth, C., Shabir, O., Redgrave, P., & Berwick, J. (2019). Neurovascular coupling preserved in a chronic mouse model of Alzheimer's disease: Methodology is critical. *Journal of Cerebral Blood Flow and Metabolism : Official Journal of the International Society of Cerebral Blood Flow and Metabolism*, 271678X19890830. https://doi.org/10.1177/0271678X19890830

41. Sinclair, M. D. (2003). A review of the physiological effects of α2-agonists related to the clinical use of medetomidine in small animal practice. In *Canadian Veterinary Journal* (Vol. 44, Issue 11, pp. 885–897). Canadian Veterinary Medical Association.

42. Susaki, E. A., Tainaka, K., Perrin, D., Kishino, F., Tawara, T., Watanabe, T. M., Yokoyama, C., Onoe, H., Eguchi, M., Yamaguchi, S., Abe, T., Kiyonari, H., Shimizu, Y., Miyawaki, A., Yokota, H., & Ueda, H. R. (2014). Whole-brain imaging with single-cell resolution using chemical cocktails and computational analysis. *Cell*, *157*(3), 726–739. https://doi.org/10.1016/j.cell.2014.03.042

43. Tankersley, C. G., Fitzgerald, R. S., & Kleeberger, S. R. (1994). Differential control of ventilation among inbred strains of mice. *The American Journal of Physiology*, *267*(5 Pt 2), R1371-7. https://doi.org/10.1152/ajpregu.1994.267.5.R1371

44. Teeuwisse, W. M., Schmid, S., Ghariq, E., Veer, I. M., & van Osch, M. J. P. (2014). Time-encoded pseudocontinuous arterial spin labeling: Basic properties and timing strategies for human applications. *Magnetic Resonance in Medicine*, *00*, 1–11. https://doi.org/10.1002/mrm.25083

45. Thal, D. R., Ghebremedhin, E., Rüb, U., Yamaguchi, H., Del Tredici, K., & Braak, H. (2002). Two types of sporadic cerebral amyloid angiopathy. *Journal of Neuropathology and Experimental Neurology*, *61*(3), 282–293. http://www.ncbi.nlm.nih.gov/pubmed/11895043

46. Thomas, D. L. L., Lythgoe, M. F. F., van der Weerd, L., Ordidge, R. J. J., & Gadian, D. G. G. (2006). Regional variation of cerebral blood flow and arterial transit time in the normal and hypoperfused rat brain measured using continuous arterial spin labeling MRI. *Journal of Cerebral Blood Flow and Metabolism : Official Journal of the International Society of Cerebral Blood Flow and Metabolism*, *26*(2), 274–282. https://doi.org/10.1038/sj.jcbfm.9600185

47. van Opstal, A. M., van Rooden, S., van Harten, T., Ghariq, E., Labadie, G., Fotiadis, P., Gurol, M. E., Terwindt, G. M., Wermer, M. J. H., van Buchem, M. A., Greenberg, S. M., & van der Grond, J. (2017). Cerebrovascular function in presymptomatic and symptomatic individuals with hereditary cerebral amyloid angiopathy: a case-control study. *The Lancet Neurology*, *16*(2), 115–122. https://doi.org/10.1016/S1474-4422(16)30346-5

48. Verkkoniemi, A., Somer, M., Rinne, J. O., Myllykangas, L., Crook, R., Hardy, J., Viitanen, M., Kalimo, H.,

6

& Haltia, M. (2000). Variant Alzheimer's disease with spastic paraparesis: Clinical characterization. *Neurology*, *54*(5), 1103–1109. https://doi.org/10.1212/WNL.54.5.1103

49. Wells, J. A., Lythgoe, M. F., Gadian, D. G., Ordidge, R. J., & Thomas, D. L. (2010). In vivo Hadamard encoded continuous arterial spin labeling (H-CASL). *Magnetic Resonance in Medicine*, *63*(4), 1111–1118. https://doi.org/10.1002/mrm.22266

50. Wilkinson, M. D., Dumontier, M., Aalbersberg, Ij. J., Appleton, G., Axton, M., Baak, A., Blomberg, N., Boiten, J. W., da Silva Santos, L. B., Bourne, P. E., Bouwman, J., Brookes, A. J., Clark, T., Crosas, M., Dillo, I., Dumon, O., Edmunds, S., Evelo, C. T., Finkers, R., … Mons, B. (2016). Comment: The FAIR Guiding Principles for scientific data management and stewardship. *Scientific Data*, *3*(1), 1–9. https://doi.org/10.1038/sdata.2016.18

51. Xiong, B., Li, A., Lou, Y., Chen, S., Long, B., Peng, J., Yang, Z., Xu, T., Yang, X., Li, X., Jiang, T., Luo, Q., & Gong, H. (2017). Precise Cerebral Vascular Atlas in Stereotaxic Coordinates of Whole Mouse Brain. *Frontiers in Neuroanatomy*, *11*, 128. https://doi.org/10.3389/fnana.2017.00128

52. Xu, F., Grande, A. M., Robinson, J. K., Previti, M. L., Vasek, M., Davis, J., & Van Nostrand, W. E. (2007). Early-onset subicular microvascular amyloid and neuroinflammation correlate with behavioral deficits in vasculotropic mutant amyloid-β-protein precursor transgenic mice. *Neuroscience*, *146*(1), 98–107. https://doi.org/10.1016/j.neuroscience.2007.01.043

53. Zerbi, V., Jansen, D., Dederen, P. J., Veltien, A., Hamans, B., Liu, Y., Heerschap, A., & Kiliaan, A. J. (2013). Microvascular cerebral blood volume changes in aging APPswe/PS1dE9 AD mouse model: a voxel-wise approach. *Brain Structure and Function*, *218*(5), 1085–1098. https://doi.org/10.1007/s00429-012-0448-8

54. Zhao, R., & Pollack, G. M. (2009). Regional differences in capillary density, perfusion rate, and P-glycoprotein activity: A quantitative analysis of regional drug exposure in the brain. *Biochemical Pharmacology*, *78*(8), 1052–1059. https://doi.org/10.1016/j.bcp.2009.06.001

55. Zhu, X., Hatfield, J., Sullivan, J. K., Xu, F., & Van Nostrand, W. E. (2020). Robust neuroinflammation and perivascular pathology in rTg-DI rats, a novel model of microvascular cerebral amyloid angiopathy. *Journal of Neuroinflammation*, *17*(1), 78. https://doi.org/10.1186/s12974-020-01755-y

Nederlandse Samenvatting

De ziekte van Alzheimer en de ziekte cerebrale amyloïde angiopathy (CAA) worden beiden gekenmerkt door opstapeling van het amyloïd-β peptide in het brein, ook wel amyloïdose genaamd. Ook worden beide ziektes gekenmerkt door een verminderd functioneren van de hersenvaten. Het doel van het onderzoek in dit proefschrift was om de kennis over de relatie tussen amyloïdose en het functioneren van de hersenvaten uit te breiden. Om dit doel te bereiken werden technieken uit de medische beeldvorming, ook wel kortweg aangeduid met "imaging", verder geoptimaliseerd voor het meten van het functioneren van de hersenvaten, en vervolgens toegepast in muismodellen met en zonder amyloïdose.

In hoofdstuk 1 werden een aantal belangrijke begrippen geïntroduceerd over de samenstelling en het functioneren van gezonde en aangedane hersenvaten. Daarnaast werden verschillende soorten muismodellen met amyloïdose geïntroduceerd. Ook werden verschillende imaging technieken besproken die het functioneren van de hersenvaten kunnen meten, met extra nadruk op de techniek "Arterial Spin Labeling" (ASL), de meest gebruikte imaging techniek in dit proefschrift. ASL is een MRI-techniek die de hersendoorbloeding in absolute waardes kan meten zonder dat daarbij invasieve handelingen zoals injecties van contrastvloeistof vereist zijn. Het bloed in de halsslagaders wordt daartoe magnetisch gelabeld, waarna het als endogeen contrastmiddel gebruikt wordt om de hersendoorbloeding te meten. Een aanpassing op de al bestaande ASL-techniek werd beschreven in hoofdstuk 2, waarmee niet alleen de hoeveelheid bloed, maar ook de aankomsttijd van het bloed in verschillende breinregio's van het muizenbrein gemeten kan worden. Deze bloedaankomsttijd is een belangrijke parameter bij de berekening van de hersendoorbloeding, maar kan op zichzelf ook een belangrijke graadmeter zijn om vasculaire pathologie te detecteren. Met de aangepaste ASL-techniek kon de bloedaankomsttijd voor het eerst in het muizenbrein gemeten worden op een tijdsefficiënte manier.

Anesthesie is praktisch onvermijdelijk bij het uitvoeren van MRI in muizen. In hoofdstuk 3 werd daarom het effect beschreven van verschillende soorten anesthesie op de dynamiek van de bloedtoevoer naar het muizenbrein. Een specifiek anesthesie protocol waarbij gebruik gemaakt wordt van lage isofluraan concentraties werd beschreven, waarmee herhaalde metingen van hersendoorbloeding gedaan kunnen worden, zowel onder normale conditie als onder hypercapnie.

In hoofdstukken 4 en 5 werden de opgedane kennis en de ontwikkelde imaging technieken van de voorgaande hoofdstukken gebruikt om het functioneren van de hersenvaten in muismodellen met amyloïdose te meten. Hoofdstuk 4 richtte zich op het APP/PS1 model, waarin amyloïd-β zich voornamelijk opstapelt in het hersenparenchym (tussen de hersencellen), net zoals bij patiënten met de ziekte van Alzheimer. Opvallend was dat het functioneren van de hersenvaten in deze muizen niet verschilde ten opzichte

van muizen zonder amyloïd-β opstapeling. In hoofdstuk 5 werd het Tg-SwDI muismodel gebruikt. Dit model vertoont hevige microvasculaire amyloïd-β opstapeling, zoals ook voorkomt bij sommige patiënten met CAA. Echter, wederom werd geen verschil gevonden tussen het functioneren van de hersenvaten van deze muizen ten opzichte van muizen zonder amyloïd-β opstapeling. De bevindingen van dit proefschrift werden in hoofdstuk 6 verder bediscussieerd.

Verder onderzoek is nodig om uit te vinden of de negatieve resultaten in dit proefschrift verklaard kunnen worden door een beperkte validiteit van de muismodellen, of dat parenchymale en microvasculaire amyloïdoise geen belangrijke rol spelen bij het verminderd functioneren van de hersenvaten in patiënten met AD en CAA. Ondanks dat negatieve bevindingen niet heel spannend klinken, dragen ze wel bij aan het beter begrijpen van de precieze verhouding tussen amyloïdose en het functioneren van de hersenvaten. Uiteindelijk zal dat belangrijke informatie kunnen zijn om een broodnodige therapie te ontwikkelen voor patiënten met de ziekte van Alzheimer en CAA.

List of publications

1. Hirschler L*, **Munting LP***, Khmelinskii A, Teeuwisse WM, Suidgeest E, Warnking JM, van der Weerd L, Barbier EL, van Osch MJP. *Transit time mapping in the mouse brain using timeencoded pCASL*. NMR Biomed. 2018 Feb;31(2).

2. **Munting LP***, Derieppe MPP*, Suidgeest E, Denis de Senneville B, Wells JA, van der Weerd L. *Influence of different isoflurane anesthesia protocols on murine cerebral hemodynamics measured with pseudocontinuous arterial spin labeling*. NMR Biomed. 2019 Aug;32(8):e4105.

3. **Munting LP**, Derieppe M, Suidgeest E, Hirschler L, van Osch MJ, Denis de Senneville B, van der Weerd L. *Cerebral blood flow and cerebrovascular reactivity are preserved in a mouse model of cerebral microvascular amyloidosis*. Elife. 2021 Feb 12;10:e61279.

4. Gravesteijn G, **Munting LP**, Overzier M, Mulder AA, Hegeman I, Derieppe M, Koster AJ, van Duinen SG, Meijer OC, Aartsma-Rus A, van der Weerd L, Jost CR, van den Maagdenberg AMJM, Rutten JW, Lesnik Oberstein SAJ. *Progression and Classification of Granular Osmiophilic Material (GOM) Deposits in Functionally Characterized Human NOTCH3 Transgenic Mice*. Transl Stroke Res. 2020 Jun;11(3):517-527.

5. Grand Moursel L, **Munting LP**, van der Graaf LM, van Duinen SG, Goumans MTH, Ueberham U, Natté R, van Buchem MA, van Roon-Mom WMC, van der Weerd L. *TGFβ pathway deregulation and abnormal phospho-SMAD2/3 staining in hereditary cerebral hemorrhage with amyloidosis-Dutch type*. Brain Pathol. 2018 Jul;28(4):495-506.

6. van Mierlo HC, van Coevorden-Hameete MH, **Munting LP**, de Graaff E, de Witte L; GROUP investigators. *No evidence for the presence of neuronal surface autoantibodies in plasma of patients with schizophrenia*. Eur Neuropsychopharmacol. 2015 Dec;25(12):2326-32.

Curriculum vitae

Leon Munting was born on July 3rd, 1989, in Voorburg, in the Netherlands, and grew up in Zoetermeer. After high school, he moved to Utrecht to study biology at Utrecht University. Next to the wide variety of classes taught at the faculty of biology, Leon supplemented his education with courses taught at the faculty of psychology and the medical faculty of Utrecht University. He also spent 5 months as an exchange student at the Hong Kong University of Science and Technology. To keep up the international spirit after the exchange, Leon organized social and cultural activities together with fellow students in the Erasmus Student Network (ESN), for international students that came to Utrecht for an exchange program. After his bachelor, Leon pursued the master *Biology of Disease,* also at Utrecht University. He developed a keen interest in dementia during his summer jobs in an elderly home and then decided to dedicate himself to learn more about the underlying biology in his subsequent academic training. During a master internship at the Leiden University Medical Center under supervision of dr. Laure Grand Moursel, he then studied the role of the inflammatory cytokine TGF-β in a familial form of cerebral amyloid angiopathy (CAA), a brain disease that leads to hemorrhage and dementia. This opened up the opportunity to pursue a PhD in the lab of dr. Louise van der Weerd, during which Leon developed an expertise in *in vivo* imaging of vascular function in the mouse brain. Currently, Leon is continuing his research at the Massachusetts General Hospital in Boston, as a post-doctoral fellow in the lab of dr. Susanne van Veluw, to study how waste products such as amyloid-β are cleared from the brain.

Dankwoord

kept such close contact from afar ever since. 21e bestuurtje, er is geen beter team, en jullie maakten mijn studententijd geniaal. Bedankt lieve familie, dat jullie altijd voor me klaar staan, en papa en mama, bedankt voor jullie onvoorwaardelijke liefde en oneindige ondersteuning.

Ma chère Lydiane, working with you was my favorite part of my PhD. Turns out being with you is even better. Merci pour tout!